Christoph Amtmann, BSc

Enhancements of a Coherent Population Trapping - Resonance Setup by Measurement Automation, Laser Collimation Control and Design of a Distributed Feedback - Laser Housing

MASTER'S THESIS

to achieve the university degree of

Master of Science

Master's degree programme: Technical Physics

submitted to

Graz University of Technology

Supervisor

Ao. Univ.-Prof.i.R. Dipl.-Ing. Dr. techn. tit. Univ.-Prof. Laurentius Windholz

Institute of Experimental Physics

Co-Supervisor

Dipl. Ing. Dr. techn. Roland Lammegger

Graz, December 2015

Abstract

This thesis deals with improvements of a Coherent Population Trapping (CPT)-resonance setup by a PC controlled measurement automation with included data recording. Additionally, a Laser Collimation Control-system and a Distributed Feedback (DFB)-laser housing are designed.

The thesis was written in the course of the CDSM-project at Graz University of Technology. The CDSM-project deals with the development and the design of the Coupled Dark State Magnetometer (CDSM). The (quantum mechanical) CPT-effect is used for the precise detection of magnetic fields.

The theory of the CPT-effect is explained in general and in combination with the Rubidium isotope ^{87}Rb.

A spectroscopic setup, using double-frequency modulated laser light, is applied for the investigation of the CPT-effect. The experiments are performed with the ^{87}Rb-isotope, which is confined as vapour within (spectroscopic) glass cells. Neon as buffer gas with a certain pressure is added. The used spectroscopic light source is a so called Vertical Cavity Surface Emitting Laser (VCSEL). Its emitted light is frequency modulated in the GHz-domain. This GHz frequency is produced by a microwave generator. For the detection of the CPT-resonance the microwave generator is tuned while the data of a lock-in amplifier are read out simultaneously. A LabView software, which was created in the course of this thesis, remotely controls the microwave generator and the lock-in amplifier. This allows the automation of the CPT-resonance spectroscopy setup and the additional creation and the management of measurement data files. The software's capability was shown at the characterisation of the 0-0-CPT-resonances as a function of the Ne-buffer gas pressure. This investigation showed that a Ne-buffer gas pressure in the range of 80 to 100 Torr results in the most suitable CPT-resonance parameters for the CDSM's sensor.

The collimation of the laser beam is necessary to ensure the smallest power broadening of the CPT-resonance linewidth . Therefore, a Laser Collimation Control (LCC)-system was designed.

An alternative approach for the design of the CPT-resonance spectroscopy setup is of interest. Therefore, this setup was adopted for a DFB-laser diode and a DFB-laser diode housing designed. This housing allows a precise diode temperature control of a few mK and a laser light frequency modulation capability in the GHz frequency regime.

Zusammanfassung

Diese Arbeit behandelt die Erweiterungen eines Coherent Population Trapping (CPT)-Resonanz-spektroskopischen Aufbaues durch eine PC-gesteuerte Automatisierung der Messroutinen mit inkludierter Messwertaufnahme. Zusätzlich wird ein "Laser Kollimations Kontroll-System" und ein Gehäuse für eine DFB-Laser Diode entwickelt.

Die vorliegende Arbeit wurden im Rahmen des CDSM-Projektes an der TU Graz verfasst. Das CDSM-Projekt beschäftigt sich mit der Entwicklung und der Konstruktion des namensgebenden Coupled Dark State Magnetometer (CDSM). Hier wird der (quantenmechanische) CPT-Effekt zur präzisen Bestimmung des Magnetfeldes genutzt.

In dieser Arbeit werden die theoretischen Grundlagen des CPT-Effektes im Allgemeinem und im Speziellen für das Rubidium-Isotop ^{87}Rb dargelegt. Zur experimentellen Untersuchung des CPT-Effektes wird ein spektroskopischer Aufbau verwendet, der mittels doppelt frequenzmoduliertem Laserlicht diese CPT-Resonanzen untersucht. Die Messungen werden an dem ^{87}Rb-Isotop durchgeführt, welches in der Gasphase (^{87}Rb-Dampf) vorliegt. Hierzu werden (spektroskopische) Glas-Zellen verwendet, in denen sich zusätzlich Neon, bei gezielt gewähltem Druck, als Puffergas befindet. Als spektroskopische Lichtquelle dient ein so genannter VCSEL, dessen emittiertes Licht im GHz-Bereich Frequenz moduliert ist. Zur Erzeugung des GHz-Signales wird ein Mikrowellen Generator verwendet. Zur Detektion des CPT-Effektes wird die GHz Frequenz des Mikrowellen Generators durchgestimmt. Gleichzeitig werden die Messdaten des Lock-In Verstärkers ausgelesen. Ein LabView-Programm, welches im Rahmen dieser Arbeit entwickelt wurde, steuert den Mikrowellen Generator und den Lock-In Verstärker. Dieses Programm ermöglicht die Automatisierung des CPT-Resonanz-spektroskopischen Aufbaues bei simultaner Erstellung und Verwaltung von Messdateien. Die Einsatzmöglichkeit des Programmes wurde anhand der spektroskopischen Vermessung von Rubidium 0-0-CPT-Resonanzen in Abhängigkeit des Ne-Puffergases Druck gezeigt. Diese Vermessung zeigt, dass ein Ne-Puffergas Druck im Bereich von 80 bis 100 Torr die günstigsten CPT-Resonanz Signal Parameter für die Verwendung im CDSM-Sensor liefert.

Die Kollimation des Laser Strahles ist notwendig um die geringste CPT-Resonanz Leistungsverbreiterung zu gewährleisten. Daher wurde ein "Laser Kollimations Kontroll-System" konstruiert.

Für einen alternativen Zugang des CPT-Resonanz-spektroskopischen Aufbaues wurde dieser für eine DFB-Laser Diode adaptiert. Dazu war die Konstruktion eines Gehäuses für die Laser Diode notwendig, welches eine präzise Temperaturkontrolle im Bereich einiger mK und die Modulierbarkeit der Laserlicht-Frequenz im GHz-Bereich ermöglicht.

iv

Contents

Contents

1. Introduction

This thesis was written in the course of the CDSM-project at the *Institut für Experimentalphysik* at Graz University of Technology. The goal of this project is to develop and improve the optical scalar magnetometer CDSM, which is suitable for space missions. This magnetometer is build in a cooperation with the *Institut für Weltraumforschung* (IWF), located in Graz.

The magnetometer's working principle is based on the quantum mechanical Coherent Population Trapping (CPT)-effect. Two coherent coupled electromagnetic fields establish so-called Λ-systems e.g. in the vapour of Alkali metals. The ground states of this Λ-system are superposed. By the ground states interference with the incident electromagnetic waves the absorption of the electromagnetic waves is cancelled due to the coherent trapping of the atomic population in a so-called dark state. In an experiment, the dark state is observed by the loss of fluorescence light. The CPT-effect was first observed in 1976 by Alzetta, Gozzini, Moi and Orriols at the University of Pisa.

The Coupled Dark State Magnetometer (CDSM) is based on the combination of pairs of dark states. It uses a glass cell which is containing ^{87}Rb for magnetic field sensing. The dark state resonance frequencies are shifted by a magnetic field, this is called *Zeeman*-effect. By the detection of the resonance shifts, the cell's surrounding magnetic field is determined. The CDSM-sensor cell contains, additionally to the Rb-vapour, a Ne-buffer gas in order to reduce the CPT-resonance linewidth. With this a (doppler broadened) CPT-resonance linewidth below 30 Hz is achievable. This is 10^7-times smaller than a 1-photon absorption linewidth. That highly reduced - with the CDSM detectable - linewidth determines the precision of the instrument.

The CDSM uses a direct laser current modulated Vertical Cavity Surface Emitting Laser (VCSEL) diode to produce the coherently coupled electromagnetic fields. The laser beam's collimation influences the accuracy of the CDSM. Therefore a device - the Laser Collimation Control (LCC) assembly - is designed to ensure the laser beam's collimation, which is shown in section 6.3.

In order to improve further the accuracy of the CDSM a CPT-resonance spectroscopy setup featuring a Distributed Feedback (DFB)-laser diode as a light source is of interested. For this DFB-laser a custom diode housing is designed for a precise temperature control in the range of a few mK and a direct laser current modulation capability up to a few GHz. This is shown in section 7, combined with an optical, thermal and electrical characterisation of the DFB-laser with the designed housing.

In section 6.2 the measurement automation of a CPT-resonance spectroscopy setup with the help of LabView is described. Therefore a microwave generator and a lock-in amplifier are remote controlled by a PC. The data is recorded and can be analysed with a custom analysis tool.

The CDSM-sensor cell contains, additionally to the Rb-vapour Neon, as a buffer gas. The LabView automation was used to investigate the influence of different Ne-buffer gas pressures on the CPT-resonance frequency, the CPT-resonance linewidth and the CPT-resonance amplitude. The results are shown in chapter 8.

The CDSM-instrument is going to be lunched in 2016 in the *Chinese Electro-Magnetic Satellite* (EMS) which will orbit the earth.

In 2022 the CDSM will be lunched at the ESA's *Jupiter icy moons explorer* (JUICE) mission. The goal is to investigate Jupiter and its moons Ganymede, Callisto, and Europa. The magnetic field detection is used to determine the presence of internal habitable liquid-water oceans under the moon's icy surfaces.

2. Coherent Population Trapping

The effect of Coherent Population Trapping (CPT) occurs in the simplest case in 3-level atomic quantum systems coupled by two electromagnetic (EM) waves. It is a quantum interference phenomenon with a macroscopic-visible quantum effect, the dark state. This can be measured by detection of the transmitted or emitted light.

2.1. Quantum Mechanical Treatment

Such a 3-energy level-system is displayed in figure 2.1, its name (Λ-system) was inspired by its shape. There are three different energy eigenstates in this simplified model $|1\rangle$, $|2\rangle$ and $|3\rangle$. With the energy-differences $\hbar\omega_{13} = \mathcal{E}_3 - \mathcal{E}_1$ between $|3\rangle$ and $|1\rangle$ and $\hbar\omega_{23} = \mathcal{E}_3 - \mathcal{E}_2$ between $|3\rangle$ and $|2\rangle$. The dipole-transition-matrix elements between the two lower energy levels (ground levels) shell be zero. The decay rates from $|3\rangle$ to the lower states are labelled with γ_1 and γ_2.

This system is described by its stationary Hamiltonian $\hat{H}_0$ and by its wave function $|\psi(r,t)\rangle$. The time-evolving system can be expressed by

$$|\psi(r,t)\rangle = \sum_{n=1}^{3} c_n \cdot e^{-i\frac{\mathcal{E}_n}{\hbar}t} |n\rangle. \tag{2.1}$$

By considering perturbation theory (2.2), weak changes in this quantum system can be introduced.

$$\hat{H}(r,t) = \hat{H}_0 + \hat{V}(r,t) \tag{2.2}$$

Where $\hat{H}(r,t)$ is the new Hamiltonian and $\hat{V}(r,t)$ represents possible disturbances. Two EM excite the Λ-system and are considered as disturbing influence $\hat{V}(r,t)$. The allowed transition probabilities from one to another state are described by the dipole operator $\hat{d}$, the dipole operator couples the atom and the electric field. So the disturbance can be written as:

$$\hat{V}(r,t) = -\hat{d} \cdot \vec{E}(r,t) \tag{2.3}$$

The bichromatic electromagnetic field is assumed in a form of the superposition of two monochromatic plane waves (linear polarisation) only the electric field components are considered because of the dominating role of the dipole-transitions:

$$\vec{E}(t,\vec{r}) = E_{0,1}\vec{e}_1 e^{-i(\omega_1 t + \vec{k}_1\vec{r}) + i\phi_1} + E_{0,2}\vec{e}_2 e^{-i(\omega_2 t + \vec{k}_2\vec{r}) + i\phi_2} \tag{2.4}$$

$E_{0,i}$ is the amplitude of the electric field with its frequency ω_i, phase ϕ_i and $\vec{k}_i$ the wave vectors.

The photon frequency mismatch to its resonance frequency is called detuning and is labelled in figure 2.1 with $\Delta_1 = \omega_1 - \omega_{13}$ and $\Delta_2 = \omega_2 - \omega_{23}$. By considering only one of the excitations, $|i\rangle$ to $|3\rangle$, the *Rabi frequency* g_i is introduced. This quantity describes the transition strength in units of a frequency.

$$g_i = -\frac{\langle 3| \, d_{i3} \, |i\rangle}{\hbar} E_{0,i} \tag{2.5}$$

For convenience the Raman detuning is used with $\Delta_R = \omega_{13} - \omega_{23} - (\omega_1 - \omega_2)$. It describes how the energy difference between the two incident waves $(\omega_1 - \omega_2)$ matches the energy splitting of the two ground states $|1\rangle$ and $|2\rangle$. Γ describes decaying processes which result in a dephasing and a loss of coherence of the two involved lower states. Using the definition of the light-atom interaction Hamiltonian (2.3) with the electric field in (2.4) and by considering the rotating wave approximation [17] by ignoring none-resonant terms, the light-atom interaction Hamiltonian can be written as

$$\hat{V} = \hbar g_1 e^{-i\omega_1 t + i\phi_1} |3\rangle \langle 1| + \hbar g_2 e^{-i\omega_2 t + i\phi_2} |3\rangle \langle 2| + h.c. \tag{2.6}$$

By a special unitary transformation it is possible to find a dark state which is decoupled from the other two states. This is shown in section 2.3 in order to illustrate the CPT effect. Although this Ansatz does not include the decaying processes γ_1, γ_2 and Γ. Therefore the density matrix formalism is used to include these features of "real" quantum systems.

Figure 2.1: Schematic representation of the three energy levels of the Λ-system, noted with $|i\rangle$. ω_{ij} is the energy difference between the states i and j, and ω_i indicates the possible excitation channels. γ_i is the decay rate from $|3\rangle$ into $|i\rangle$. Γ describes the loss of coherence between the ground states $|1\rangle$ and $|2\rangle$. Δ_i symbols the photonic frequency detuning to the atomic states and Δ_R the Raman-detuning.
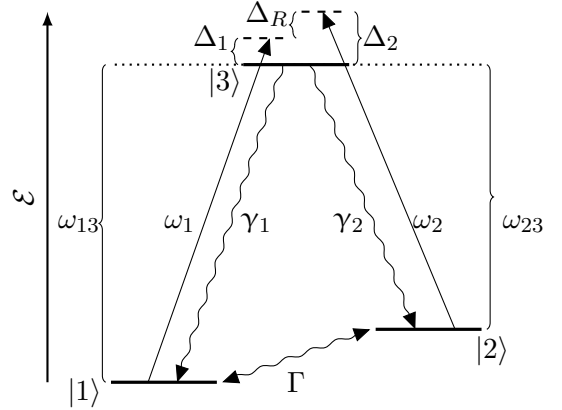
2.1.1. Density Matrix Formalism

In open quantum-systems, which are coupled to a thermal reservoir, not all atoms are in the same quantum state. There is a certain distribution of different atomic configurations and these change over time, this called mixed system [27]. In order to handle systems like this, the density matrix formalism is used. The density matrix formalism combines quantum mechanics with statistical methods to handle statistical

ensembles of quantum states. The density operator is defined as:

$$\hat{\rho} := \sum_i p_i \left| \psi_i \right\rangle \left\langle \psi_i \right| \tag{2.7}$$

It is the sum over all possible projections for $\left| \psi_i \right\rangle$, weighted with their classical probability p_i.

By assuming there is only one state, ψ_i turns into ψ, which can be written in its basis as $\psi = \sum_n c_n \left| n \right\rangle$. $\left| n \right\rangle$ are its basis vectors with their coefficients c_n. Using (2.7) as $\hat{\rho} = \left| \psi \right\rangle \left\langle \psi \right|$ the following form is achieved

$$\hat{\rho} = \sum_n \sum_m c_n c_m^* \left| n \right\rangle \left\langle m \right| = \sum_{n,m} \rho_{nm} \left| n \right\rangle \left\langle m \right|. \tag{2.8}$$

with $c_n c_m^* = \rho_{nm}$. The diagonal element ρ_{nn} is the probability to find $\left| n \right\rangle$ in a measurement. In a statistical sense they can by considered as population. The off-diagonal elements on the other hand are associated with the coherences between the states $\left| n \right\rangle$ and $\left| m \right\rangle$. To show this, the coefficients are expressed in their polar form as $c_n = r_n e^{-i\phi_n}$ and $c_m^* = r_m e^{i\phi_m}$. This leads to $\rho_{nm} = r_n r_m e^{-i(\phi_n - \phi_m)}$. From this the dephasing becomes clear with $\Delta\phi_{nm} = \phi_n - \phi_m$.

With the off-diagonal elements the phase relation between different quantum eigenstates are described. These play an important role in quantum optics because the observable effects are highly depended on coherence or decoherence.[27]

For the general case of a mixed system, the density operator $\hat{\rho}$ in (2.7) can be interpreted as mixed state with $\left| \psi_i \right\rangle = \sum_n c_{n,i} \left| n \right\rangle$. These mixed states can not be written as a state vector, they must be treated statistically.

The density matrix has some properties:

Normalisation condition:

$$\sum_n \rho_{nn} = Tr(\hat{\rho}) = 1 \tag{2.9}$$

For a closed system is $Tr(\hat{\rho}) = 1$ and for a open system $Tr(\hat{\rho}) \leq 1$

Triangle inequality:

$$\left| \rho_{nm} \right|^2 \leq \rho_{nn} \cdot \rho_{mm} \tag{2.10}$$

The matrix is Hermitian:

$$\rho_{nm} = \rho_{mn}^* \tag{2.11}$$

Expectation value of an operator $\hat{A}$:

$$\left\langle \hat{A} \right\rangle = \sum_n \sum_m c_n c_m^* \left\langle m \right| A \left| n \right\rangle = Tr(\rho A) \tag{2.12}$$

By taking the time-derivative of (2.7) and using the time-depended Schrödinger equation the *von Neumann* or *Liouville* equation is achieved:

$$\frac{\partial}{\partial t} \hat{\rho} = -\frac{i}{\hbar} \left[\hat{H}, \hat{\rho} \right] \tag{2.13}$$

This is an equation of motion for quantum systems [27]. Although this equation does still not include decaying processes. To include them it is necessary to add the Relaxation Operator $\hat{R}$ [4], see equation (2.14). Here all de-phasing and relaxation processes can be included in the mathematical model of the Λ-System. This is a convenient way to include the missing decaying processes (Γ, γ_1 and γ_2) which are displayed in figure 2.1.

$$\frac{\partial}{\partial t}\hat{\rho} = -\frac{i}{\hbar}\left[\hat{H}, \hat{\rho}\right] - i\hat{R}\hat{\rho} \tag{2.14}$$

2.1.2. The Λ-System described with the Density Matrix Formalism

For the Λ-system in figure 2.1 the single elements of $\frac{\partial}{\partial t}\hat{\rho}_{nm} = \langle n|\frac{\partial}{\partial t}\hat{\rho}|m\rangle$ can be expressed as

$$\dot{\rho}_{nm} = -\frac{i}{\hbar}\sum_{k=1}^{3}(H_{nk}\rho_{kn} - \rho_{km}H_{mk}) - i(\hat{R}\hat{\rho})_{nm} \tag{2.15}$$

with the equations [3]:

Polpulation evolution:

$$i\dot{\rho}_{11} = -g_1\rho_{31}e^{i\Delta_1 t - i\vec{k}_1\vec{r}} + 2i\gamma_1\rho_{33}$$

$$i\dot{\rho}_{22} = -g_2\rho_{32}e^{i\Delta_2 t - i\vec{k}_2\vec{r}} + 2i\gamma_2\rho_{33}$$

$$i\dot{\rho}_{33} = g_1\rho_{31}e^{i\Delta_1 t - i\vec{k}_1\vec{r}} + g_2\rho_{32}e^{i\Delta_2 t - i\vec{k}_2\vec{r}} - 2i(\gamma_1 + \gamma_2)\rho_{33}$$

Coherence evolution:

$$i\dot{\rho}_{13} = -g_1(\rho_{33} - \rho_{11})e^{i\Delta_1 t - i\vec{k}_1\vec{r}} + g_2\rho_{12}e^{i\Delta_2 t - i\vec{k}_2\vec{r}} - i(\gamma_1 + \gamma_2)\rho_{13}$$

$$i\dot{\rho}_{23} = -g_2(\rho_{33} - \rho_{22})e^{i\Delta_2 t - i\vec{k}_2\vec{r}} + g_1\rho_{21}e^{i\Delta_1 t - i\vec{k}_1\vec{r}} - i(\gamma_1 + \gamma_2)\rho_{23}$$

$$i\dot{\rho}_{12} = -g_1\rho_{32}e^{i\Delta_1 t - i\vec{k}_1\vec{r}} + g_2\rho_{13}e^{-i\Delta_2 t + i\vec{k}_2\vec{r}} - i\Gamma\rho_{12}$$

$$\tag{2.16}$$

$\Delta_i = \omega_i - \omega_{3m}$ are the frequency detunings and γ_i the partial decay rates. Γ describes the relaxation of the coherence ρ_{12} between the ground state.

The population of ρ_{11} and ρ_{22} is directly increased by the decay from $|3\rangle$ with the rates γ_1 and γ_2. By the substitution of the equations

$$\rho_{m3} := \rho_{m3,r}e^{i\Delta_m - i\vec{k}_m\vec{r}}$$

$$\rho_{12} := \rho_{12,r}e^{i(\Delta_1 - \Delta_2)t - i(\vec{k}_1 - \vec{k}_2)\vec{r}} \tag{2.17}$$

the behaviour of the off-diagonal coherence elements is described. The amplitudes $\rho_{ij,r}$ correspondent to their ρ values at resonance. It is assumed, that the elements ρ_{m3} oscillate with their detuning. $\vec{k}_1 - \vec{k}_2$ takes the spatial relation of the two photons into account.

The solutions to this differential equation system is very complex and shell not be given here, these are publishes in several papers, e. g. [6] and [33].

By applying some assumptions (the Λ-system is at rest, equal detuning $\Delta_1 = \Delta_2 = \Delta$, equal decay rates $\gamma_1 = \gamma_2$ and equal Rabi-frequencies $g_1 = g_2 = g$) an analytic expression for the time-independent population ρ_{33} can be found [3]. ρ_{33} is of interest because it is proportional to the fluorescent light. These solutions are the steady-state solutions for the symmetric Λ system. The population as a function of the single frequency detuning is plotted in figure 2.2. The use of the normalised Raman detuning $\Delta_{R,n}$ allows to set the full width at half maximum (FWHM) to 2. One frequency ω_1 or ω_2 is held constant at its resonance while the other is scanned. This corresponds to measurement techniques, shown in section 6.1 about spectroscopic techniques.
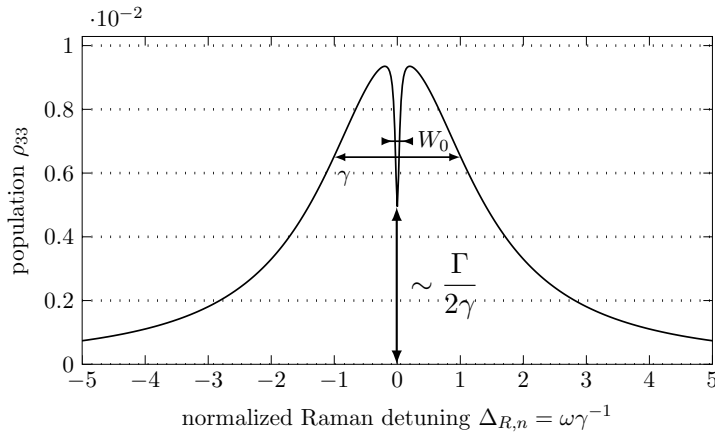
Figure 2.2.: The population ρ_{33} of the $|3\rangle$ energy level as a function of normalized Raman detuning. The FWHM is set to 2. For an ideal CPT, $\rho_{33}(R = 0) = 0$ and the dip's bottom goes to 0. The loss of ground-state coherence determines the depth of the dip.

2.2. CPT-Resonance Features

Figure 2.2 shows the population of the highest energy state $|3\rangle$ (compare figure 2.1). When one frequency is tuned towards its resonance the population increases following the Lorentzian line shape profile like the regular absorption in the case of a single transition excitation (2-level-system) [4]. But close the expected maximum, the population drops rapidly. Now the population is transferred directly between the lower states $|1\rangle$ and $|2\rangle$. Population trapping occurs. In experiments a strong decrease of the resonance fluorescence is detected. This absence of fluorescence inspires the name "dark resonance" at the "dark state". The width of the characteristic sharp dip is [3]

$$W_0 \approx \Gamma + \frac{g^2}{\gamma_1 + \gamma_2} \tag{2.18}$$

2.2. CPT-Resonance Features

This linewidth W_0 can be much smaller than the natural linewidth $\gamma = \gamma_1 + \gamma_2$ of $|3\rangle$. In experiments, a linewidth of 100 to 500 Hz is measured, compared to 16 MHz of the natural linewidth. The depth of the valley is determined by the ratio of $\Gamma/2\gamma$.
A certain laser intensity is necessary

$$I \gg I_n \frac{\Gamma}{\gamma} \tag{2.19}$$

in order to observe CPT [3]. With I_n the saturation intensity for the corresponding optical transition. For ^{87}Rb the value for Γ is in the range of 20 to 1000 s^{-1} in cells containing Ne as buffer gas (several kPa pressure) additional to the Rb-vapour.
For small intensities is the susceptibility χ connects the electric field E with the polarisation P. The simplest approximation is to assume a linear relation with the generalised (complex) susceptibility [27]:

$$P(\omega_L) = \epsilon_0(\chi'(\omega_L) + i\chi''(\omega_L))E(\omega_L) \tag{2.20}$$

This is the system's dipole response to an electric perturbation induced by the laser frequencies ω_L [18]. The susceptibility is related with the absorption coefficient α and the index of refraction n by

$$(n + i\alpha)^2 = 1 + \chi \ . \tag{2.21}$$

With this equation and $\chi = \chi' + i\chi''$ the following is derived [20]:

$$\alpha(\omega_L) = \frac{\chi'(\omega_L)}{2n(\omega_L)} \tag{2.22}$$

$$n = \frac{1}{2}\left[1 + \chi'(\omega_L) + \sqrt{(1 + \chi'(\omega_L))^2 + (\chi''(\omega_L))^2}\right] \tag{2.23}$$

The absorption is mainly dependent on the imaginary and the refractive index mainly in the real part of χ. If χ' and χ'' is zero, than $n = 1$ and $\alpha = 0$ [17]. So the medium becomes transparent for the frequency ω_L. This occurs for the resonance frequency in figure 2.2. This effect is called electromagnetically induced transparency (EIT).
The optical polarisation can also be expressed as

$$P(\omega_L) = N\langle \hat{d} \rangle = N \cdot Tr(\hat{\rho}\hat{d}) = N(d_{13}\rho_{13} + d_{23}\rho_{23}) \tag{2.24}$$

with N the density of absorbing atoms and d_{i3} the dipole operator elements. The total polarisation is just the polarisation of one atom times their number. Combining booth equations (2.20) and (2.24), the real and imaginary part of χ are derived:

$$\chi'(\omega_L) = \frac{N}{2\epsilon_0 \hbar E}(d_{i3}\rho_{i3})$$
$$\chi''(\omega_L) = \frac{N}{2i\epsilon_0 \hbar E}(d_{i3}\rho_{i3}) \tag{2.25}$$

The real and imaginary parts of ρ_{i3} are plotted in figure 2.3, with the equations found in [27]. The spectral features of figure 2.2 are also present in the measurements of n and α. Their line shapes are Lorentzian formed too. In order to model the line shapes in 2.3 it is convenient to use a sum of a so called absorptive and a dispersive Lorentzian profile[24].
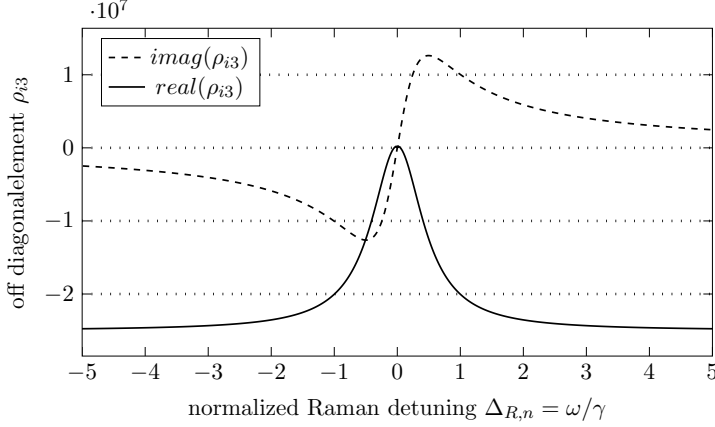
Figure 2.3.: Imaginary (dashed) and real (straight) part of the off diagonal element ρ_{i3} for a symmetric Λ system as a function of the normalized Raman detuning $\Delta_{R,n}$. The real part correspondents with the medium's absorption α, the imaginary part with the index of refraction n. Close to the resonance ($\Delta_{R,n} = 0$), $\alpha = 0$ and $n = 1$[17] which leads to electromagnetically induced transparency (EIT).

2.3. Analytic Description of the CPT-Effect

In order to understand the effect of CPT it is convenient to introduce a new orthogonal system basis set of a coupled $|C\rangle$, a noncoupled state $|NC\rangle$ and $|3\rangle$[4]. By a unitary transformation this new basis is produced from the previous one ($|3\rangle$, $|2\rangle$ and $|1\rangle$).

$$|C\rangle = \frac{g_1}{g}|1\rangle + \frac{g_2}{g}|2\rangle$$
$$|NC\rangle = \frac{g_2}{g}|1\rangle - \frac{g_1}{g}|2\rangle \tag{2.26}$$
$$\text{with}$$
$$g = \sqrt{g_1^2 + g_2^2}$$

Both states are a linear combination of the ground states, a superposition of two quantum states. With the equation (2.6) and the $|NC\rangle$ state the transition probability can be calculated:

$$\langle 3|\hat{V}|NC\rangle = \frac{\hbar g_1 g_2}{g}e^{-i\omega t}\left(e^{i\phi_1} - e^{i\phi_2}\right) \tag{2.27}$$

The small frequency difference of ω_1 and ω_2 is assumed to be 0 for the next considerations, otherwise a beat signal is superposed. So $\omega_i = \omega$, this frequency is now the resonance frequency of the Λ system.

This $\langle 3|\hat{V}|NC\rangle$ matrix element is only 0 for equal phases of the two incident electromagnetic waves, so no excitation is possible although ω is at resonance. This state becomes decoupled from the rest of the system and so the atoms are trapped in this

stable configuration. No excitation is possible from this "dark state". There is also no spontaneous emission neither to $|3\rangle$ nor to $|C\rangle$ by which the atoms could leave $|NC\rangle$. But small changes of the phases lead to loss of coherence and the transition to $|3\rangle$ becomes possible. The relative phase of the laser fields plays an important role in the noncoupled state's evolution.

In the case of coherence ($\phi_1 = \phi_2 = \phi$) the evaluation of the transition element from $|C\rangle$ to $|3\rangle$ is

$$\langle 3| \hat{V} |C\rangle = \hbar g e^{-i\omega t + i\phi}. \tag{2.28}$$

If the decay γ is neglected, the initial prepared population of $|NC\rangle$ is unchanged and there is population transfer between $|3\rangle$ and $|C\rangle$ over time.

Although if these decaying processes are included, it can be shown [4] that the γ rates are equal for the decay to the new ground-states. Spontaneous emission from $|3\rangle$ populates the new states $|C\rangle$ and $|NC\rangle$. So a pumping process is established, when the Λ system interacts with the resonant laser fields. Atoms, in the $|C\rangle$ state gets exited to $|3\rangle$ and decay equally into $|C\rangle$ and $|NC\rangle$. The atoms in $|NC\rangle$ are trapped and a smaller number of the initial states end up in $|C\rangle$, there the absorption and decaying cycle starts again. So, over time, all atoms get trapped in $|NC\rangle$ and no absorption takes place in the system. The medium becomes transparent for the resonance frequencies. This effect strongly depends on the coherence of the laser fields, as shown for the transition element $\langle 3| \hat{V} |NC\rangle$ in equation (2.27). Every little disturbance of the coherence results in a nonzero transition element. In the density matrix approach, this disturbances are combined in the ground state relaxation rate Γ which couples the $|C\rangle$ and $|NC\rangle$. This leads to a specific lifetime of $|NC\rangle$. The higher Γ, the less number of atoms are trapped in the noncoupled state and this determines the depth of the dip in figure 2.2.

These relaxation processes have different sources: the atomic flight through the laser beam defines the interaction time, atomic polarisation and coherence damping by collisions and velocity changing collision [5]. Another way to describe the CPT effects is done by the method of "second quantisation" [4].

2.4. Λ-Systems in Atoms due to Laser Excitation

The CPT effect occurs in Λ systems which have a high ground-state live time, therefore the hyperfine ground states of different atoms are suitable for experiments. Mostly used are the vapors of alkali-atoms. One requirement is, that the Raman condition is fulfilled: the energy difference of the two incident laser must match the energy splitting of the ground states [18]. The absolute frequency detuning results in a reduction of the resonance amplitude.

For experiments the relative phase stability of both components of the dichromatic EM light field (see (2.4)) determines ground state coherence and so the width W_0 of the dark state.

In the atomic level configuration the Λ-system is normally surrounded by other atomic levels, which are not part of the Λ configuration. In this multilevel systems the ground

state coherence can be destroyed by optical excitation into these additional states by one-photon absorption or by the formation of additional Λ-systems, which interfere destructively [49]. In all the performed experiments, ^{87}Rb was used as a "CPT-medium". It is confined in a glass cell as vapour, its pressure is determined by the rubidium's vapour pressure curve. For 30°C it is approximately $4 \cdot 10^{-7}$ Torr [44]. Additionally Ne is added to the cell as buffer gas in order to minimize the CPT-linewidth, see section 2.4.2.

2.4.1. Rubidium for Spectroscopy and Quantum Optical Experiments

The rubidium isotope ^{87}Rb is widely used in quantum optical experiments, therefore the understanding of its interaction with light is important. A very detailed description of this atom can be found in the paper "Rubidium 87 D Line Data" [44]. The following information is based on this paper. Extra sources are noted explicitly.
The notation of an atomic state in terms of its quantum numbers is

$$\text{n}\ ^{2S+1}\text{X}_J. \tag{2.29}$$

The number n is the main quantum number. $2S + 1$ is the multiplicity, it indicates the number of possible orientations of the spin $\vec{S}$ and the orbital angular momentum $\vec{L}$, the number of degenerate wave functions and so the number of fine structure splittings. X symbols the orbital angular momentum number for L, with S(L=0), P(L=1), D(L=2)... . The magnetic quantum number m is not included in this notation. [12]
By the coupling of the orbital angular momentum $\vec{L}$ of the outer electron and its spin angular momentum $\vec{S}$, the total electron angular momentum can be expressed as

$$\vec{J} = \vec{L} + \vec{S}. \tag{2.30}$$

The quantum number J has the range of

$$|L - S| \le J \le L + S \tag{2.31}$$

and $|\vec{J}| = \hbar\sqrt{J(J+1)}$. J is used as a index of the symbol X.
For rubidium the outer-electron ground-state is $5\ ^2\text{S}_{1/2}$ ($L = 0$, $S = 1/2$, $J = 1/2$) and the first exited state splits up in to separate levels, $5\ ^2\text{P}_{1/2}$ ($L = 1$, $S = 1/2$, $J = 1/2$) and $5\ ^2\text{P}_{3/2}$ ($L = 1$, $S = 1/2$, $J = 3/2$). Transitions from the ground state $L = 0$ to the first exited state $L = 1$ are labelled with D. There are two D-lines, from $5\ ^2\text{S}_{1/2}$ to $5\ ^2\text{P}_{1/2}$ called D_1 and from $5\ ^2\text{S}_{1/2}$ to $5\ ^2\text{P}_{3/2}$ called D_2.
The hyperfine structure (hf) is produced by the coupling of $\vec{J}$ with the total nuclear angular momentum I.

$$\vec{F} = \vec{J} + \vec{I} \tag{2.32}$$

The total atomic angular momentum quantum number F allows the following quantum numbers:

$$|J - I| \le F \le L + I \tag{2.33}$$

Which results in a additional energy splitting of the levels. For the quantum numbers of the ground state $J = 1/2$ and $I = 3/2$, these new levels are labelled with $F = 1$ and $F = 2$. The hyperfine states of the ground state $5\ ^2S_{1/2}$ can be treated as the states $|1\rangle$ and $|2\rangle$ of the Λ-system. For the excited state $|3\rangle$ either $5\ ^2P_{1/2}$ or $5\ ^2P_{3/2}$ are suitable to accomplish a Λ-system. So both, the D_1 and D_2 line can be used for CPT-experiments.

The experiments, which were done as part of this thesis, only deal with the D_1-line. Although the D_2 is more often used in quantum optical application, because of its cycling transition in cooling and trapping, the D_1 is used for magnetometry due to its lower number of excited state splittings, which results often in a smaller linewidth W_0 [17].

The energy shift of an hyperfine substate with respect to the fine structure state can be written as

$$\Delta E_{hfs}(F) = \frac{1}{2}A_{hfs}K + B_{hfs}\frac{\frac{3}{2}K(K+1) - 2I(I+1J(j+1))}{2I(2I-1)2J(J-1)} \tag{2.34}$$

with A_{hfs} the magnetic dipole constant of the nucleus, B_{hfs} the electric quadrupole constant (relevant only for the D_2, but zero for $J = 1/2$ levels) and

$$K = F(F+1) - I(I+1) - J(J+1). \tag{2.35}$$

In figure 2.4 an absorption spectrum of the D_1-line is shown, which was observed using tunable laser light generated by a laser diode. The laser light's frequency was sweep through the features to measure the absorption of the gas. The individual atomic transitions are labelled.

In figure 2.5 the Rb states, which are linked to the Λ-systems of the D_1-line, are drawn. The resonance wavelength between the fine structure splitting is in the infra red (IR) regime at $\lambda = 794.978$ nm (vacuum wavelength). The ground state hyperfine splitting is $\nu_{HFS,S} = 6.8347$ GHz and the splitting of the first excited state $\nu_{HFS,P} = 816.66$ MHz [38]. If a magnetic field is applied, each single F state splits up in $2F + 1$ magnetic sublevels, which are labelled with m_F. When there is no field, the single F states are degenerated. For weak magnetic fields, the sublevel split can be linearly approximated with

$$\Delta E_{|Fm_F\rangle} = \mu_B g_F m_F B. \tag{2.36}$$

B is the magnetic field strength, μ_B the permeability, g_F the Landé g-factor and m_F the magnetic quantum number. The splitting of spectral lines in magnetic fields is called *Zeeman* effect. For intermediate fields and states with $J = 1/2$ the *Breit-Rabi* formula is used to describe energy shifts of the magnetic sublevels. For the two states with $m = \pm(I + 1/2)$ the

$$E_{|J=1/2\ m_J\ I\ m_I\rangle} = \frac{\Delta E_{hfs}}{2I+1} \pm \frac{1}{2}(g_J + 2Ig_I)\mu_B mB \tag{2.37}$$

is used to calculate the energy shift. m_i is the specific eigenvalue of the specific angular momentum.
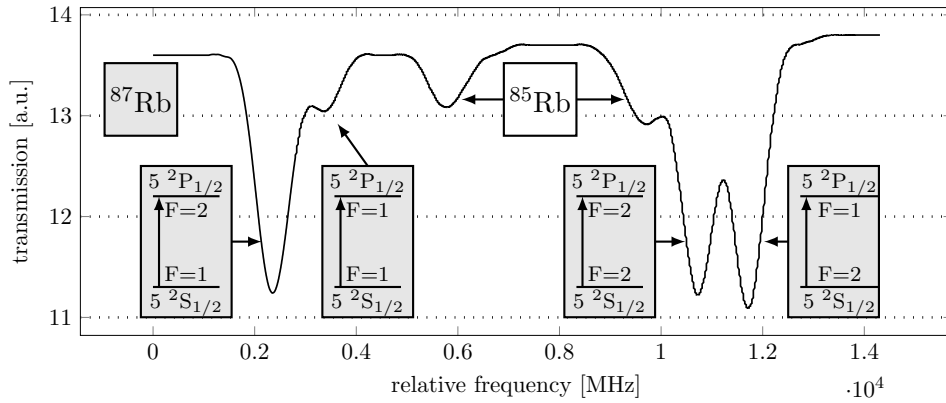
Figure 2.4.: Absorption spectrum showing the Rb D_1-line. The vapour consists mainly of the ^{87}Rb isotope but small amounts of the ^{85}Rb are present. The one-photon transitions are labelled and correspondent to the energy-level diagram in figure 2.5. The data is taken from [17]. Light generated by a so-called VCSEL-diode was used.
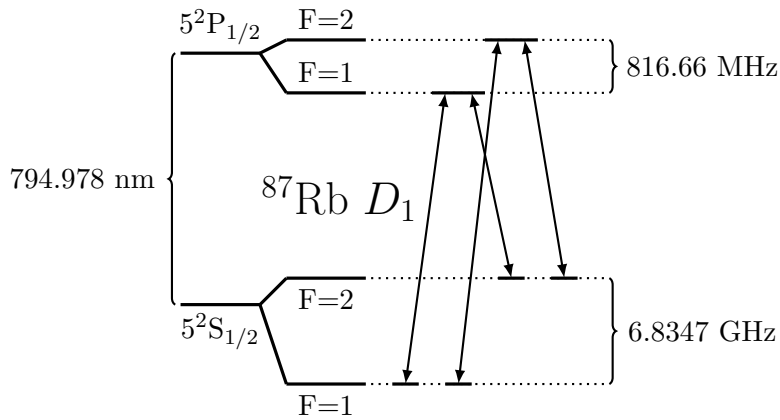
Figure 2.5.: The two possible Λ-systems of the ^{87}Rb D_1-line in the case of zero magnetic field $|\vec{B}| = 0$. The hyperfine splitting of the S-configuration acts as the ground-state for both Λ-system. The P-splitting allows two different systems. The magnetic sublevels are assumed to be zero for both ground-states, so these resonances are label with 0-0.

In experiments, the 0-0-CPT-resonance is often investigated. The numbers 0-0 indicate the magnetic quantum number $m_F = 0$ of the two ^{87}Rb ground states (see figure 2.5). This 0-0-resonance *Zeeman* frequency shift is quadratically depended on the magnetic flux density B [44][17]. This frequency shift is

$$\Delta\nu(B) = \frac{(g_J - g_I)^2 \mu_B^2}{2\hbar\Delta E_{hfs}} = 575.14 \cdot 10^8 \cdot B^2. \tag{2.38}$$

For a small magnetic field density of $B = 7.9$ µT the induced 0-0-resonance frequency shift is $\nu_B = 3.6$ Hz, see section 8.2.

2.4.2. Buffer Gas

The ground-state relaxation rate determines the linewidth of the CPT-resonance. In experiments, besides the laser phase stability, this is mostly dependent on the residence time of the Λ-atoms within the laser beam. An additional buffer-gas will lead to a diffusive motion which increases the interaction time up to a few milliseconds. The special choice of neon (no net spin, very small polarisation) will allow to preserve the ground-state coherence over a high number of collisions [49]. So a linewidth of 30 Hz [18] can be achieved for Rb and 42 Hz for Cs [49]. A negative side-effect is that the optical transitions are strongly broadened up to several 100 MHz for a few kPa buffer-gas pressure.

The interaction of the CPT-atoms with the neon atoms also results in blue-shift of the resonance frequency. A shift of (4.80 ± 0.10) Hz/Pa was found for Cs atoms with neon buffer gas [49]. An additional effect arises through the buffer-gas, the amplitude of the CPT-resonance shows a strong temperature dependence. The total shift [48] can be approximated with

$$\nu(T) = \nu_0 + P(c_1 + c_2\Delta T + c_3\Delta T^2). \tag{2.39}$$

The c_i are the fit parameters, ν_0 the resonance frequency of buffer-gas less cell and P is the buffer-gas pressure. Heating the gas increases the number of interacting atoms with the laser light. Although when a certain temperature is reached the signal is reduced due to the increasing optical thickness of the gases. For a Cs vapor with neon as buffer gas (5 kPa) the amplitude dropped at 65°C rapidly [25]. For increasing laser intensities a linear broadening of the CPT linewidth W_0 (see equation 2.18) is observed, this is called *Power Broadening* [19].

2.5. Coupled Dark State Magnetometer

The Coupled Dark State Magnetometer (CDSM) is an optical pumped scalar magnetometer which is based on the spectroscopy of free alkali atoms. This magnetometer is specially designed for scientific space missions [38] [37].

A ^{87}Rb-vapour cell with neon as buffer gas is used as the magnetic field sensor. In the presence of a magnetic field the spectral lines are split by the *Zeeman* effect, according to their m_F quantum number, into several components. As a consequence, several Λ-systems are established within these split components [50]. These Λ-systems result in the appearance of CPT-resonances, which can be used as precise spectroscopic markers.

The CPT-resonance occurs as a narrow dip at the exact resonance frequency of the Doppler broadened spectral lines, which linewidth is approximately 500 MHz [13]. The CPT-linewidth of this narrow dip is 50 to 1000 Hz, depending on the setup's parameters (e.g. the beam's intensity, the laser beam diameter and the buffer gas pressure). By (frequency-)tracking this small spectral features, a CPT-resonance shift, which is introduced by a magnetic field change, can be measured with a high resolution.

The CDSM combines pairs of equal resonance number $n = |m_{F1} + m_{F2}|$-number of the CPT-resonances (between different *Zeeman*-shifted levels) to enable a high dynamic range up to 1 mT without loss of B-field sensitivity and guaranties a so-called deadzone free detection of the magnetic field's magnitude [38]. This feature is superior to other types of scalar magnetometers.

Further, the pairwise excitation of the CPT-resonances enables to distinguish between unwanted systematic frequency shifts (e.g. temperature induced pressure shift [48]) which acts on all CPT-resonances of the CPT-resonance spectrum and the B-field dependent shift. So the CDSM becomes independent of the sensor's temperature. This is a key feature for space missions where high sensor temperature changes are unavoidable.

For the CPT-resonance detection a multi frequency modulated laser light is guided through a graded index multi mode fibre to the sensor, which is mounted ideally several meters away from the electronic-devices to avoid interference-effects. The magnetic field interacts with the ^{87}Rb-atoms within the sensor (glas-)cell and changes the Rb-vapour's optical properties via the frequency shift of the CPT-resonances. This changes are detectable in the transmitted laser light, which is guided to a photo diode, where an absorptive and a dispersive signal component is derived by a phase-sensitive measurement (lock-in amplifier). From the dispersive signal the magnetic field change is calculated.

The coherent laser light necessary for the establishing of the Λ-system is produced by a VCSEL-diode, which is direct laser current modulated. The method of a double frequency modulation (FM)-modulation of the laser light for CPT-resonance spectroscopy in ^{87}Rb is explained in chapter 6.1.

The CDSM design is used in a magnetometer which will be lunched in 2016 for the Chinese *Electro-Magnetic-Satellite*-Mission. The goal of this mission is to observe the earth's magnetic field.

2.5. Coupled Dark State Magnetometer

The next confirmed mission is the ESA's *Jupiter icy moons explorer* (JUICE)[1] mission. The lunch is planed to be in 2022 with the arrival at Jupiter in 2030. There, a three year observation period of the gaseous planet Jupiter and three of its largest moons, Ganymede, Callisto and Europa will take place. The detection of magnetic fields is key for the determination whether there are liquid water oceans with habitable environments under the icy moon's surfaces of Ganymede, Europa, and Callisto.

---

[1]`http://sci.esa.int/juice/` 14th of December 2015

3. Diode-Laser

The semiconductor laser is the most used laser design in industry. It offers a great number of benefits, like a small form-factor, small power consumption, easy mass-production and direct modulation by current control.

The following description is based on the book *Laser - Bauformen, Strahlführung, Anwendung* from J.Eichler and H.J.Eichler [16]. Other sources are noted explicitly.

3.1. pn Junction

The functionality of the conventional LED and the laser diode originate from the pn-junction. This junction is made of two different doped semiconductors which are connected. One is highly n-doped with N_D, the concentration of donors. The bands are filled up to the Fermi energy, because of its high doping the Fermi energy F_C cuts through the conduction band.

The other semiconductor is highly p-doped with N_A the concentration of acceptors. In this case the Fermi energy F_V cuts through the valence band, a band diagram of this pn-junction is shown in figure 3.1(a).

By diffusion of electrons and electron-holes a depletion width is established but leaves the ions in its crystal position. So there is a positive charge distribution on the n-doped side (positive donor ions are left) and there is a negative charge distribution on the p-doped side (negative acceptor ions are left). This difference in charge results in an electric field which stops the diffusion of the electrons and holes. This electric field produces a potential difference V_D between the different doped zones.

$$V_D \approx \frac{k_B T}{e} \ln \left(\frac{N_A N_D}{n_T^2} \right) \tag{3.1}$$

n_T is the concentration of thermal (at temperature T) excited electrons, witch the charge e, in the intrinsic (non doped) semiconductor. k_B is the Boltzmann-constant. This voltage is often called *build-in voltage* and is inherent for every pn-junction.

This potential difference shifts the energy bands so that both Fermi-energies, F_C and F_D, match, as shown in figure 3.1(a). In (a),there is no bias voltage applied. Applying forward bias voltage reduces the potential difference. This induces the electrons and the holes to move, as a result a diffusion currents flows. The hole-current is in the opposite direction of electron-current. The electron and hole mobility is determines by the specific diffusion constants, so electrons have a much higher mobility. Therefore much more free electrons start to accumulate in the conduction band of the n-doped semiconductor than holes in the valence band of the p-doped semiconductor. So a

(a) No applied bias voltage.

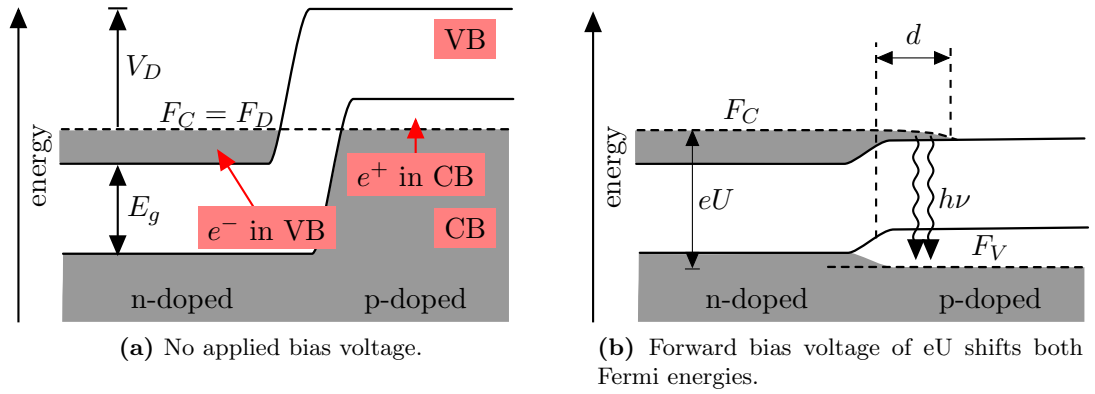**(b)** Forward bias voltage of eU shifts both Fermi energies.

Figure 3.1.: Band diagrams for a pn-junction with no bias voltage (a) and al large forward bias voltage in (b). The bias voltage eU pushes the F_V down and this allows electron-hole recombination which takes place in a small area on the pn-interface.

small area of population inversion is established in the active region. By electron-hole recombination, photons are produced, see figure 3.1(b). Their energy is determined by their recombination energy gap. The thickness d of the active area depends on the recombination time τ and the electron's diffusion constant D.

$$d = \sqrt{D \cdot \tau} \tag{3.2}$$

For GaAs the thickness is $d \approx 1$ μm, with $D = 10$ cm^{2}s^{-1} and $\tau = 10^{-9}$ s [16]. There is a different but fixed band gap for every two component crystal. In GaAs e.g. the band gap is 1.43 eV, which corresponds to an emission of 868 nm. A variable band gap is achieved by combining more elements and varying their mixing ratio.

3.2. Laser Diode Structures

For light amplification a resonator is needed to restrict the electromagnetic waves to certain modes within the active region and to achieve a high density of amplified energy within these modes. The modes overlap with amplification profile of the laser diode. This selects the possible frequencies of the broad gain profile, which has a linewidth of about 10 nm. These modes depend on the length of the resonator L and the semiconductor's index of refraction n. So the resonator's eigenmodes are $\nu = mc/(2nL)$ with m an integer number [13].

The restriction of the active region is done by cutting the semiconducting crystal twice to get two perfectly plane parallel mirrors, the so called Fabry-Perot laser diodes. There is no need of covering these surfaces with a mirroring layer. The material's high refractions index (GaAs: $n = 3.6$) and the transition to air delivers a relative high reflectivity (GaAs: $R = 0.32$) which is sufficient enough for amplification. The other rougher crystal surfaces prohibit the forming of modes in unwanted direction.

A laser with a single pn-junction, like in the previous section, is called homo-structure.

A disadvantage is that the light is not guided through the crystal, there are high losses due to the penetration of light in unwanted areas. To compensate this, high currents are needed to drive this type of laser.

A big improvement was the development of heterostructure devices. Here different semiconductor layers are combined. A schematic drawing is shown in figure 3.2. The
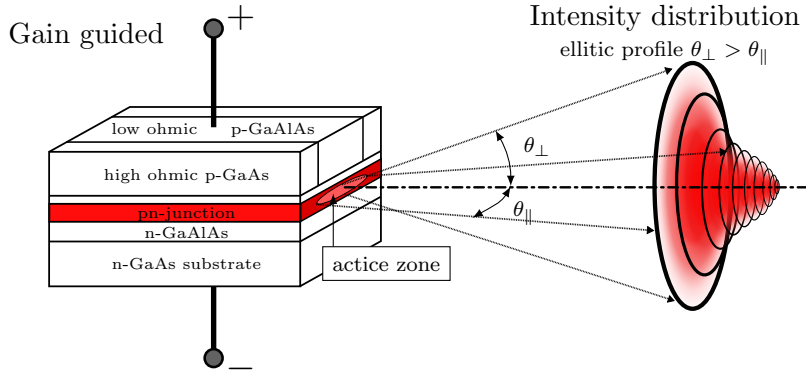

Figure 3.2.: GaAlAs double heterostructure diode laser, the current is gain guided. Due to its drawn out active zone the angle of divergence are different ($\theta_\perp$ and $\theta_\parallel$). This result in an approximately elliptic intensity distribution.

diverse layers have different band gaps and so different refractive indices. At the boarders between the layers, there is a jump in the refractive indices. These act like mirrors and restrict the light within the active zone. So there are less losses, compared to the homostructure and this leads to a reduction of the threshold current by a factor of 100. By further reduction of the active zone it is possible to guide the current explicitly through the semiconductor crystal, this is also shown in figure 3.2. This is done by making small low ohmic contacts within the high ohmic bulk. This *gain guided* structure reduces the power consumption and the threshold current. The light amplification takes place in a narrower active region which only allows the propagation of the transversal ground mode.

An improvement of this design by a further reduction of the active zone via index guiding reduces the threshold current to about 10 mA at room temperature.

3.3. Beam and Emission Characteristics

The shape of the active zone influences the laser beam because of its very narrow cross-sections, compare with figure 3.2. This leads to diffraction at the crystal surface and so divergent beams are emitted. Ideally, the beams can be considered as Gaussian, with the opening angle θ_0, the waist-width $2\omega_0$ and the wavelength λ. For Gaussain beams, see chapter 4.1. An approximation for large distances from the emission source can be

made:

$$\theta_0 = \frac{\lambda}{\pi \omega_0} \tag{3.3}$$

The cross-section of a DFB-laser's active zone has nearly the shape of a rectangular. Therefore two "extremum" angles of divergence are formed by diffraction. This influences the intensity distribution of the radiated light. This nearly elliptic pattern is shown schematically in figure 3.2.

For further applications focusing or collimation of the laser beam is necessary. This is achieved by different types of lenses and optical elements for beam-shaping. More information, concerning Gaussian beam features is brought in section 4.1.

In figure 3.3 the optical output power as a function of the laser current is shown. There are two emission regimes, separated by the threshold current I_{th}. When this current is reached, the regular broad LED emission switches to laser emission. The spontaneous emission gets dominated by the induced, so laser operation becomes possible.

By assuming that a constant part of the injected electrons is responsible for photon emission, the linear behaviour of the optical power can be explained. The output power
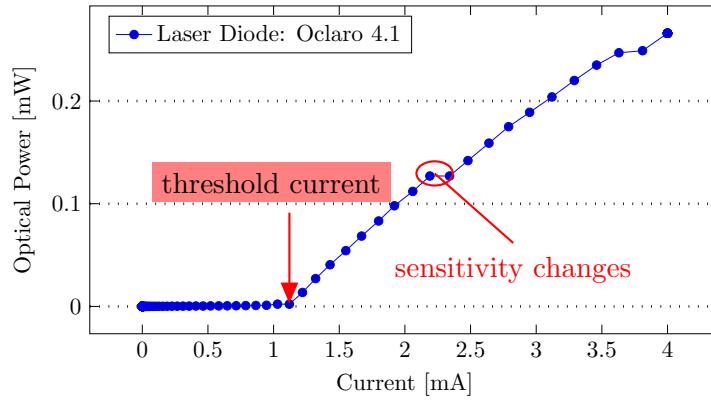
Figure 3.3.: Optical output power as a function of the laser current. Measured for a VCSEL Oclaro laser diode at a temperature of 25°C. When the threshold current is reached, the diode emitting characteristic switches from LED to laser mode and the power increases rapidity. The jumps in the linear behaviour are due to the automatic changes of the powermeter's sensitivity.

depends strongly on the diode's temperature T. A relation of $I_{th} \sim e^{\frac{T}{T_0}}$ is assumed with T_0 a characteristic value.

3.4. Frequency Dependence Amplification

In semiconducting lasers induced transitions from various energies states in the valence band E_V to multiple energy holes in the conduction band E_C take place. So photons with different wavelengths are emitted, their energies can be expressed as $h\nu = E_C - E_V$.

The bands are not equally occupied with electrons or holes, the fermi-function

$$f_i(E_i) = \frac{1}{e^{\frac{E_i - F_i}{k_B T}} + 1} \quad i = \{V, C\} \tag{3.4}$$

describes their population as a function of temperature T and the energy differences between the electron E_C or hole energy E_V and the fermi energy $F_{C,V}$ of their corresponding band, either $E_C - F_C$ or $E_V - F_V$. Therefore the transition processes are not equally likely. This leads to a frequency dependent gain $g(\nu)$. For $g > 1$ the laser operation becomes theoretical possible. It is satisfied for population inversion, $N_2 > N_1$. Considering the interaction cross-section for induced emission σ the frequency dependent gain $g(\nu)$ can be expressed.

$$g(\nu) = \sigma(N_2 - N_1) \tag{3.5}$$

In order to get a more illustrative description of the gain some assumptions, substitutions and transformation were made, these are shown in the book [16].
The gain can be expressed as

$$g(\nu) \sim \sigma(h\nu - E_g)^{1/2}(f_C - f_V)\Delta\nu. \tag{3.6}$$

$\Delta\nu$ is the frequency interval around ν and E_g the band gap energy. The laser threshold is reached when $f_C - f_V > 0$ is fulfilled. For low frequencies the function (3.6) is determined by square-term $(h\nu - E_g)^{1/2}$, at higher frequencies the exponential decay of the fermi functions dominates and the gain drops. By injecting electrons ($\hat{=}$ laser current) in the conduction band, the fermi energy F_C is raised, thus the fermi function f_C grows and so does the gain $g(\nu)$. With higher currents the maximum of the gain function shifts to higher frequencies.

3.5. Direct Modulation of Laser-Diodes

For applications, the frequency tuning is of particular importance. The laser frequency is determined by the band gap, so all energy gap-changing parameters are suitable for laser frequency tuning. In general it is not possible to tune the laser continually over the entire gain profile of the semiconductor ($\sim$10 nm). Mode jumps (from one resonator mode to the next) are unavoidable. By using an external resonator, like the external cavity laser diode (ECDL), it is possible to reduce the number of mode jumps.
The main tuning parameters are the laser temperature and the laser current. Variation of the laser current changes the emitted frequency. This is due to the current influences on the temperature which causes a change in the index of refraction n, the energy gap and a change in the resonator length L[13]. The resonator eigenmodes ν get shifted with

$$\Delta\nu = \frac{\partial\nu}{\partial n}\frac{dn}{dT}\Delta T + \frac{\partial\nu}{\partial L}\frac{dL}{dT}\Delta T = -\nu\left(\underbrace{\frac{1}{n}\frac{dn}{dT}}_{(a)} + \underbrace{\frac{1}{L}\frac{dL}{dT}}_{(b)}\right)\Delta T. \tag{3.7}$$

21

A periodic modulation of the laser current leads to amplitude modulation (AM), which becomes clear from figure 3.3. A higher laser current results to a higher laser output current. Small changes in the current result in a direct modulation of the lights amplitude. This amplitude modulation (AM) causes two of the so called side bands, see section 5.2. One has a lower frequency $\omega_c - \omega_m$, compared to the laser frequency ω_c and one has a higher frequency $\omega_c + \omega_m$. Additionally, the equation (3.7) shows, that the laser frequency is tunable by periodic variations of the laser current. Two effects, the change in index of refraction (3.7)(a) and the resonator length-variation (3.7)(b), are responsible for a frequency modulation (FM). In general the change of the index of refraction (3.7)(a) is predominal in most cases.

In practice the modulation capability of laser diodes is reduced with higher modulation frequencies. So the amplitudes of the sidebands decrease with higher modulation frequencies [40]. The maximum frequency tuning range is defined by the range between two mode jumps [34].

3.6. External Cavity Laser Diode (ECDL)

The ECDL uses an external resonator for frequency selection, in contrast to the crystal surfaces at the heterostructure design. The external resonator is mostly realised with a lens and an external grating, which reflects the light back into the active region. The grating is placed in a certain angle that the first order of the grating's diffraction pattern is send back. By adjusting the grating's angle, the laser light's emitting frequency can be selected. The large length of the external resonator leads to a small mode spacing, compared to a heterostructure laser. Two common designs are the Littrow-configuration and the Littman-configuration.

3.7. Distributed Feedback (DFB)-Laser Diode

The Distributed Feedback (DFB)-laser is an edge emitting diode. The resonator is build up like a heterostructure laser with the crystal surfaces as mirroring planes. A special longitudinal mode selection is achieved by a metal grating, which is placed on the active region. The grating periodicity G is in the range of nm and made by electron beam lithography.

The laser field interacts with the reflections on the grating and preferred frequencies get amplified by constructive interference while other frequencies are suppressed by destructive interference. This constructive interference is called *distributed feedback*. The metal grating varies the real and imaginary part of the index of refraction n with its periodicity. This influences the evanescent tail of the laser modes and this provides the distributed feedback [42].

The periodicity G and n (index of refraction of the grating) determine the laser's center frequency. In order to built a DFB-laser with a specific wavelength λ_{Bragg}, the *Bragg-Condition* has to be fulfilled

$$m\lambda_{Bragg} = 2nG \tag{3.8}$$

with m the order of diffraction.

The DFB-laser delivers the tunability of a external-cavity setup. Frequency tuning is realised with variation of the refractive index by current or temperature change.

With an index coupled DFB-laser a single mode operation with a linewidth under 200 kHz and a optical power of 2 mW is possible [26] [42].

One of the main disadvantages is the strongly elliptical beam shape. This requires a aspheric lens or a achromatic prism for collimation. The laser is very sensitive to back reflection, so an optical isolator is necessary[42].

3.8. Vertical Cavity Surface Emitting Laser (VCSEL)

The laser design of the Vertical Cavity Surface Emitting Laser (VCSEL) differs to the design of the edge-emitting lasers, which were described until now. The cavity (the resonator) is placed vertically on the chip. Its active zone is a quantum well surrounded by high reflective distributed Bragg reflectors. In a GaAlAs-diode the active zone's thickness is 8 nm.

Through its special structure, only one specific longitudinal mode operates at each time and is emitted through the surface of the chip [2].

The vertical cavity has a low parasitic capacity which results in a high frequency modulation bandwidth of several GHz by direct current modulation [37]. Its beam characteristic has a rotational symmetry and an angle of divergence between 15° and 20°. Therefore it is very suitable for fibre coupling.

The disadvantages are a high linewidth of 10 MHz and a low optical output of a few mW [2].

4. Optics

Geometrical optics is used to describe light beams and their interaction with lenses, prisms and other optical components. Light is treated as beams describing the (time averaged) direction of the energy-flux, diffraction-effects are not taken into account. This is a sufficient approximation for a lot of applications where the typical dimensions considered are much larger than the wave length λ.

The wave-like characteristics of EM-fields are not taken into account. The sections about optics and optical components are based on the books [16] and [22].

4.1. Gaussian Optics

The laser beam is formed within the active region and leaves the resonator through a semitransparent mirror. The laser beam diffracts on the edges of the resonator mirrors which constricts the laser beam within the middle of the cavity. In order to describe this, the laser beam is characterised by Gaussian-formed EM waves.

Real lasers systems are able to transmit different transversal electric field distributions, which are called modes. In the ideal case, the intensity distribution (in a plane perpendicular to the beam direction) is Gaussian shaped. This basic mode is called transverse electromagnetic mode (TEM)$_{00}$. The numbers 00 indicate that there is no zero-crossing of the electric field components in both orthogonal lateral directions, see figure 4.2. Higher modes are described by their number of zero-crossings, this is shown in figure 4.2.

The basis for all mathematical EM wave descriptions is the wave equations, which is derived from the Maxwell-equations. The equation for the electric field is:

$$\left(\frac{\partial^2}{\partial x^2} + \frac{\partial^2}{\partial y^2} + \frac{\partial^2}{\partial z^2} - \frac{1}{c^2} \frac{\partial^2}{\partial t^2} \right) \cdot E(x, y, z, t) = 0 \qquad (4.1)$$

x, y and z are the coordinates, t is the time and $c = c_0/n$ the velocity of light in a medium with the index of refraction n.

One of the solutions for (4.1) is a spherical wave. In the paraxial approximation for spherical waves the solution for the electric field is (4.2). It is only valid for areas close to the optical axis, which is a sufficient approximation for laser beams [16].

$$E(r, z, t) \approx \frac{B}{q(z)} \cdot exp\left(-\frac{r^2}{w^2(z)}\right) \cdot exp\left(-i\frac{kr^2}{2R(z)}\right) \cdot exp(i(\omega t - kz)). \qquad (4.2)$$

It describes the propagation of a TEM$_{00}$ laser beam in the z-direction. Figure 4.1 describes the change of the beam radius $w(z)$ as a function of the direction of propagation

z. $R(z)$ is the radius of curvature and describes the bending of electric field surfaces with the same phase relation with respect to the origin. The field amplitude is $B/q(z)$ with $q = z + iz_R$. The smallest radius is called beam waist $w(0) = w_0$. The characteristic distance z_R for which the beam's cross-sectional areas doubles, is called the Rayleigh-length, so $w(z_R) = \sqrt{2}w_0$. This leads to the relation:

$$w_0 = \sqrt{z_R \frac{\lambda}{\pi}} \tag{4.3}$$

For a Gaussian beam (TEM$_{00}$) 86.5% of the laser power is within the beam's radius $w(z)$, at this point the intensity drops to $1/e^2 = 13.5\%$ of the intensity maximum. The red line in figure 4.1 is drawn at that intensity.

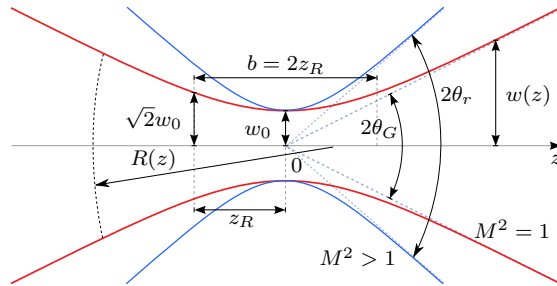The angle of divergence θ for distances $z \gg z_R$ is:

Figure 4.1.: Gaussian beam radius $w(z)$ as a function of the propagation direction z. M is the beam quality factor, which adapts ideal beams to real beams with $\theta_r = M^2 \theta_G$. $R(z)$ is the radius of curvature for the beam's wave front. For an ideal beam is $M^2 = 1$ and for a real beam $M^2 > 1$. θ_G is the angle of divergence and w_0 the beam waist for the ideal/Gaussian beam. At the Rayleigh-length z_R the beams cross-sectional area is doubled and $w(z_R) = \sqrt{2}w_0$. b is defined as the focal length. The red line marks the beam intensity at $1/e^2 = 13.5\%$.[1]

$$\theta = \lim_{z \to \infty} \frac{w(z)}{z} = \frac{w_0}{z_R} = \frac{\lambda}{\pi w_0} \tag{4.4}$$

With the expression (4.4) the angle of divergence of a laser beam can be estimated. The smaller the active zone, the smaller will be the beam waist within the active zone and so the angle of divergence is increased. This is shown in figure 3.2, in the chapter about laser diodes. Due to the flat rectangular active region, two characteristic angles of divergence are formed. The smaller width results in a larger angle. So the elliptical intensity distribution is explained.

The Gaussian beam has planes with the same phase which are shaped like a parabola.

---

[1]Image-adapted: Source: Gaussianbeam.png: en:User:DrBob ⓒ CC BY-SA 3.0
7$^{\text{th}}$ of December 2015 `https://commons.wikimedia.org/wiki/File:GaussianBeamWaist.svg`

Their radius of curvature $R(z)$ is

$$R(z) = z + \frac{z_R^2}{z}.$$ (4.5)

For large $z \gg z_R$ is $R(z) \approx z$. Therefore the beam behaves like a spherical wave. For small z and large $R(z)$ the wave front appears as a plane wave. So the Gaussian beam's characteristic is a (z-dependent) mixture of spherical and plane waves.

The TEM$_{00}$ has no zero-crossing in the transversal electric field, as mentioned above. The higher modes are also solutions of the wave equation (4.1), which are expressed mathematically as Hermitian polynomials. The Hermitian index corresponds to the number of zero-crossings. Some of these higher TEMs are shown in figure 4.2. One feature of all the TEMs is that their beams' specific shapes do not change when they propagate.
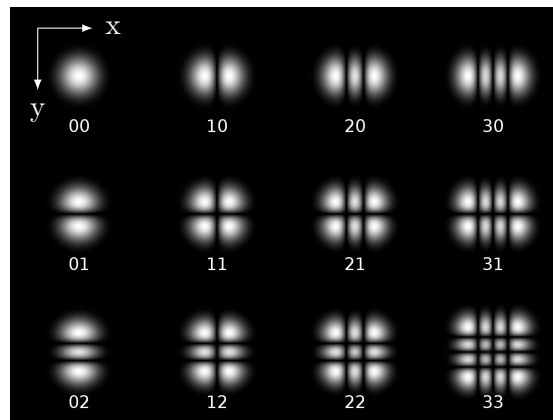
Figure 4.2.: Different Hermitian-Gaussian mode cross-sections. The numbers underneath the modes indicates the number of electric field zero-crossings. The first number is associated with the x-axes and the second with the y-axes.[2]

4.1.1. Influences of Lenses on Gaussian Beams

From geometrical optic the equation for the relations between the distance of an object g, the distance of the image b and the focal length f, is known.

$$\frac{1}{f} = \frac{1}{b} + \frac{1}{g}$$ (4.6)

These distances refer to their corresponding principal plane.

A Gaussian beam with the initial radius w_0 propagates through a lens with the focal length f. The beam's waist is in a distance of a to the lens. It is considered to be a

---

[2]Image-adapted: Source: Hermite-gaussian.png: en:User:DrBob ⓒⓒ CC BY-SA 3.0
7th of December 2015 `https://commons.wikimedia.org/wiki/File:Hermite-gaussian.png`

thin lens, so both principle planes coincide. This beam travels through the lens, there its properties change and a new Gaussian beam is formed with the new parameters w_0' at the distance of a'. From (4.6) and the properties of Gaussian beams the following equation is achieved:

$$a' = -f + \frac{f^2(f-a)}{(f-a)^2 + z_R^2} \tag{4.7}$$

$$\frac{w_0'}{w_0} = \frac{f}{\sqrt{(a-f)^2 + z_R^2}} \quad \text{with } z_R = \frac{\pi w_0^2}{\lambda} \tag{4.8}$$

The minimal w_0' (a focused beam) is reached when z_R and w_0 are large. For $z_R \gg a - f$ the focal "point" becomes

$$w_0' = \frac{\lambda f}{\pi w_0}. \tag{4.9}$$

Within this spot w_0' 86.5% of the lights intensity is located. In practise the beam's smallest radius w_0 is limited by the diameter D of the used lens. The radius has to be $w_0 \leqslant D/2$ so that it becomes not cut by the lenses aperture. w_0' becomes

$$w_0' \geqslant \frac{2f\lambda}{\pi D}. \tag{4.10}$$

For the narrowest Gaussian beam, it is necessary to enlarge D.
In optics it is convenient to define the numerical aperture (NA) as

$$NA = n \cdot sin(\theta). \tag{4.11}$$

n is the index of refraction and θ the angle of divergence. For lenses the NA is

$$NA = \frac{D}{2f}. \tag{4.12}$$

It describes a lens' ability to collect light, the higher NA is, the more light is collected. The NA is used in lens applications were a small object or small light source is placed very close to a lens and as much light as possible should pass through.
The equation (4.10) for the focused beam waist can be expressed as a function of NA

$$w_0' \geqslant \frac{\lambda}{\pi NA}. \tag{4.13}$$

The NA is used to design combinations of lenses. Two lenses are compatible, if the second one (seen from the direction of propagation) has an higher NA.

4.1.2. Real Gaussian Beams

Ideally a laser emits a TEM_{00} mode. In reality much more complex structures as those of figure 4.2 are detected. This complex structures are formed by the combination of higher laser modes with amplitude and phase fluctuations.

For large distances, the expression (4.4) is still a good approximation for the angle of divergence. For real beam, the initial beam's waist w_0 and the initial angle of divergence θ_{Gauss} is enlarged, so the factor M is introduced, the beam quality factor. This leads to the real beams angle of divergence θ_{real}:

$$\theta_{real} = M^2 \theta_{Gauss} = M^2 \frac{\lambda}{w_0 \pi} \tag{4.14}$$

In figure 4.1 a TEM$_{00}$ with $M^2 = 1$ and a more realistic Gaussian beam with $M^2 > 1$ is shown.

4.1.3. Lenses for Laser Applications

In the previous section the large angles of divergences of laser diodes are described. Therefore a lens is necessary to focus or collimate the laser beam. A high NA is wanted to collect as much light as possible and to reduce diffraction on the aperture of the lens. A low spherical aberration enables a defined focal spot. This is achieved by aspheric lenses designed for specific applications.

A widely used lens type is the so called *Bestform lens*. One side of the lens features an infinite object distance while the other side has a defined focal length. This (virtually) eliminates the spherical aberration in the case of a collimation-application and thus a diffraction limited focus spot size can be achieved [7].

In lasers with two different angles of divergence (like a DFB-laser) a cylindrical lens or a pair of compensation-prisms (anamorphic prism-pairs) are used for optimal beam shaping.

So it is possible to compensate angle deviations, where one angle is between 4° and 40° while the other is much greater in the range of 40° to 80°.

4.1.4. Fibre and Fibre Couplers

In order to transport laser light, optical fibres are used. Fibres which transmit multiple optical modes are called multi-mode fibre (MMF). Fibres which only allow one mode to be transmitted, are called single-mode fibre (SMF).

For the visible and near IR spectrum the fibres are made out of cylindrical shaped quartz (SiO$_2$) glass core ($n_1 =$1.47). The diameter is between 3 and 1000 μm. The core is covered with a different SiO$_2$ layer (cladding) which provides total internal reflation due to its smaller reflective index ($n_2 =$1.46). Due to this jump in the refractive index, this fibres are called step-index fibres. The incident light beams are reflected at the border between the two different refractive indices. Depending on its initial angle of entrance the beams are reflected different times. This leads to interference effects and causes a restriction to certain optical modes (TEMs) within the fibre.

The laser light is brought with a lens into the fibre. Provided that the focused beam's diameter is a little smaller then the fibre's one. The maximal allowed beam divergence θ_{max} is defined by the NA of the fibre with:

$$NA = sin(\theta_{max}) = \sqrt{n_1^2 - n_2^2} \tag{4.15}$$

Due to its high NA, it is relatively easy to couple light into its guiding regime and so they can carry high laser intensities. However this multi-mode fibre (MMF) leads to a high modal dispersion of signals. Additionally the intensity-pattern, which is observed after the light had passed the MMF, changes when the fibres are bent differently. For different modes the optical path through the fibre depends on the reflection angle and this is changed when the fibres are bent. For some applications it is necessary to
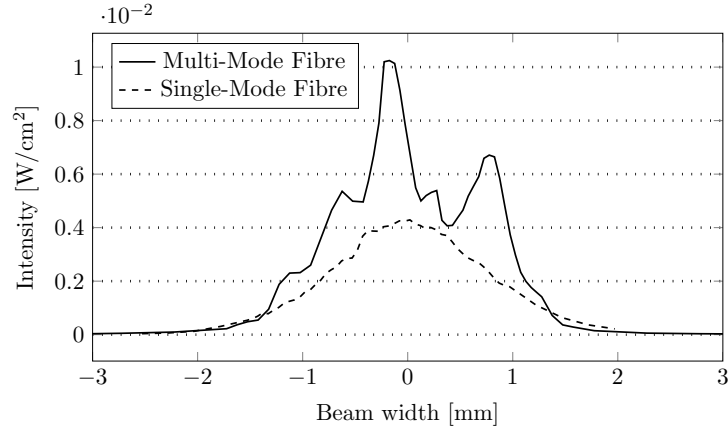

Figure 4.3.: Beam profile intensity of a MMF and a SMF as a function of the spacial dimension. The SMF's beam is Gaussian shaped and the shape stays constant when the fibre is bend differently. The MMF in contrast shows a superposition of different modes which change with the bending of the fibre. The measurements where performed with the VCSEL Oclaro 2.1. The intensity distribution was detected with the slit-method (slit width: 16 μm, see section 8.2.5).

have a fibre with low dispersion and signal delay. This is achieved by so called gradual-index or graded-index fibre. Here the change of n is not an abruptly jump, but rather a smooth transition from n_2 to n_1 resulting in a parabola-shaped index-profile in the most common case. This leads to a balancing of the signal dispersions and so the mode's features are mostly preserved. But just the low index modes can be carried.

In order to carry just a single mode the core diameter has to be reduced to a few μm to guide just the TEM_{00}. Higher modes are above the so called cut-off wavelength $\lambda_{cut-off}$ given by wave guide theory considerations. So single-mode fibre (SMF) are used as a optical mode filter where only the ground mode passes. They are used for applications where a high quality beam is required. For example a SMF produces a single collinear laser beam when two beams are coupled into the fibre.

In figure 4.3 a laser beam's intensity distribution for a single and a multi-mode fibre is shown.

4.2. Optical Components

In order to perform optical measurements, several optical components are necessary to manipulate light beams. For the parts, which are used in the experiments of chapter 6, a short description of their functionality is listed below.

4.2.1. Faraday Isolator

The Faraday effect describes the rotation of the linear polarisation of the EM-field due to an applied homogeneous magnetic field in a medium. The angle δ is dependent on the length of the medium l, V the material specific Verdet constant and the magnetic flux density B [16].

$$\delta = l \cdot V \cdot B \tag{4.16}$$

This effect can be used to eliminate optical feedback into the laser diode. Therefore a polariser is placed before the Faraday rotator. Behind this a second polariser is placed, which polarisation orientation is rotated at $45°$ in respect to the first polariser. The Faraday rotator turns the linear polarisation of the incident pre-polarised beam by an angle of $45°$. So the entire intensity can pass the second polariser. If a beam comes from the opposite direction, it becomes polarised by the second filter first, than gets shifted at $45°$ in the other direction by the Faraday rotator. So the reverse beam hits the first polariser at $90°$ and no intensity can pass. This is used as an "optical isolator" and prevents unwanted back reflections.

4.2.2. Polarizing Beam Splitter Cubes

A polarizing beam-splitter cube is as polariser. Here two $90°$ flint glass prisms are glued together in order to form a cube. 95% of the incidents light, which is polarized parallel to the light's plane is incident, is transmitted. Only 0.1% of the perpendicular polarised light is transmitted, the rest is reflected in the dielectric layer in between the cubes. Extinction ratios of $1:10^4$ are achieved. [36]

4.2.3. Dichroic Glass Polariser

Dichroic polarisers are used to generate linear polarised light. Dichroic means that one polarisation axis is absorbed much stronger than the other one. This is either done by dichroic crystals or by certain kinds of polarising sheets. In the ideal case 50% of the non polarised light is transmitted. Extinction rates as high as 10^5 can be achieved. For the IR-spectral range the polariser is made out of metal whiskers, which are deposited from the metal vapour on a substrate [16][51].

4.2.4. $\lambda/4$ and $\lambda/2$ Plates

For some measurements circular polarized light is needed. Mostly a $\lambda/4$ plate is used to switch from a linear polarised beam to a circular. The plate is made out of quartz glass and its crystal axis is placed in an $45°$ angle to the incident polarisation vector. The

linear polarised beam is projected in equal parts to the slow and the fast propagation axis, which are characterised by different refraction indices. Both beams experience a phase shift. By a proper choice of the plate's thickness ($\lambda/4$) the beam's interference only allows circular polarisation to leave the quartz plate.

If the thickness is $\lambda/2$, the plate can be used to rotate the polarisation at an angle 2α by rotating the plate at the angle α. All this functionality is only fully available if the light's wavelength matches the plate's half or quarter thickness.

4.2.5. Glan-Thompson Prism

The Glan-Thompson prism is used to produce a polarised beam from a non polarised one without changing the direction of the initial beam. It is made of two prisms (two birefringent crystals) with a small gap of air in between. The angle between the optical axis and the gap between the prisms is chosen to reflect the ordinary beam, so that it is no longer propagating in the optical axis, and to transmit the extraordinary beams unhindered. If a glue is choosen instead of air, high laser intensities would lead to degradation of the used material. The Glan-Thompson prism can be used as variable intensity reducer when it is mounted turnable with respect to the laser source's polarization.

4.2.6. S+K Optical Mounting and Connection System

The company Schäfter+Kirchhoff GmbH (S+K) offers the modular construction kit *multicube.* It is designed for stable mounting of optical components and enables a high flexibility. The components are easily exchangeable, therefore a flange and adapter system is used, based on a 19.5 mm diameter with M3 fixing screws.

A lot of these modules are used in the laboratories of the Institute of Experimental Physics at the TU Graz. So it is convenient to adopt the measures of the S+K-*multicube* system and use them in own designs. This was done for the construction of the LCC and DFB- housing, see 6.3 and 7.2 [3]

---

[3]S+K-MultiCube System: 26th of November 2015
http://www.sukhamburg.com/produkte/multicube.html

5. Electronics

5.1. High Frequency Technology

The book *Halbleiter-Schaltungstechnik* by U. Tietze and C. Schenk [45] provides fundamentals concerning communication engineering and their circuits. These basics are used to arrange the following sections.

5.1.1. Coaxial Cable

Coaxial cables are widely used in technological applications. This cable is build up by cylindrical shaped conductors with different diameters. The larger one wraps in smaller one. The so formed spacing in between the conductors is filled with an dielectric material. Due to its arrangement the cable is shielded because the electric and the magnetic fields are kept in between both conductors. The most common dielectric materials are Teflon ($\epsilon_R = 2.05$) and polystyrene ($\epsilon_R = 2.5$).

Impedance

The ratio of electric field strength E and magnetic field strength H is called impedance Z and describes the cable's resistance to a propagating electro-magnetic wave.

$$Z = \frac{|E|}{|H|} = \sqrt{\frac{\mu_0 \mu_r}{\epsilon_0 \epsilon_r}} \overset{\mu_r = 1}{=} \frac{377}{\sqrt{\epsilon_r}} \quad [\Omega] \tag{5.1}$$

It is convenient to set $\mu_r = 1$ because there are no magnetic materials in between the conductors.
To calculate the impedance of a coaxial wire Z_W, the cables geometry must be taken into account. Therefore a geometry factor k_G is added to the equation (5.1).

$$Z_W = Z \cdot k_G = Z_F \frac{1}{2\pi} ln\left(\frac{d_a}{d_i}\right) = \frac{60}{\sqrt{\epsilon_r}} ln\left(\frac{d_a}{d_i}\right) [\Omega] \tag{5.2}$$

d_a is the outer conductor's diameter and d_i the inner conductor's diameter.
Every cable and each other electrical load have their own impedances. When two objects with different impedances are connected, an impedance transformation occurs. On the jump between different impedances reflections of the EM-waves take place which results in losses. So the impedance matching is very important for high frequency (HF)-applications.

5.2. Frequency Modulation

The method of frequency modulation is widely used in traditional wireless data transmission applications [45].
A high frequency carrier wave $\vec{E}(t) = \vec{E}_0 \cdot s_C$ is modulated with a baseband signal $s(t)$ by varying the parameters amplitude, frequency and phase. From these parameters the different names are given:

- amplitude modulation (AM):

$$s_C(t) = (a_C + k_{AM}s(t)) \cdot cos(\omega_C t) \tag{5.3}$$

- frequency modulation (FM):

$$s_C(t) = a_C \cdot cos\left(\omega_C t + k_{FM}\int_0^\tau s(\tau)d\tau\right) \tag{5.4}$$

- phase modulation (PM):

$$s_C(t) = a_C \cdot cos\left(\omega_C t + k_{PM}s(t)\right) \tag{5.5}$$

The coefficients k_{AM},k_{FM} and k_{PM} indicate the strength of the modulations. a_C is the amplitude of the carrier and ω_C the carrier's frequency.
For the FM the instantaneous frequency $\omega(t)$ is modulated with the baseband signal $s(t)$.

$$\omega(t) = \omega_C + k_{FM} \cdot s(t) \tag{5.6}$$

The instantaneous phase ϕ is related with instantaneous frequency via $\omega(t) = d\phi/dt$. Therefore equation (5.6) has to be integrated to get $\phi(t)$. The phase ϕ at the time t depends on the previous phase behaviour of ω. By substituting $\phi(t)$ in $s_C = a_T \cdot cos(\phi(t))$ the equation

$$s_C = a_T \cdot cos\left(\int_0^t \omega(\tau)d\tau\right) = a_C \cdot cos\left(\omega_C t + k_{FM}\int_0^\tau s(\tau)d\tau\right) \tag{5.7}$$

is achieved. A sinusoidal baseband signal $s(t) = a_s cos(\omega_s t)$ produces the carrier signal

$$s_C = a_C \cdot cos\left(\omega_C t + \frac{k_{FM}a_s}{\omega_s}sin(\omega_s t)\right). \tag{5.8}$$

The maximal variation of the carrier frequency $\omega_C \pm k_{FM}a_s$ is called frequency deviation $\Delta\omega$. The relation $\eta = \Delta\omega/\omega_s$ is defined as modulation index.
For a sinusoidal baseband signal, the carrier signal (5.8) can be expressed as expansion of *Bessel functions of the first kind* $J_n(\eta)$. In figure 5.1 a FM spectrum is shown. The Bessel functions define the amplitudes of the side bands.
In principle, there is an unlimited number of side bands. But just a small number of peaks is visible in a spectrum. The higher the modulation index, the more bands become visible. In the spectrum are side bands left (lower) and right (upper) of the carrier frequency, their distance to each other is the baseband signal frequency ω_s.
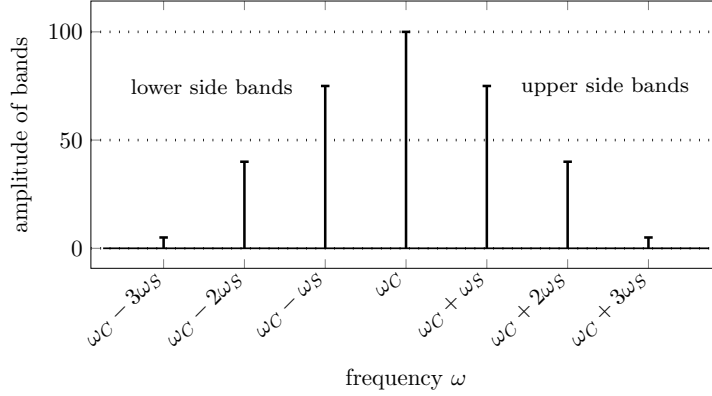
Figure 5.1.: Schematic representation of the spectrum of the carrier ω_C which is frequency modulated by the the signal ω_S. The low modulation index $\eta < 1$ results in a low number of visible upper and lower side bands. The picture was adapted from [45]

5.3. Electronic Devices

The following section describes two measurement instruments which were used for the CPT-resonance experiments in section 6.

5.3.1. Lock-In Amplifier: SR830

Lock-In amplifiers are used to detect very small AC signals which are normally covered by noise [31].
Its working principle is based on the comparison of a sinusoidal reference signal

$$s_r(t) = V_r \cdot sin(\omega_r t + \theta_r) \tag{5.9}$$

with the initial reference signal disturbed by the measurement

$$s_m(t) = V_m \cdot sin(\omega_r t + \theta_m). \tag{5.10}$$

In general, the amplitude V_m, which is changed by the experimental object, is of interest. θ_m is the phase shift introduced by the measurement.
An internal oscillator generates a lock-in signal $s_{int} = V_{int}\dot{s}in(\omega_{int}t + \theta_{int})$. In order to get V_m the signals s_{int} and s_m are multiplied by a phase sensitive detector (PSD).

$$V_{PSD} = V_m V_{int} sin(\omega_r t + \theta_m) sin(\omega_{int}t + \theta_{int})$$

$$= \frac{1}{2}V_m V_{int} \underbrace{cos([\omega_r - \omega_{int}] + \theta_m - \theta_{int})}_{\text{slow oscillating}} - \frac{1}{2}V_m V_{int} \underbrace{cos([\omega_r + \omega_{int}] + \theta_m + \theta_{int})}_{\text{fast oscillating}} \tag{5.11}$$

This signal consists of slow and a fast oscillating part. By connecting the PSD to a low pass filter, the higher frequency oscillation gets removed from the AC signal.

In an ideal case the difference signal $\omega_r - \omega_{int}$ in the argument of the *cos*-function can be tuned to be zero by changing the frequency of the internal oscillator, so (5.11) becomes

$$V_{PSD} = \frac{1}{2} V_m V_{int} cos(\theta_m - \theta_{int}). \qquad (5.12)$$

This signal is only depended on the phase relation between the disturbed signal and the internal oscillator. Now all AC-components are removed.

All frequencies, which are not close to ω_r do not contribute to V_{PSD}, so just noise signals in a very small bandwidth close to the reference frequency are detected. V_{PSD} becomes a DC signal which is now proportional to V_m if the phase relation is kept constant. Therefore θ_{int} is phase looked to θ_r with an active phase-looked-loop. By using the internal oscillator as a reference signal, the difference frequency $\omega_r - \omega_{int}$ is inherently zero and the phase-lock condition is automatically fulfilled.

In order to measure the V_m signal the phase θ_{int} has to be adjusted to reduce the phase difference $\theta_m - \theta_{int}$ to zero, so that $V_{PSD} = \frac{1}{2} V_m \cdot V_{int}$. In an experiment, the phase θ_m is not constant, so a permanent tuning of θ_{int} is necessary. To prevent this a second PSD is added, with a 90°-shifted phase in respect the reference signal. After the second PSD and a second low pass filter the signal

$$V_{PSD} = \frac{1}{2} V_m V_{int} sin(\theta_m - \theta_{int}) \qquad (5.13)$$

is detected. The first PSD is label as $X = V_m cos(\theta)$ and is called "inphase" component. The second signal is $Y = V_m sin(\theta)$ and is called "quadrature" component. The X and Y components are shown on the lock-in amplifier's display. The full signal can be reconstructed without the phase dependence:

$$\sqrt{X^2 + Y^2} = V_m \qquad (5.14)$$

Such a dual-phase lock-in amplifier is commonly used.

The Lock-In Amplifier *Stanford Research Systems Model SR830* [31] was used to perform the measurements for this thesis. This device is remote controllable via the GPIB-bus. This feature was used for a LabView-automation for measuring CPT-resonances, see section 6.2.

The following list describes the configurable parameters, which were externally set by the program.

- **Reference Frequency**
  The reference frequency $\nu_{int} = \omega_{int}/2\pi$ of the internal reference oscillator.

- **Reference Amplitude**
  The reference amplitude of the internal reference oscillator.

- **Reference Phase**
  The reference phase shift of reference oscillator in respect to the output signal.

- **Time Constant**
  The time constant configures the low pass filter with $\frac{1}{2}\pi f$. f is the -3 dB frequency of the filter. The higher the time constant the more steady and reliable the result will be. So more noise is filtered. But this results in problems when real signal changes occur. The devices becomes less sensitive.

- **Low Pass Filter Slope**
  The filter slope determines the roll off of the low pass filter. The settings 6,12,18 and 24 dB per octave are available. A higher roll of is used for low reference frequencies.

- **Sensitivity**
  The sensitivity ranges from 2 nV/fA to 1 V/µA and is divided in 26 individual sensitivity steps.

- **Reserve Mode**
  The reserve mode is used to handle the specific amplifications within the device to deal with high signal noises.

- **Notch Filter**
  This setting removes influences from the line frequencies at 50 Hz and 100 Hz.

5.3.2. Signal Generator: SMR20

The full synthesised microwave generator *SMR 20*[30] from the company *Rohde & Schwarz* was used to perform all GHz-experiments. This device produces GHz signals up to 10 GHz with a step resolution of 0.1 Hz. Additional it is possible to modulate a GHz carrier with an external modulation signal either with AM or with FM. For the setup in section 6 only the FM is used. In the experiment, the following parameters were set:

- **Power**
  Output power in dBm. 0 dBm correspondents to 1 mW at 50 Ω load impedance.

- **Deviation**
  Sets the deviation of the FM.

- **External Reference**
  An Rb optical pumped hyperfine atomic clock[1] at 10 MHz is used for GHz frequency stabilisation.

- **Sweep-Parameter**
  A sweeping mode allows an automatic or external triggered sweeping of the GHz frequency. Therefore a start, end and step frequency has to be set.

---

[1] *Stanford-Research Systems: Model FS725 Rubidium Frequency Standard*

6. Improvements of a CPT-Resonance Setup

6.1. Frequency-Modulation Spectroscopy

For detecting very narrow spectral features frequency modulation (FM) spectroscopy is used [8]. The key concept is to use the side bands of FM-modulated laser light to perform spectroscopy. The laser light's frequency acts as the carrier with ω_C. The side bands are produced by a sinusoidal signal with the frequency ω_m. This is done by direct laser current modulation, see section 3.5. The modulation index is low. The so generated pure optical spectrum is dominated by the strong carrier with one upper and one lower weak side band. The laser light is send through the sample (e.g. glass cell with specimen). On the following photo-detector the lower frequency component ω_m is detected. Narrow spectral features, like CPT-resonances can be scanned by varying ω_C or ω_m.

The scanning with ω_C is shown in figure 6.1. The isolated upper side band is tuned through the feature in the frequency picture. By monitoring the disturbance of the FM spectrum the absorption and dispersion can be observed.

Ideal spectral features are Lorentzian shaped. A theoretical derivation for probing a Lorentzian feature is shown in [8]. It is shown, that the intensity which gets detected on the photodiode can be expressed as

$$I(t) = \frac{cE_0^2}{8\pi} e^{-2\delta_0} \cdot \left[1 + \underbrace{(\delta_{-1} - \delta_{+1})\eta cos(\omega_m t)}_{\text{absorption}} + \underbrace{(\phi_{+1} + \phi_{-1} - 2\phi_0)\eta sin(\omega_m t)}_{\text{dispersion}} \right] . \quad (6.1)$$

With E_0 the initial amplitude of the laser's electric field. η is the modulation index. The subscripts $X_{-1,0,+1}$ indicate the first lower side band (-1), the carrier (0) and the upper first side band (+1). δ_i is the i-band's amplitude damping constant due to the absorption within the sample. ϕ_i is the optical phase shift, which is caused by interaction with the sample's feature.

All information about the optical feature is detectable at the modulation frequency ω_m. The $cos(\omega_m t)$ components are proportional to the difference in absorption of the two side bands. Each side band produces a beat signal with a phase shift of 180° to each other. In the case of the same amplitudes $\delta_{-1} = \delta_{+1}$ the single beat signals chancel each other by interference. So no absorption signal is observed on the photodiode. This is also true for the carrier scanning of the spectral feature[1]. The absorption amplitudes

---

[1] the feature is assumed to be symmetrical

of the side bands are equal and so both side band beat signals chancel each other. The beat signal phase shift of 180° also causes the mirrored absorption peaks in the measurements, see figure 6.2.

The $sin(\omega_m t)$ component arises when the phase relations between the side bands and the carrier change. It indicates the dispersion of the spectral feature. When the carrier scans the symmetrical spectral feature both side bands experience the same amount of phase shift but with different signs. Therefore the dispersive signal crosses the frequency axis. This zero-crossing occurs exactly at the resonance frequency and so it is useful for precise resonance tracking and frequency locking application.

Small changes in the amplitudes or the phase of a single side band result in the deviation of the perfect beat signal cancellation [28] [8].

If ω_m is larger than the linewidth of the spectral feature, like in figure 6.1, the upper side band can probe the feature independently. There will not be an influence on the lower side band and the carrier signal, other than normal noise. Therefore (6.1) is reduced to an equation were the *cos* component is directly proportional to the absorption of the single scanning side band. The *sin* is directly proportional to the dispersion which the scanning band experiences. So the spectral feature can be scanned directly. This method is highly sensitive to small changes in the scanning side band's absorption and phase. In most scanning applications, a symmetrical spectral feature can be
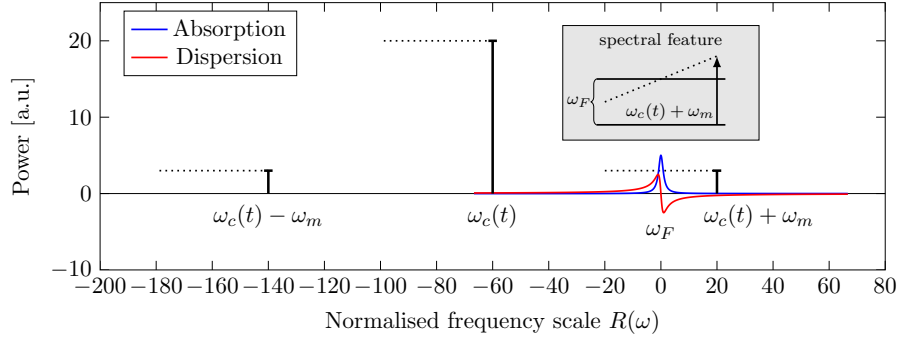

Figure 6.1.: The upper side band of the FM-modulation spectrum is tuned through the spectral feature by carrier sweep $\omega_c(t)$. In this case a 1-photon absorption process with the energy splitting ω_F, see gray box. The modulation frequency ω_m stays constant during the sweep. The frequencies $R(\omega)$ are multiples of the half feature-linewidth.

approximated as an Lorentzian function. Therefore the spectral feature's influence on the FM signal is characterised by the attenuation $\delta(\omega)$ and the phase shift $\phi(\omega)$. The normalised frequency scale

$$R(\omega) = \frac{\omega - \Omega}{\Delta\Omega/2} \tag{6.2}$$

is introduced with its line center frequency Ω and $\Delta\Omega$ the full width at half maximum (FWHM) frequency for the peak attenuation δ_{peak}. $R(\omega)$ describes the ratio between

the band's frequency distance from the center frequency of the Lorentzian function and half of the feature's linewidth. So this $R(\omega)$ is a multiple of half the linewidth. With this

$$\delta(\omega) = \delta_{peak}\left(\frac{1}{R^2(\omega)+1}\right) \tag{6.3}$$

and

$$\phi(\omega) = \delta_{peak}\left(\frac{R(\omega)}{R^2(\omega)+1}\right) \tag{6.4}$$

can be approximated [8].

The scanning of an optical feature with the upper side band, the carrier and the lower side band is shown in figure 6.2. From the equations (6.4) and (6.2) the linewidth (FWHM) of the optical feature can be identified as the distance from the maximum to the minimum of the dispersive signal. This is used in experiments to determine the feature's linewidth.

The equations (6.3) and (6.4) are used to plot the blue absorption signal $\delta(\omega)$ and the red dispersive signal $\phi(\omega)$ in figure 6.1. Here $\omega_m \gg \Delta\omega$ guaranties that each band probes the feature separately while the others are only influenced by background noise. When $R = 0$, the carrier is resonant with the spectral feature.

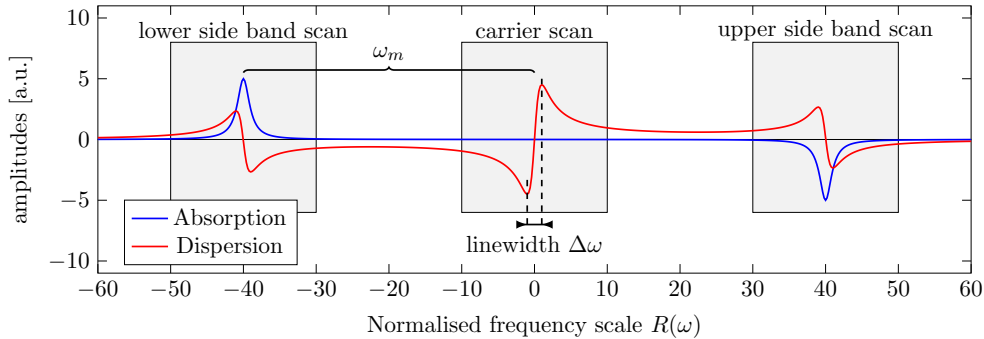For experiments it is convenient to scan the carrier frequency with a constant modulation frequency.

Figure 6.2.: Schematic absorptive and dispersive signal for a spectral feature. It is scanned with the lower side band, the carrier and the upper side band. The signals are approximated with the equations (6.3) and (6.4). The absorptive signal contains no absorption peak for the carrier. The normalised frequency axis is set to zero where the carrier scans the feature. The modulation frequency is large compared to the spectral line width $\omega_m \gg \Delta\omega$.

6.1.1. CPT-Spectroscopy in Rubidium with a Double-Frequency Modulated Laser Light

For the observation of the CPT-resonances, in the simplest case, three energy levels have to be coupled by two coherent, quasi-resonant laser light frequencies. Therefore a frequency modulated laser can be used to generate the two coherent electromagnetic fields, which are necessary for the establishment of the Λ-system excitation scheme. This approach simplifies the experimental work of coupling two laser light sources coherently [28]. Additionally it enables the design of a simple and portable spectroscopy setup for the CDSM. For performing FM spectroscopy a second modulation with ν_{kHz} is used, see figure 6.3.

In ^{87}Rb, the hyperfine ground state splitting between 5 ^{2}S$_{1/2}$ $F = 1$ and $F = 2$ is 6.8347 GHz, see section 2.4.1. For the excitation to the first excited state (5 ^{2}P$_{1/2}$) a light's wavelength of 794.978 nm is needed. The hyperfine splitting of the first excited state is 816.66 MHz (section 2.4.1). An energy-scheme is shown in figure 6.4.
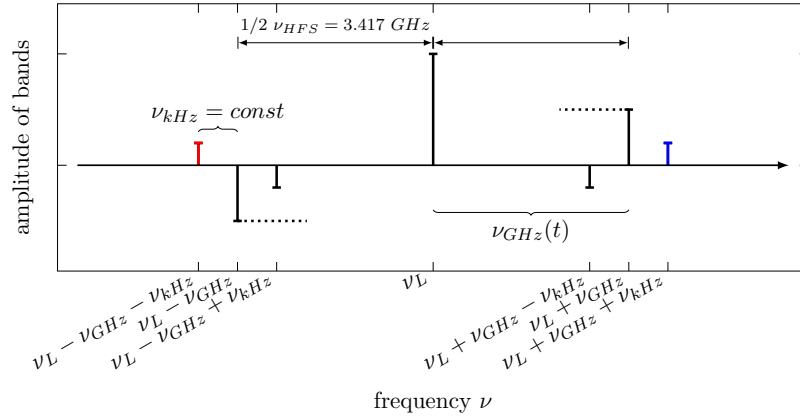

Figure 6.3.: The frequency spectrum of a double-frequency modulated laser light. The upper ($\nu_L + \nu_{GHZ}$) and the lower side band ($\nu_L - \nu_{GHZ}$) are used to establish a Λ-system within the ^{87}Rb ($\nu_{GHz} \,\widehat{=}\, 1/2\nu_{HFS}$), a energy schema is shown in 6.4. A second FM with ν_{kHz} is superimposed onto the ν_{GHz} source (see figure 6.6) producing side bands where ν_{GHz} is acting as a carrier. By changing ν_{GHz} and keeping ν_{kHz} constant, FM-spectroscopic detection is possible, as shown in figure 6.4. The red side band probes the lower frequency transition, while the blue side band probes the higher frequency transition. Some bars are mirrored due to a phase shift of 180° between the upper and the lower side band of a FM.

The direct laser current modulation by a microwave GHz signal, which is used for the diode laser's FM (see 3.5), creates an upper and a lower spectral component ($\nu_L \pm \nu_{GHz}$). The frequency distance from the carrier to each of the side bands in the context of the CDSM is 3.417 GHz. So the upper side band's frequency excites the transition from the ground state 5 ^{2}S$_{1/2}$ $F = 1$ to the first excited state 5 ^{2}P$_{1/2}$ $F = 1, 2$ and the lower band

fits the transition from ground state $5\ ^2S_{1/2}\ F = 2$ to the first excited state $5\ ^2P_{1/2}$ $F = 1, 2$ [38].

For the experiment one of the transitions to $5\ ^2P_{1/2}\ F = 1$ or $5\ ^2P_{1/2}\ F = 2$ has to be matched for achieving sufficient CPT-resonance strengths. A two photon detuning $\Delta\nu$ (see figure 6.4) in the order of $\nu_{Doppler} \approx 500$ MHz reduces the pumping rate into the dark state because of the fact, that only far detuned velocity groups of the free moving ^{87}Rb-vapour atoms become sufficient excited by the spectral distribution of the laser radiation.

As mentioned above, in order to perform FM-spectroscopy (see section 6.1 and 6.4) the microwave signal is modulated itself by a modulation frequency ν_{kHz} in the range of several kHz. The selection criteria for the ν_{kHz} frequency is guided by the facts that a single side band has to scan the feature and that the 3dB cut-off frequency of the used photo diode set a maximal frequency.

The entire light's spectrum with all produced side bands is shown in figure 6.3. The mirrored arrows indicate a phase shift of 180°. By tuning the GHz-signal both GHz side
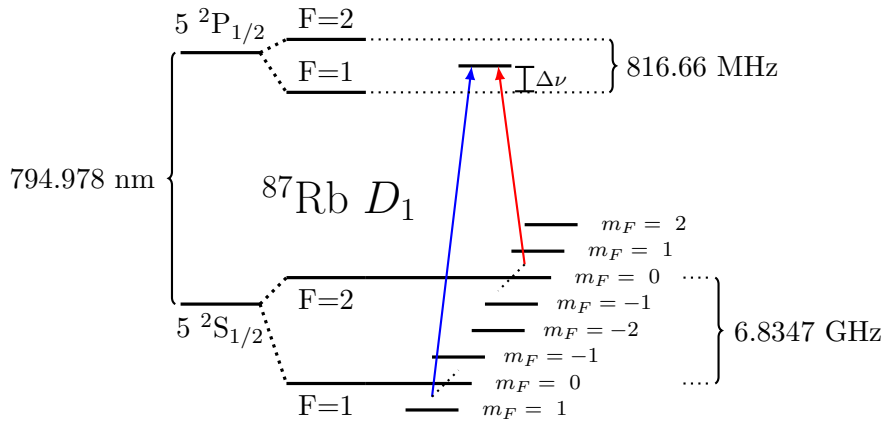

Figure 6.4.: Energy schema of the ^{87}Rb D_1. A Λ-system is achieved by two coherent EM-waves, which were produced by a double-frequency modulated laser light. Its spectrum is shown in figure 6.3. The - in that figure red marked side band - probes the in this figure red marked transition, while the blue marked side band, probes the here blue marked transition. The ν_{GHz}-scanning in this picture indicated by the dotted lines, just the 0-0-resonance is probed. A further ν_{GHz} increase would lead to the scanning of the magnetic field dependent sublevels.

bands $(\nu_L \pm \nu_{GHz})$ are shifted at the same time by the same amount but in different directions. While their distance ν_{kHz} to their own side bands is kept constant. This ensures that both transitions of the Λ-system get probed at the same time.

By applying a magnetic field, the hyperfine structure levels in figure 6.4 split due to the *Zeeman* effect, according to $2F + 1$ in either three levels $(F = 1)$ or five levels $(F = 2)$. Between this magnetic sublevels Λ-systems are established, when the side band frequencies $\nu_L \pm \nu_{GHz}$ match the ^{87}Rb excitation frequencies.

6.1. Frequency-Modulation Spectroscopy

This splitting can be tracked by the shift of the CPT-resonance frequencies. With circular polarised light Λ-systems between different states of different magnetic quantum number m_F can be established.

In the case of a weak applied magnetic field, the *Zeeman* splitting of the energy levels is smaller than the linewidth of a single CPT-resonance, thus all of the Λ-systems within this frequency range are excited. This leads to an overlap of several the CPT-resonance signals and in consequence a not fully lifted degeneracy at the CPT-resonances is detected.

In order to prevent this degeneracy a magnetic field is applied in experiments. This magnetic field must be large enough to avoid the overlap of the Λ-systems.

In experiments, the 0-0-CPT-resonance[2] is often investigated. The numbers 0-0 indicate the magnetic quantum number $m_F = 0$ of both two ground states ($F = 1$ and ($F = 2$)). This 0-0-resonance *Zeeman* frequency shift is quadratically depended on the magnetic field (see equation 2.38) and for small magnetic fields "virtually no frequency shift is detectable" [28]. So this resonance can be used for the characterisation of different cells (see section 8) and as a frequency reference in the CDSM for the correction of the GHz reference oscillators drift without a B-field induced shift of the resonance position [37].

In figure 6.5 the absorptive signal and the dispersive signal components of a 0-0-CPT-resonance are shown. An magnetic field is applied in the direction of the light to isolate the 0-0-resonance. The peaks are produced by the scanning of ν_{GHz} across the CPT-resonance position with the upper side band, the carrier and the lower side band, compare with figure 6.2. Figure 6.5 shows the for the CPT-analysis important pa-
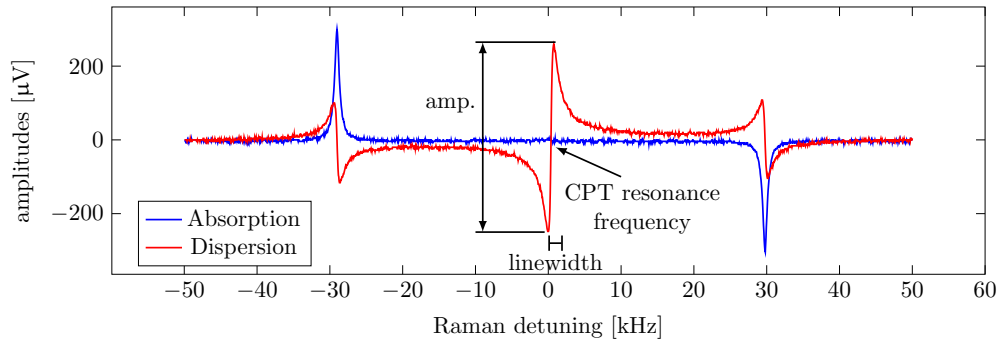

Figure 6.5.: FM-spectrum with the absorptive and dispersive signal components of a ^{87}Rb 0-0-CPT-resonance, produced by a linear ν_{GHz} sweep. The for the CPT-analysis important parameters are marked: The amplitude, linewidth and the exact CPT-resonance frequency. Experimental parameters: ^{87}Rb-buffer gas cell with 40 Torr Ne pressure, $\nu_{khz} = 30$ kHz, cell temperature 23°C, optical power 104 µW. [17]

rameters. The CPT-resonance frequency is the zero-crossing of the dispersive signal component where the carrier probes the CPT-resonance, compare with figure 6.2. The amplitude is the distances from the dispersive signal's maximal height to its minimal

---

[2]The 0-0-CPT-resonance or 0-0-transition is often called, in the literature, atomic clock transition

hight. The linewidth is given as the frequency distance from the maximum to the minimum.

For a precise measurement of the CPT-resonance frequency in the CDSM a high amplitude to linewidth ratio is desired. This can be estimated by a linear approximation of the dispersive signal's slope at the resonance frequency. The steeper the sloop, the sooner is the CDSM's electronics able to track a resonance change. This increased the devices accuracy.

6.1.2. CPT-Spectroscopy with a VCSEL-Diode

The setup for a CPT-resonance characterisation is shown in figure 6.6. The used abbreviations are described in table 6.1. This setup consists of three segments, the Laser-Cell-Heating segment, the 1-photon spectroscopy segment **A** and the CPT-resonance spectroscopy segment **B**. In order to characterise a CPT-resonance all three segments are needed.

Table 6.1.: List of abbreviations for the devices and elements used in the VCSEL CPT-resonance spectroscopy setup, which is shown in figure 6.6.

Acronym	Name	Description
LD	VCSEL-Diode	*Oclaro 795 nm Single mode* in a custom housing [1]
TC	Temperature Control	*VCSEL-Temp. Control*
CC	Current Control	*Laser Driver LC-VC-1K*
FI	Faraday Isolator	*Linos FI-790 TV*
GT	Glan-Thompson Prism	*B. Halle PGT 1.08*
$\lambda/4$	$\lambda/4$ Plate	*B. Halle* 795 nm low
	Rb-Cell	*Photonics Technologies* isotopically pure ^{87}Rb
	Cell-Heating	Heating wire with water reservoir and Pt1000
	B-Field Coil	Solenoid coil with 79 turns and a length of 75 mm
	μ-Metal Shielding	Four cylindrical shells
PM	Power Meter	*Newport Model: 1830-C*
LI	Lock-In Amplifier	*Stanford-Research Systems Model SR830*, see section 5.3.1.
GHz	Microwave Generator	*Rohde & Schwarz SMR 20*, see section 5.3.2
ATC	Atomic Clock	*Stanford-Research Systems: Model FS725* [21]
BT	Bias-Tee	*Mini-Circiuts ZX85-12G+*[10]
FG	Function Generator	*Wavetek Model 180*
OSC	Oscilloscope	*Hameg HM1507 150MHz 200MS/s*

Segment: Laser-Cell-Heating

The Laser-Cell-Heating is the basis for the CPT-resonance spectroscopy. The setup's light source is a VCSEL-diode (LD), which is mounted in a custom housing and is
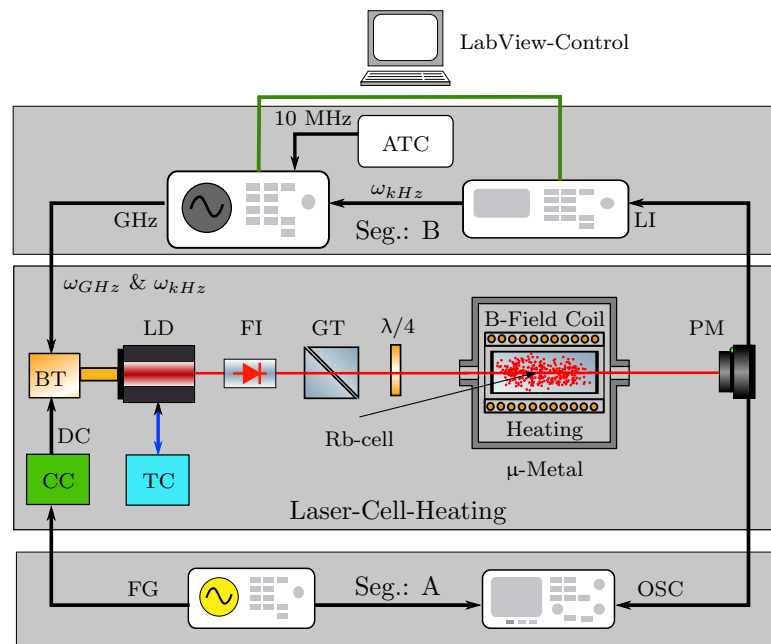
Figure 6.6.: Setup for the CPT-resonance characterisation. It consists of three parts, the Laser-Cell-Heating, the segment **A** for 1-photon spectroscopy and segment **B** for the CPT-resonance spectroscopy.The abbreviations are explained in table 6.1.

regulated by its temperature control (TC) and its current control (CC). The Faraday isolator (FI) prevents it against back reflections. The collimated laser beam is linearly polarised with a Glan-Thompson prism (GT). The following $\lambda/4$ plate[3] transforms the linear polarisation into a circular polarisation. The light is guided through a glass cell, which contains the spectroscopic specimen ^{87}Rb-vapour. The Rb-cell is wrapped with a heating wire and a Pt1000 resistance thermometer is placed directly on the cell. This arrangement is put into a solenoid coil in order to apply a specific homogeneous magnetic field. The heating wire produces an additional magnetic field, so the heating must be turned off during the data recording. To hold the cell's temperature, a small water reservoir is put between the coil and the cell. This reduces the cooling rate to approximately 0.3°C/min instead of more than 2°C/min without water reservoir. These numbers are true for a cell's temperature of 36°C and a room temperature of 22°C. To prevent the cell from additional magnetic stray fields (e.g. the earth's magnetic field) the whole arrangement (cell, heating, water reservoir and coil) is put into µ-metal shielding. This µ-metal is a high permeability ($\mu_r = 10^4$ to 10^5 [23]) alloy. Four shells are used to minimize an external magnetic field influence. Each shell has two holes in order to guide through the laser beam. The transmitted optical power is ultimately detected with a photo-diode (PM).

Segment A: 1-Photon Spectroscopy

Segment **A** is used to detect a 1-photon absorption spectrum of the Rb D_1 line. This spectrum is used for the laser light's wavelength adjustment.

The diode's constant DC current source (CC) is modulated with a 100 Hz triangular signal, which is produced by the function generator (FG). By tuning the laser current and temperature the light's wavelength is changed to fit the ^{87}Rb D_1 excitation of $\lambda = 794.978$ nm. The change of the light's frequency is monitored on the oscilloscope's screen (OSC), which is plugged in at the analogue output of the power meter. With this setup the ^{87}Rb D_1 spectrum in figure 2.4 on page 13 was detected.

The laser light's frequency is set on the 5 ^{2}S$_{1/2}$ F=2 to 5 ^{2}P$_{1/2}$ F=1 transition [4], this ensures the light's wavelength of $\lambda = 794.978$ nm. .

Segment B: CPT-Resonances-Spectroscopy

The CPT-effect is observed with the setup **B** of figure 6.6. Segment **A** has to be disconnected.

The reference function generator of the Lock-In amplifier (LI) produces a kHz-signal, which is guided to the microwave generator (GHz). The FM-mode of the microwave generator is used to modulate the kHz-signal on the GHz-carrier (ω_{GHz} =3.417 GHz). The atomic clock's (ATC) 10 MHz reference is used to stabilise the GHz-signal, this is necessary to ensure the microwave generator's precision of 0.1 Hz. The atomic clock

---

[3]The *B. Halle* $\lambda/4$ plate is made for the wavelength of 795 nm with low order. The low order improves the measurement's quality.

[4] This is the first peak from the right in figure 2.4.

Stanford-Research Systems: Model FS725 Rubidium Frequency Standard [21] provides stable and reliable performance, with an estimated 20 year ageing (long therm stability) of less than $\Delta\nu/\nu = 5\cdot10^{-9}$.

Via the bias-tee (BT) the constant current of the (CC) and the modulated GHz-signal are combined and guided to the laser. The laser light (wavelength of 794.879 nm) is frequency modulated by direct laser current modulation (see section 3.5). The GHz-signal with the kHz-side bands is used as the baseband signal. The so created spectrum is shown in figure 6.3.

The optical power is detected with the power meter (PM) and the signal is evaluated by the lock-in amplifier (see section 5.3.1). By slowly varying the GHz-signal the absorptive signal as the inphase component and the dispersive signal as the quadrature component are recorded by the lock-in amplifier. From the dispersive signal the CPT-resonance frequency, the CPT-linewidth and the CPT-amplitude are determined, see figure 6.5.

Therefore the GHz-frequency must be set manually followed by a manual data recording of the lock-in amplifier's X (inphase) and Y (quadrature) components. This manual recording is time consuming and additionally increases the influence of light frequency drifts and cell cooling rates.

In order to perform fast a GHz-sweep a LabView-automation was realised by remote controlling of the microwave generator (GHz) and the lock-in amplifier, see figure 6.6. A detailed description of the LabView automation programs can be found in section 6.2.

The here presented setup is used for the characterisation of Rb-cells with different Ne buffer gas pressures, which is described in chapter 8.

6.2. LabView-Automation of a CPT-Resonance Setup

For experiments, the automation of certain repeating processes is useful to accelerate the workflow, to reduce handling errors and to ensure the reproducibility of results. For the setup of the CPT-resonance spectroscopy in section 6.1.2, the automation was realised by remote controlling the *SMR20* microwave generator and the *SR830* lock-in amplifier with the help of a PC and the software package *LabView*[5]. The connection from the PC to the devices was established via the General Purpose Interface Bus (GPIB). Information concerning LabView and GPIB can be found on the tutorial website of National Instruments[6].

6.2.1. GPIB Interface

The computer to instrument connection is established with an USB to GPIB interface, which is based on the IEEE-488.2 standard. Therefore the adapter *GPIB-USB-HS+*[14] from *National Instruments* is used. Since this adapter is produced by the same company as LabView, the compatibility to LabView is ensured.

Two devices are remote controlled by LabView. The *Rohde & Schwarz SMR20* microwave generator and the *Stanford Research Systems SR830* lock-in amplifier. In the section 5.3 a detailed description of these instruments can be found. In this section, just the information concerning the LabView automation is presented.

The GPIB communication is based on a "talker" and "listener" principle. The PC sends a request while a device is listing, for the answer the PC listens and the device talks. The sending and receiving is based on text commands, some of them are valid for all devices (e.g. such as assigning addresses), but most of them are specific for each instrument and have to be looked up in the specific manuals.

The GPIB-interface has to be initialised and searched for devices, in order to address a plugged in device.

6.2.2. LabView Programs

LabView is a visual programming language. The single functions are visualised as boxes and the data and information flow is shown as wires. LabView creates a graphical user interface (GUI) automatically for each combination of functions. By combining several of these functions a SubVI can be created. This serves as a new function for more complex tasks. For this project a lot of SubVIs were created, these are shown in table A.1 combined with a short description.

For the usability of the made programs in combination with the experimental setup, it was important to simplify and automate as much processes as possible. Therefore the initializing of the instruments were automated just as the file management. Produced data is saved automatically combined with date and timestamps.

---

[5]LabView 2012, Service Pack 1, Version 12.0.1f5 (32-bit)
   ©1986-2013 National Instruments
[6]National Instruments - Tutorials: LabView and GPIB in German and English
   `http://www.ni.com/tutorials/d/` 1st of December 2015

In the following sections just the main ideas of the programs are presented. In the appendix, their GUIs are explained including a small manual, see section A.1.

6.2.3. Software Workflow Concept

The CPT-resonance spectroscopy of section 6.1.2 requires to set first a certain frequency with the GHz generator, followed by the recording of the X and Y components of the lock-in amplifier. Therefore the software was designed to increase the frequency in steps to guarantee this sequence. Each step has to be finished until the next one is allowed to start, no parallel tasks, which involve the instruments, are allowed.
The schematic workflow is shown in figure 6.7. The boxes symbolise SubVIs, which are build to handle the devices' communication. The blue colour labels the *SMR20* and the green the *SR830*. The red arrows indicate the order of the execution of the single boxes. The yellow box refers to the measurement data file management, which is also realised in LabView. In figure 6.7, both devices get configured and the sweep parameters are
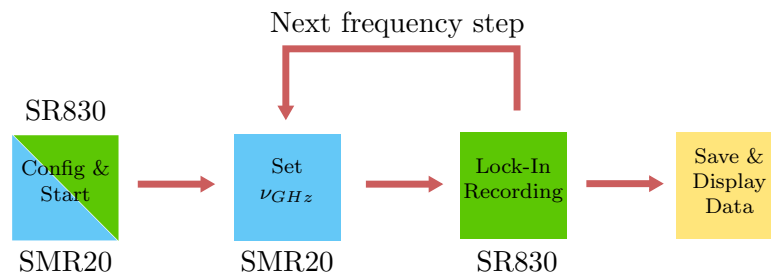

Figure 6.7.: Basic workflow concept of the LabView automation. The single coloured boxes refer to the devices. The red lines represent the LabView program structure. The yellow box indicates the data visualisation and file management.

set (blue/green coloured box). The GHz start frequency $\nu_{GHz} = \nu_{start}$ is set (blue box). After the frequency is set, the LabView program starts the lock-in amplifier's recording of the inphase and the quadrature components (green box). The data is displayed and saved to the measurement data file (yellow box). The GHz-signal is set again with the frequency $\nu_{GHz} = \nu_{start} + \nu_{step}$ and the lock-in amplifier detects again. This procedure is followed until the stop frequency is reached: $\nu_{GHz} = \nu_{stop}$.

Central Sweep Mode

The central sweep mode program implements the schematic workflow from figure 6.7. Its job is to perform an automated CPT-resonance scan. In figure 6.8 a more detailed diagram of the program's structure is shown. The actual LabView program structure is not shown because of its lack of clarity. Although figure 6.8 resembles the actual structure in the essential parts. This diagram is built as a SubVI (see SubVI number 9 in table A.1) for later implementation in more complex structures.
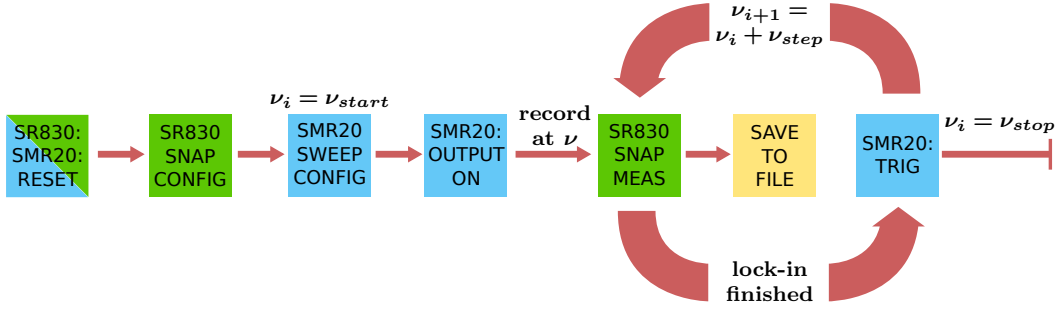
Figure 6.8.: Diagram of the central sweep mode. The lock-in amplifier *SR830* and the microwave generator *SMR20* are reset and than configured with the device sets. The *SMR20* GHz output is activated. The lock-in records at ν and the data is saved. After this the trigger-command is sent to increase the GHz-frequency by ν_{step}. The sweep stops when $\nu_i = \nu_{stop}$. A semicolon after the device's name indicates, that the box is a single command. Boxes without a colon are SubVIs, which can be found in table A.1.

The boxes (in figure 6.8) with a colon after the device's name are meant to resemble single commands which are sent directly to the devices, while the boxes without semi-colon after the device's name symbolise SubVIs, which can be found in table A.1.

At the beginning of each frequency sweep, both devices (*SMR20* and *SR830*) are reset to its default settings, to ensure the same starting conditions for every sweep. After this, the devices are configured for the sweep with all the necessary parameters. The *SR830* parameters are listed at the description for the SubVI number 3. The *SMR20* provides a special built-in sweep mode. This allows to set a start frequency ν_{start}, a step frequency ν_{step} and a stop frequency ν_{stop}. This built-in sweep mode increases the output frequency from ν_i to ν_{i+1} when a trigger command is send to the *SMR20* via the GPIB-interface, see SubVI number 8

After the devices' configuration the *SMR20* GHz-output has to be activated. The start GHz-frequency ν_{start} is set. The lock-in amplifier *SR830* records the first set of data (SubVI number 4). The program allows to record the X and Y data several times in order to calculate their mean values. This reduces signal noise but slows down the scanning speed. The mean-values for the inphase and the quadrature signal are displayed on the screen and saved to the measurement data file. After this the *SMR20* gets triggered, this sets a new GHz frequency $\nu_{i+1} = \nu_i + \nu_{step}$ and the lock-in records again. This procedure is continued until $\nu_i = \nu_{stop}$ is reached.

Monitoring Mode

In order to find the right sweep-parameters it is useful to have a monitoring mode program. This monitoring mode allows to display the lock-in data by simultaneously changing the configuration parameters of the *SMR20* and the *SR830*. This monitoring

mode does not record any data.

For this monitoring mode, most of the SubVIs, which were made for the central sweep mode, are used. Just the *SMR20* sweep-configuration function (SubVI number 8) had to be replaced. The *SMR20* is set on a fixed frequency, see SubVI number 7. In figure
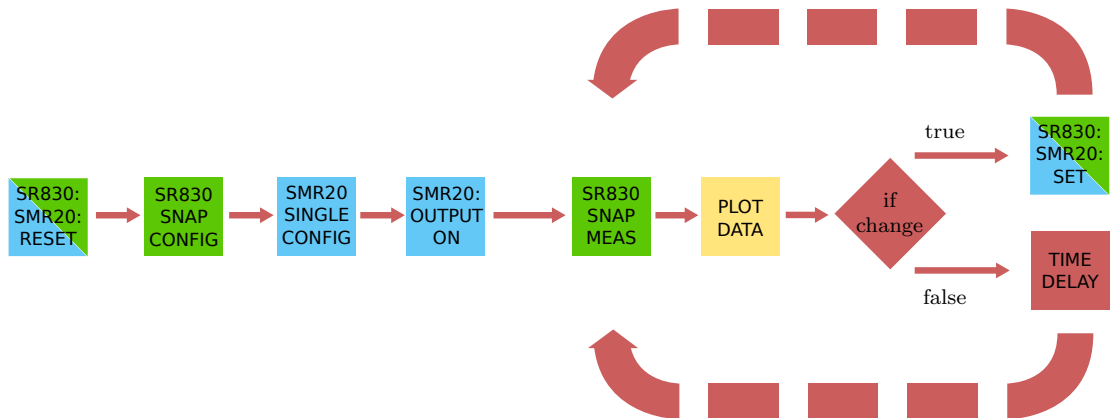

Figure 6.9.: Diagram of the monitoring mode. Both devices (*SMR20* and *SR830*) are reset and configured. The *SMR20* is set on a fixed frequency while the *SR830* records data, which are plot. An if-statement checks if some configuration parameters are changes, if true the parameter get set, if false a time delay regulated the lock-in's readout speed. The single used SubVIs can be found in table A.1. This diagram is realised as SubVI number 10.

6.9 a schematic diagram of the monitoring mode is shown. The devices get reset to their default settings, configured and the GHz-signal output is turned on. The lock-in recording (SubVI number 4) is followed by an if-statement. This if-statement checks if some configuration parameters were changed in the graphical user interface (GUI). If the statement is true, these specific parameters are set, if the statement is false, a small time delay is used to regulate the lock-in's readout speed. A stop function (not shown in figure 6.9) cancels the loop. This monitoring mode is also realised as SubVI with the number 10.

Combination of the Monitoring Mode and the Sweep Mode

The integration of the monitoring mode and the central sweep mode in one GUI leads to a general recording program. The program's usability is further increased by including the initialising and addressing SubVIs (numbers 2 and 1). In figure A.1 (shown in the appendix on page 89) the GUI is shown, combined with a small manual.

For keeping track of the experiments, a daily log-file is created automatically. In this file all configuration parameters of each sweep are saved with the possibility of adding some annotations before and after the sweep procedure. The log-file SubVI's number is 13.

Analysis Tool

The data analysis is simplified by an analysis tool. This allows to read out the measurement data files. The GUI is shown in figure A.2. This program lists the configuration parameters of a sweep and plots the recorded data points. It also allows to stack several different plots in order to compare different sets of data.

By placing cursors within the plot, the linewidth, the amplitude and the resonance frequency can be measured directly with this analysis tool.

6.3. Construction of a Laser-Collimation-Control System

The CPT-resonance linewidth is a function of the laser light's intensity, see section 2.2. Higher intensities result in a broadened linewidth. This effect is called power broadening [19]. The laser light's intensity is the optical power divided by the beam profile's cross-sectional area, see section 8.2.5. Therefore the intensity is increased either by a greater optical power or by the reduction of the beam profile's cross-sectional area.

In general, laser-diodes have an large angle of divergence (e.g. VCSEL: $15°$ to $20°$, see section 3.8 and DFB-laser: $5°$ to $50°$ see section 7.3.2). Therefore a lens is used in most applications to focus or collimate the laser beams. In order to minimise the CPT-linewidth power broadening, the laser beam is used for collimation.

Although, in the case, where the laser beam is focused - with its collimation lens- within the Rb-cell, the smaller beam cross-sectional area will increase the intensity and this broadens the CPT-linewidth.

In figure 6.10 a CPT-linewidth broadening factor as a function of the beam's focal length is shown. This factor is a multiple of the CPT-linewidth at the beam's focal length of
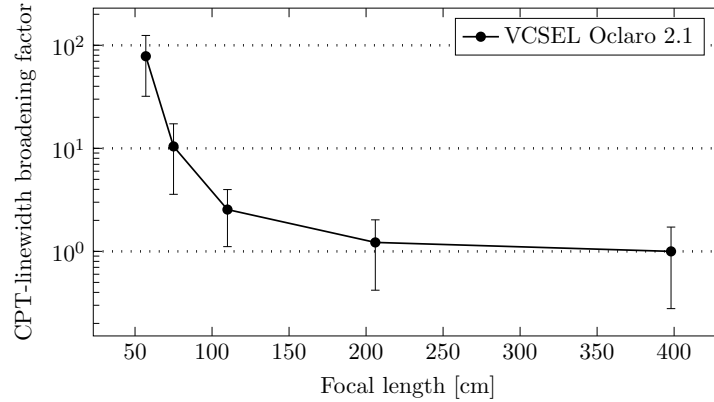

Figure 6.10.: CPT-linewidth broadeing factor as a function of the focal point of the VCSEL Oclaro 2.1 laser. The linewidth increases more than exponantially for shorter focal lengths.

400 cm. The CPT-linewidth increases more than exponential for a shorter focal length. Even at a focal length of 200 cm the CPT-linewidth is increases at a factor of 1.5 . In this figure, the importance of the laser beam's collimation for the CPT-resonance characterisation and ultimately for the CDSM's precision (see section 2.5) is shown.

In order to analyse the collimation quality of a laser with collimation lens or a fibre coupler, the Laser Collimation Control (LCC) system was designed. The LCC's concept is illustrated in figure 6.11 and in table 6.2 the single elements are listed.

The basic idea is to use a *Bestform* lens (2 in figure 6.11) to focus the beam (which collimation has to be controlled) and investigate the beam's focal spot size on a webcam's CCD sensor (1). The CCD sensor is placed in the lens' (2) focal plane f_{BF}. If the beam

is collimated perfectly, just a small spot is illuminated on the sensor. This beam image is observed via a webcam-software. The more the beam's collimation deviates from its perfect collimation - the beam gets focused - the larger the illuminated spot will get. This allows to quantify the beam's collimation, which is otherwise hard to investigate. The focal spot size is the criteria for the collimation of the beam. This criteria can be used for the collimation of a laser lens or a fibre coupler (6 in figure 6.11). By adjusting the relative position Δf_{beam} between a laser and its collimation lens and watching for the smallest spot size on the PC screen, the Laser-Fibre-System is collimated.

The accuracy of the collimation criteria depends on the position of the CCD sensor with respect to the *Bestform* lens' focal plane f_{BF}. By investigating the image's sharpness of a distant object (e.g. a house farther than 30 m) on the webcam sensor via the webcam-software of, the CCD's position relative to the *Bestfrom* lens is set. A sharp picture of a distant object - the object distance is assumed to be infinite - indicates that the CCD sensor coincides with the *Bestform* lens' focal plane.

To minimise the influence of the chromatic aberration on the adjustment of the optimal lens to CCD distance a low pass IR-filter (3 in figure 6.11) is used. Together with the decreasing IR-sensitivity of the CCD-chip, a bandpass filter in the wavelength region of the laser wavelength (795 nm), which is used for the setup in 6.1.2 and the CDSM is created, see figure 6.12.

A variable attenuator (4 and 5) allows to adjusted the LCC to different light intensities. This is done by rotating a linear polarising elements in respect to the polarisation direction of a second linear polariser.
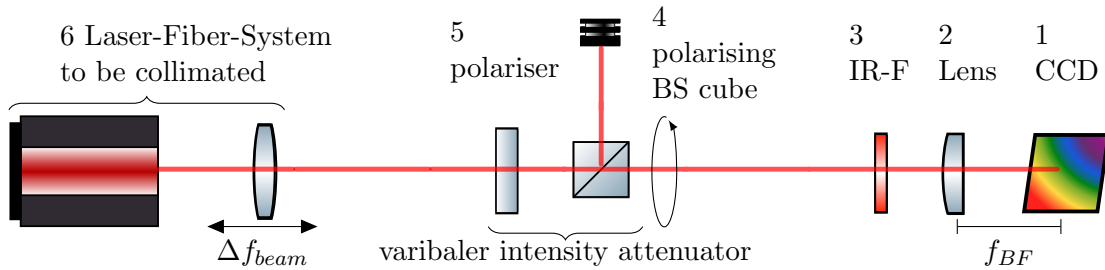

Figure 6.11.: Concept for the Laser Collimation Control (LCC) system. The elements from (1) to (5) are part of the LCC and are listed in table 6.2. Element (6) symbolises different beam sources such as laser collimators and fibre couplers.

The following list describes the used components in detail, the numbers refer to those in figure 6.11 and table 6.2.

1. **CCD**
   A conventional webcam (*Trust Spotlight webcam - 16429*) was used for the design of the LCC. Its CCD-chip has a resolution of 640x480 pixel with the dimensions of $\sim$ 2.0 mm x 1.5 mm which results in a pixel size of 3.1 μm x 3 μm. This model without autofocus and removable lens enables a manual focussing and the removal

Table 6.2.: Functional elements used in the LCC system

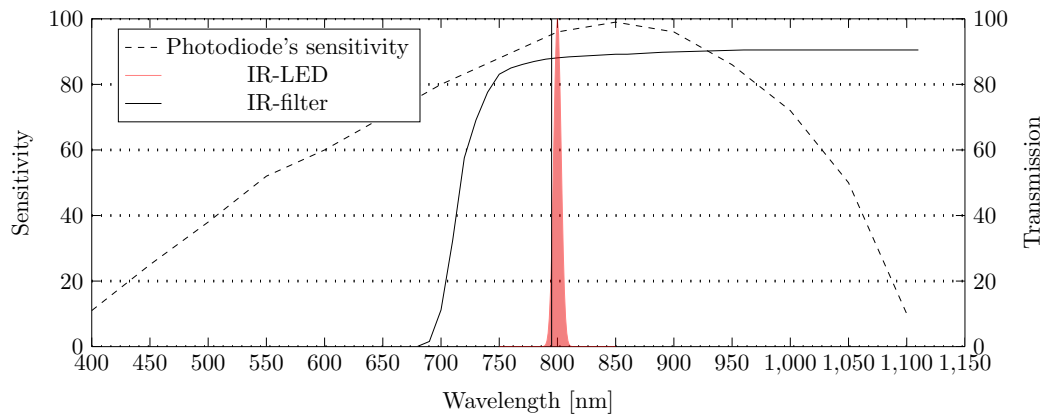| Number	Name	Function
1	CCD	Detecting of beam's diameter
2	Lens	*Bestform* lens for beam focusing
3	IR-F	IR-transmission over 700 nm
4	Polarising BS cube	Rotatable polarising beam splitter cube
5	Polariser	Fixed linear polariser

Figure 6.12.: Bandpass filter characterisic of the LCC. The IR-filter transmits wavelengths over ≈ 700 nm, while the photodiode's sensitivity[43] ranges up to ≈ 1100 nm. The laser wavelength of 795 nm is shown (black vertical line). Additionaly the IR-LED's emission spectrum, with a central wavelength of 800 nm, is drawn in. The LED is used as a referance object for the LCC adjustment.

of the default lens. In addition a webcam allows to display the image via a PC. First tests showed that the default lens could not focus the laser beam in adequate manner. On the computer image, no difference between an focused and a collimated beam was recognisable. Therefore the lens was changed.

2. **Bestform Lens**
The *Bestform* lens (*B. Halle OBF020*) replaces the default lens. The *Bestform* lens is described in 4.1.3. Its specifications are [7]:

B. Halle:	OBF020
optical glas:	SFL57
focal length f_{BF}:	20 mm
diameter:	20 mm

For the new lens a mounting was designed, which is schematically figured in 6.13. This mounting consists of two elements, which fit in the screw thread of the webcam. Therefore no additional changes had to be made on the webcam's housing. The mechanical drawing of the *Bestform* lens housing can be found in the appendix A.10. A S+K-connector (see section 4.2.6) was added for further extensions.

3. **IR-Filter:**
Within the lens mounting, see 6.13, the IR-transmission filter was placed by fixing the filter with an additional aluminium spacer. This filter is normally used in IR-photography. Its lowpass characteristic, transparent over approximately 700 nm[7], is shown in figure 6.12.

Cokin filter:	A007
Wrattennumber:	89A
trimmed:	ø 19.5 mm

4. **Polarizing Beam Splitter Cube**
in order to adjust the LCC to different light intensities, a variable attenuator was added to the system. This element is combined by two linear polarising elements. One if fixed and the other is mounted rotatable.
The rotatable polariser is a beam splitter cube in a custom mounting. This polariser was used in previous projects. A S+K mounts is placed on both sides.

B. Halle:	PTW 1.10
Spectral range:	600 - 900 nm
Extinction:	10^3:1
Transmission:	> 95
Cube Size:	10 mm

---

[7]Kodak Homepage: 15th of October 2015 `http://motion.kodak.com/us/en/motion/products/lab_and_post_production/kodak_filters/wratten_2_filters/default.htm`
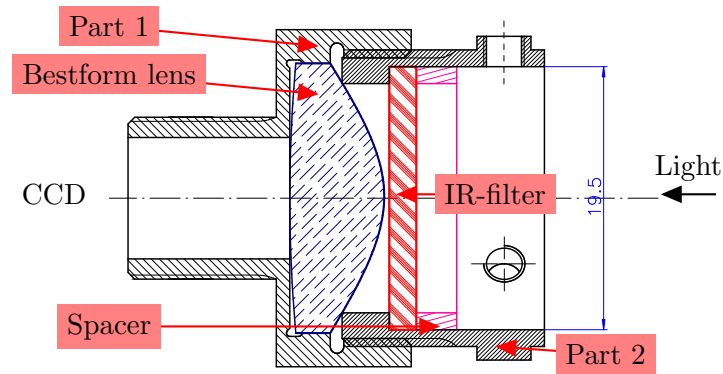
Figure 6.13.: Overview of the LCC lens mounting. Dimensions in mm. The mechanical drawings of Part 1 and Part 2 can be found in A.10. The IR-filter is held in place with an aluminium spacer. The thread fits to the webcam.

5. **Dichroic Glass Polarizers**
   The second linear polariser is a dichroic glass polariser from the S+K company.

S+K:	5PF-P - 750-L
Spectral range:	750 - 1250 nm
Extinction:	10^4:1
Transmission:	> 87-93
Clear aperture:	12 mm

6. **Laser-Fiber-System**
   The S+K connector allows to plug in different optical components, whose collimation must be checked and if necessary corrected.

The final assembly is shown in the picture 6.14. By using elements of the S+K MultiCube system (see section 4.2.6) the stability was improved. Above, the adjustment of the distance between *Bestform* lens and the CCD sensor is described. To improve this process a reference light source with a reference distance between this light source and the LCC is defined. A IR-LED *LED800-01AU* [29] with the emitting wavelength of 800 nm in a distance of 10 m was chosen for the adjustment of the lens to CCD sensor distance. The LED's wavelength corresponds approximately to the laser light's wavelength and therefore they should experience the same chromatic aberration. The LED's spectrum is shown in figure 6.12.
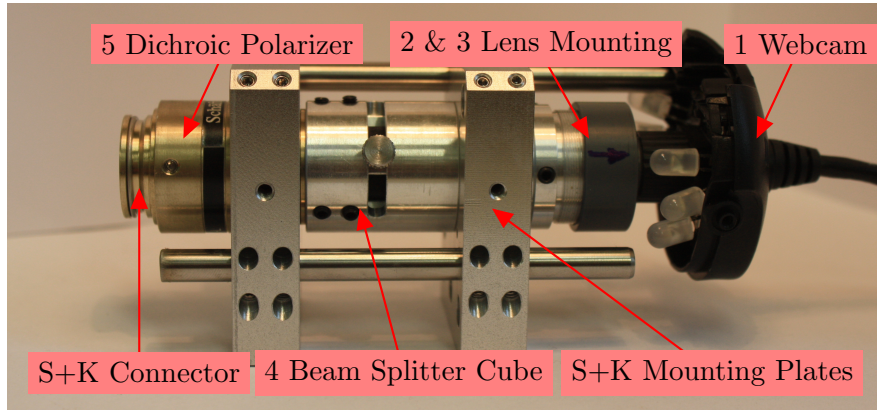
Figure 6.14.: Fully assembled Laser Collimation Control (LCC). The numbered elements are listed in table 6.2. The stability was improved by elements S+K mounting plates. The S+K connector on the dichroic polarizer allows a direct connection of S+K fibre couplers and other ø19.5 mm compatible optical elements.

6.3.1. Applications of the LCC

The commercial software[8] is used to display the image of the laser beam. The element, which collimation should be controlled or adjusted, is plugged onto the LCC, the S+K connector is shown in figure 6.14 on the dichroic polarizer. The beam's intensity must by set by the variable attenuator in order to minimise interference effects and to prevent the CCD-sensor from over-driving. For light intensities (> 1 mW) it is necessary to reduce the sensitivity of the CCD sensor. This is done by the software.

To ensure the correct setting of the LCC the device must be focused on the reference light source. This is done by rotating the modified lens mounting relative to the CCD sensor, so the chip is moved into lens' focal plane.

6.3.2. Characterisation of the LCC

For an ideal LCC configuration (CCD sensor in the focal plain of the *Bestform* lens and perfectly collimated beam) the focal spot size $2 \cdot w'_0$, which illuminates the CCD sensor, is calculated for a Gaussian beam. The calculation of equation (4.10), with the maximal usable lens' diameter[9] $D = 9$ mm , its focal length $f = 20$ mm and the laser beam's wavelength $\lambda = 795$ nm results in a beam diameter of $2 \cdot w'_0 \approx 3$ μm.

By comparing this value to the size of a single pixel (≈ 3.1 μm x 3 μm), maximal four pixel at the time should be illuminated for the ideal configuration.

In figure 6.15 the CCD-image of an uncollimated beam (a) and a collimated beam (b)

---

[8]*Debut Video Capture Software* v 2.12

   Distributed by NCH Software `www.nchsoftware.com/capture`

[9]See the mechanical drawing A.10 of the lens mounting. The lens is maximal illuminated by beam with a 9 mm diameter.

is shown. These images were taken in the course of the fibre coupler collimation of the

(a) This uncollimated laser beam results in a large spot on the CCD sensor.

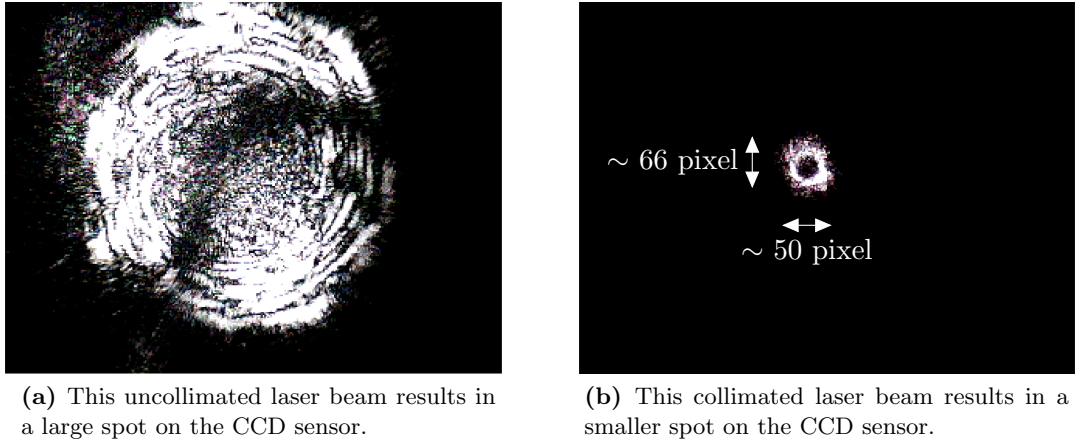**(b)** This collimated laser beam results in a smaller spot on the CCD sensor.

Figure 6.15.: Collimation of the DFB-laser diode setup of figure 7.1 with a fibre coupler and a MMF.

DFB-laser setup in section 7.1. The DFB-laser's beam was guided through a MMF and a fibre coupler to the LCC. In (a) an interference pattern is visible due to diffraction at the lens mounting's aperture and a interference effects between the len's surfaces. Additionally a coma-like structure is seen, this indicates that the laser beam enters the *Bestform* lens in an oblique angle. This corresponds with the fact that the beam's center does not coincide with the sensor's center.

In (b) the image of an collimated beam is seen. The beam's cross-sectional area is approximately 50 pixel x 66 pixel, which corresponds to 155 μm x 193 μm. The *Blooming* effect , where a overcharged pixel transfers its overcharge to its neighbouring pixels, is responsible for the broad beam image as much as misalignments. Besides the LCC's variable reducer an arbitrary exposure setting within the webcam's software allows to enhance the image's contrast by reducing overdrive effects.

7. A DFB-Laser Diode for CPT-Resonance Spectroscopy

In the CDSM project, the laser commonly used for CPT-resonance spectroscopy is a VCSEL-diode. Due do its GHz-frequency modulation capability this laser diode is well suited for direct laser current modulation (section 3.5). The VCSEL's linewidth (typically > 50 MHz) is in the regime of the natural linewidth (or slightly above) of the $5\ ^2P_{1/2}$ to $^2S_{1/2}$ transitions of the ^{87}Rb-atoms ($\delta\nu \approx 6$ MHz [48]).

A smaller laser linewidth should only increase the excitation efficiency because the entire line (laser frequency spectrum) lies within the natural linewidth. This, in theory, should not have an influence on the CPT-resonance amplitude and CPT-resonance linewidth. Although, CPT-resonances of smaller linewidths (down to 30 Hz) and, compared to the VCSEL based CPT-resonance experiments, higher resonance amplitude ($\sim$10 times larger) have been observed. This was achieved by a two coupled laser Phase Lock Loop (PLL) setup [28] where the laser light's linewidth is 100 kHz. This bulky setup is unsuitable for space missions due to its highly complex design consisting two phase-locked lasers and its frequency stabilisation with an extra Rb-cell.

The CPT-resonance excitation performance, achieved with the PLL setup, suggests that a different laser diode technology, which enables a similar simple setup (like the VCSEL-setup, see section 6.1.2) but with a smaller laser linewidth, could improve the accuracy of the CDSM.

A DFB-laser features a smaller laser linewidth (< 2 MHz) but the high frequency modulation capability (up to 3.4 GHz, see section 6.1.1) is not known in the context of this CPT-spectroscopy setup.

This chapter deals with the integration of a DFB-laser diode into the current CPT-resonance spectroscopy setup by the design of a custom laser diode housing. This housing is characterised and the DFB-laser diode's capability for spectroscopy is investigated.

7.1. DFB-Laser Diode Characterisation Setup

In figure 7.1 a 1-photon spectroscopy setup for the DFB-laser is shown. It is similar to the VCSEL's FM-spectroscopy setup in section 6.1.2. For the DFB-laser the segment Laser-Cell-Heating and the segment **A** (the 1-photon absorption setup) are adapted. The magnetic shielding is not necessary for the 1-photon absorption characterisation. The diode is mounted within a custom housing.
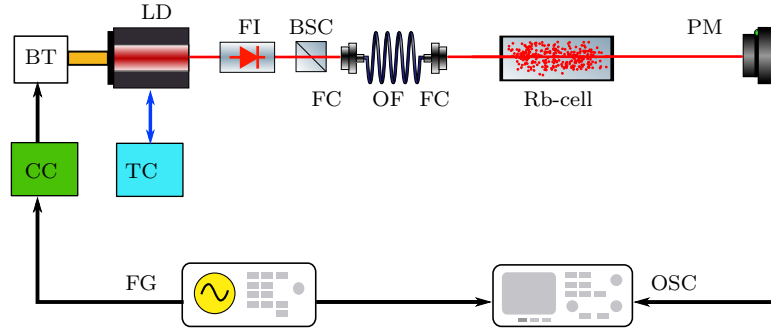
Figure 7.1.: ^{87}Rb vapour 1-photon spectroscopy setup for the DFB-laser. The abbreviations of the single devices and elements are listed in table 6.1.

Table 7.1.: List of abbreviations for the devices and elements used in the DFB 1-photon spectroscopy setup, which is shown in figure 7.1.

Acronym	Name	Description
LD	DFB-Diode	*Toptica 795 nm*[41] in a custom housing
TC	Temperature Control	*Toptica DTC 110 T03 edition*[15]
CC	Current Control	*Toptica DCC 100* [15]
FI	Faraday Isolator	*S+K 48FI-5-780*
BSC	Beam Splitter Cube	*S+K 48BM-CC-B*
	Rb-Cell	buffer gas free ^{87}Rb cell
FC	Fibre Collimator	*S+K 60SMS-1-4-A11-02*
OF	Optical Fibre	*S+K MMF-VIS/NIR-200-NA022-3-APC-0-500*
PM	Power Meter	*Newport Model: 1830-C*
BT	Bias-Tee	*Mini-Circiuts ZX85-12G+*[10]
FG	Function Generator	*Wavetek Model 180*
OSC	Oscilloscope	*Hameg HM1507 150MHz 200MS/s*

7.2. Construction of a DFB-Laser Diode Housing

7.2.1. Design Requirements

The here presented DFB-laser housing design is indented to be the prototype for future potential implementations into the CDSM. This design was created for a laboratory environment. Additionally, future space applications were taken into account during the design process in order to minimize the number of changes for an actual flight model. This design is based on a previous VCSEL diode housing, which is already used in the *China Seismo Electromagnetic Satellite Mission*.

The goal of this design was to create a mechanically robust and compact housing for the laser diode with included temperature control and HF modulation possibility. The temperature control is achieved by a thermoelectric cooler (TEC) Peltier element combined with a negative temperature coefficient (NTC) thermistor and set by a control loop. For HF modulation, the housing introduces an extra impedance step to reduce side band power losses due to HF reflections. This housing consists of multiple parts with different functionality, but all individual parts are designed to center the DFB-laser to the geometrical and optical axis because the DFB-laser dye is mounted in its T09 package eccentrically with an offset of ~ 0.4 mm. Therefore the diode has to be positioned eccentrically in respect to the rotation axis of the housing to align the optical axis with the rotational axis. This simplifies further optical setups and the actual use in the laboratory. Furthermore the housing is designed for simple function, handling and manufacturing.

Table 7.2 lists the electrical and optical parameters of the used DFB-laser diode (*# LD-0795-0020-DFB-1*) from *Toptica Photonics AG*.

Table 7.2.: DFB-laser diode *# LD-0795-0020-DFB-1*: Optical and electrical characteristics at 25.0°C and $P_O = 15.0$ mW[41]

Item	Symbol	Min	Typ	Max	Unit
Max. Optical Output Power	P_O		15.0		mW
Operating Temperature	T_{op}	10.0	25.0	35.0	°C
Threshold Current	I_{th}	10.0	15.0	25.0	mA
Operating Current	I_{OP}	-	40.0	50.0	mA
Operating Voltage	V_{OP}	-	2.5	3.0	V
Slope Efficiency	η_s	0.6	0.8	1.0	W/A
Lasing Wavelength	λ_p	794.1	795.0	796.0	nm
Temperature dependence	$d\lambda/dT$	-	0.06	-	nm/K

7.2.2. Design Overview

In figure 7.2 an schematic overview of the design is given. All individual parts are placed where they are in the assembled housing. Each element is numbered and labelled. A

7.2. Construction of a DFB-Laser Diode Housing

short description is listed in table 7.3 with the corresponding numbers. The detailed mechanical drawings can be found in the appendix A.2.1.
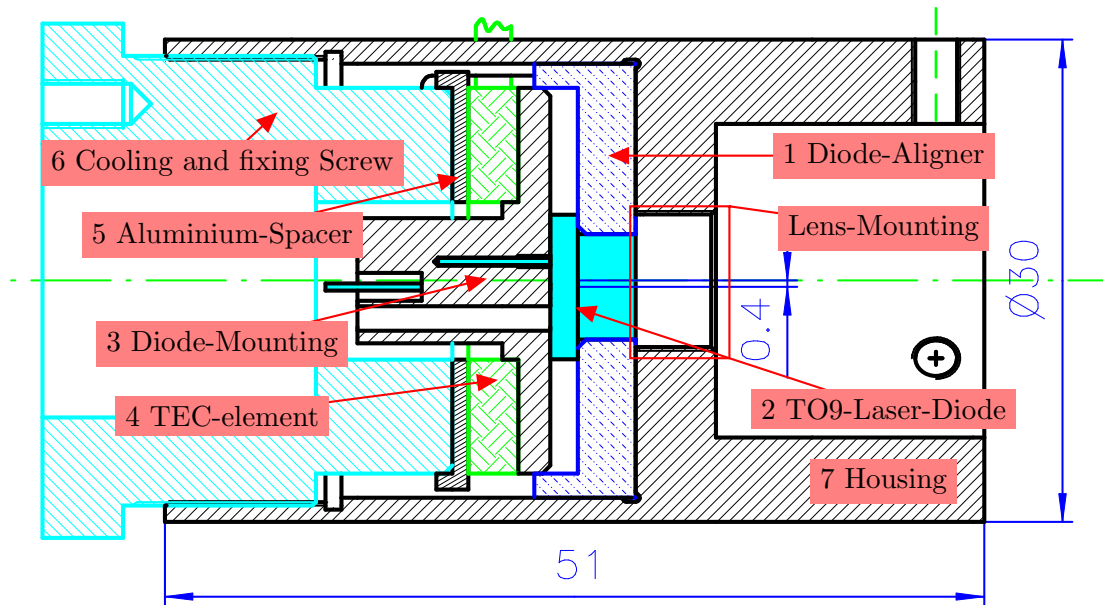

Figure 7.2.: Overview of the DFB-laser diode housing with all used parts numbered. For a part list see table 7.3 . Dimensions are in mm.

Table 7.3.: Short part list of the DFB-laser housing. For non-purchased parts the material is listed. The specific mechanical drawings can be found in the appendix.

Number	Name	Function	Material	Technical Drawing
1	Aligner	electric and thermal isolation	Macor	A.3
2	TO9	Diode package	-	[41]
3	Mounting	HF and thermal connection to diode	brass	A.4
4	TEC	heat source and electric isolation	-	A.5
5	Spacer	reduce shear force on the TEC	aluminium	A.6
6	Screw	heat sink and mechanical fixing	aluminium	A.7
7	Housing	robust enclosure	aluminium	A.8

7.2.3. Description of the Individual Parts

The following lists describes the part's functionality of table 7.3 in more details. All parts, except the diode, the TEC-element and the thermistor were manufactured in the workshop of the *Institut für Experimentalphysik* at Graz University of Technology.

1. **Diode Aligner:**   Mechanical drawing: A.3
   The diode aligner fixes the diode in its place. The center hole is shifted by 0.4 mm with respect to the rotational center in order to align the laser beam on the geometrical axis. The material *Macor* [1] insulates the laser diode from the aluminium enclosure electrically and thermally. This prohibit a thermal short-cut between both sides of the TEC-element (part 4). The raised boundary guides the diode mounting (part 3) in order to keep it centred. It simultaneous isolates the diode mounting thermally from the aluminium enclosure (part 7). Additionally, the diode aligner reduces lateral shear forces on the laser diode.

2. **TO9-Laser Diode:**   Mechanical drawing: [41]
   The DFB-laser diode *# LD-0795-0020-DFB-1* [41] from *Toptica Photonics AG* in a TO9 package is used. The technical details are found in table 7.2. The pins had to be cut in order to make electrical contact, this is described in the section about the diode mounting.

3. **Diode Mounting:**   Mechanical drawing: A.4
   This component has two functions. Firstly making thermal contact from the diode, via the aluminium spacer, to the TEC-element and secondly establishing electrical contact with the diode's pins.
   For an optimal thermal contact the conduction surface to the diode was maximised. To measure the diode's temperature a drill-hole for inserting a thermistor was added. The 10 kΩ NTC-resistor *B57550G1* [32] from the company *EPCOS* was used as thermistor. For delivering electrical power with a high frequency modulated current to the diode a formstable microwave coaxial cable [46] was used. This is soldered to the brass diode mounting, which acts as the diode's ground contact because the diode's package, pin 2 and 3 are grounded. Brass allows the direct soldering of the wire. For the pin layout see the diode's data sheet [41]. By pressing the mounting against the diode a reliable electrical contact is achieved. Before soldering the wire to the brass, the cable was cut to expose the inner conductor without the dielectric material around. This is done to connect the wire's inner conductor with the anode pin of the diode. Therefore a special SMA-connector is used. This is shown in figure 7.3. By this method a new coaxial cable is formed with a length of a few millimetre. The air gap is the new "cable's" dielectric material. In order to adapt the impedances of the microwave cable (50 Ω) to the laser diode, an intermediate impedance level is introduced.

---

[1] MACOR: machinable glass ceramics from the company *Corning* 9th of December 2015:
`https://www.corning.com/cala/en/products/advanced-optics/product-materials/`
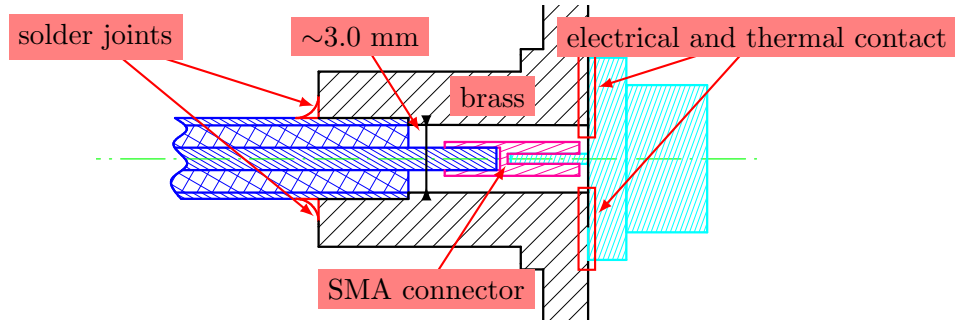`specialty-glass-and-glass-ceramics/glass-ceramics/macor.html`

Figure 7.3.: Schematic drawing of the soldered coaxial wire (blue) to diode mounting (black). The coaxial cable grounds the brass diode mounting and so the diode's package (turquoise). The anode pin is attached to the inner conductor of the coaxial cable via a special SMA connector (magenta).

Therefore the diameter of the brass-drilling was calculated to correspond with 70 Ω impedance. The impedance is a function of the used dielectric material (in this case: air) and the diameter of the inner conductor. The equation (5.2) with the inner diameter of the microwave cable (0.92 mm) result in the outer diameter of $\sim$ 3.0 mm. This wire to brass to diode connection is shown in figure 7.3. The exact impedance of the laser diode is not known, but it is higher than 70 Ω and a function of the laser current.

A TEC guiding step is designed to prevent a thermal short-cut between both sides of the TEC-element.

4. **TEC-Element:** Mechanical drawing: A.5

   The TEC-element *CH-38-1.0-0.8* [9] from *TE Technology, Inc.* is used to transport the heat from the brass diode mounting via the aluminium spacer to the cooling screw. By using a round module with a center hole it is possible to achieve quick heat exchange by maximising the surface area. The center hole allows to guide the electrical connections in a adequate manner to the diode mounting. Additionally this specific model is available in a sealed configuration, which is necessary for space missions. The table 7.4 shows the electrical and thermal characteristics of the used element.

5. **Aluminium-Spacer:** Mechanical drawing: A.6

   To prevent damages to the brittle TEC-materials a spacer was added to weaken shear forces introduced by the fixing screw. Aluminium was chosen for its high thermal conductivity.

6. **Cooling and Fixing Screw:** Mechanical drawing: A.7

   The screw works as the heat sink of the construction by pressing the all individual parts (1-5) against the housing. This also ensures a reliable electric contact to the diode. The inner hole allows the wires to be guided to the diode mounting.

Table 7.4.: TEC-element: Thermal and electrical characteristics [9]

	Material Specifications (27°C hot side temperature)	Material Specifications (50°C hot side temperature)
V_{max} (V)	4.7	5.2
I_{max} (A)	5.8	5.8
Q_{max} (W)	16.8	18.4
DT_{max} (°C)	69	78
Operation/storage temperature	-40°C to +80°C	

Additionally an external heat sink can be mounted with three M3 screws on the back. A black heat sink is shown in figure 7.4.

7. **Housing:**   Mechanical drawing: A.8

   The aluminium enclosure fits all components of the DFB-laser housing. Two slotted holes are added in order to guide the TEC-element's wires through the housing and ensures simple assembling and disassembling.

   The mechanical housing is designed for the use of a already existing lens mounting. The therefore necessary thread is labelled in figure 7.2. The used lens was a aspheric objective lens *F-LA11* from the company *NEWPORT* with a NA of 0.4 and a focal length of 6.24 mm. It also was convenient to add an optical connector which dimensions (ø 19.5 mm) are used by the S+K company, see section 4.2.6. So the Laser housing can be combined with existing components and can be integrated in already existing setups.

In figure 7.4 the fully assembled DFB-laser housing is shown. It is mounted on a S+K Faraday isolator (*48FI-5-780*) with an attached beam splitter cube. For further experiments two fibre couplers are added. This additional optical elements are part of the S+K MultiCube system (*48MB-19.5-150*).

In order to support the housing's weight and to manage the wires a supporting construction is added. The mechanical drawing is found in the appendix A.9.

7.2.4. Electronic Control of the DFB-Laser

For the DC current and temperature control the *Diode Laser Controller DC 100* [15] from *Toptica* was used with their specific submodules for current and temperature.

Temperature Control

The temperature submodule is the *DTC 110 T03 edition*. It allows a TEC-current up to 5 A with a maximum output power of 30 W. The temperature range is controllable in the range of 0°C to 50°C with a stability of < 2 mK for the stock laser head *DL 100*.
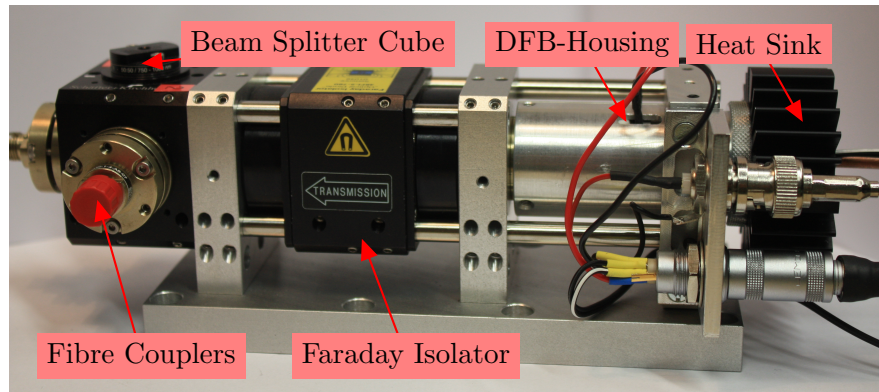
Figure 7.4.: The fully assembled DFB-diode housing is mounted on a S+K Faraday isolator. A beam splitter cube with two attached fibre couplers is added for further experiments. The black heat sink is added for a better heat exchange.

Current Control

The current submodule is the *DCC 100*. The maximum current output is 500 mA with a low noise smaller than 10 µA. This DC current is connected with the laser diode by a coaxial cable through a Bias-Tee.

High Frequency Current Modulation

For the direct laser current modulation a coupling of the DC current with the high frequency signal is necessary. This is done by the coaxial bias-tee *ZX85-12G+* from the company *Mini-Circuits* [10]. It has a wideband frequency range from 0.2 to 12000 MHz with an impedance of approximately 50 Ω. An electrical schematic is shown in the manual [10].

The high frequencies are produced by the microwave generator *Rohde + Schwarz SMR 20*. A description of the device can be found in section 5.3.2.

7.3. Characterisation of the DFB-Laser and the DFB-Housing

7.3.1. Analysis of the DFB-Housing's Design

Assembling and Disassembling

The DFB-housing's assembling works as indented. The individual components fit together and the mechanical functionality is given.

Although there are some problems which should be fixed during the next revision process.

- **Adjustment of the optical axis:**
  An adjustment problem occurs due to the DFB-chip's eccentric positioning. This

results in a 0.4 mm mismatch between the optical axis and the diode's geometrical one. Although this mismatch was included in the design, it ultimately complicated the assembling process.

In practice it is hard to align the diode mounting (housing part 3)[2] and the diode aligner (part 1) within the housing. Each single rotation of the diode mounting results in an undefined rotation of the diode aligner. The rotation of the diode mounting is unavoidable during the assembling process.

Additionally the fixing of the large screw (part 6) introduces further undefined rotations of the spacer (part 5), the TEC-element, the diode mounting and the diode aligner.

For a more precise design a fixing mechanism has to be introduced to prevent the rotation of the diode aligner and the diode mounting. The simplest way is to screw the diode aligner in its place and to fix the diode mounting to the diode aligner with some bolts.

- **Potential TEC-element wire damage:**
  The housing (part 7) features two slotted holes for guiding the TEC-element's wires. Close to the TEC to the wire connection point are the wires covered with additional shrink sleeving. This results in a more rigid wire. During the assembling process, the wires have to be bend, which causes strain on the wires. Multiple assembling and disassembling could potentially tear off the wires from the TEC-element.

  A similar problem is introduced by the fixing of the large screw (part 6). This results in a rotation of the TEC-element (as mentioned above) and this shears the wires on the edges of the slotted holes which potentially tears them off.

  So the TEC-element also has to be fixed to prevent rotation.

Thermal Characteristics

The thermal regulation loop worked as indented. After the turn on, the laser diode reached it's temperature in a short time below one minute. Small diode temperature changes, set on the temperature control, were realised within a few seconds. The tested temperatures were all in the range of 15°C to 40°C.

For this functionality the cooling and fixing screw had to be tightened sufficiently. A too loose screw resulted in a bad thermal contact between the elements and the TEC current reached it's maximum value. Additionally the heat sink got too hot to touch, which is not true for a sufficiently tightened screw.

7.3.2. Optical Characterisation

Section 3.3 describes the radiated intensity distribution for a rectangle shaped active zone of a laser diode. Such an active zone forms an elliptical beam profile due to the two angles of divergence. This is observed for the DFB-laser. An aspheric lens (see

---

[2]Compare the part numbers with section 7.2.2

part 7 of the laser housing) is used to collimate the laser light with the help of the Laser Collimation Control (LCC), see figure 6.15. After this collimation the laser beam profile was scanned with the slit-method (slit width: 16 μm), which is explained in section 8.2.5. The observed intensity distribution is shown in figure 7.5. This figure
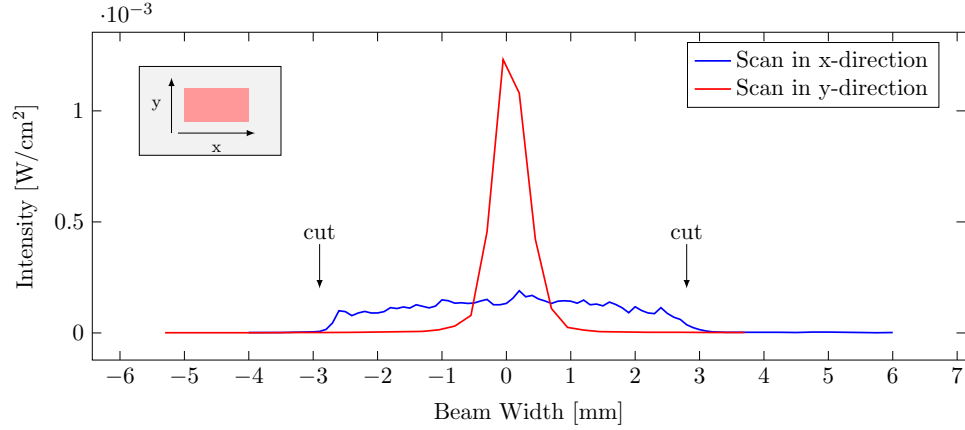

Figure 7.5.: Intensity distribution of the collimated DFB-laser beam. The collimation was achieved with the laser lens, listed at the DFB-housing's part 7. The strongly elliptical beam was scanned parallel (x-direction) and perpendicular (y-direction) to the broad beam width, as shown in the gray box. The broad side is cut by the lens' aperture. The intensity distribution was detected with the slit-method (slit width: 16 μm, see section 8.2.5)

shows an extremely elliptical beam. The scanning direction was parallel (x-direction) and perpendicular (y-direction) to the broad beam width. The narrow beam profile is Gaussian shaped with the Gaussian fitted beam width of (1.0 ± 0.2) mm, while the broad beam width is cut by the len's aperture of ≈ 5 mm. A Gaussian fit showed a broad beam width of (7.2 ± 0.6) mm. With the Gaussian fitted beam widths and the collimation lens' focal length of $f = 6.24$ mm the angles of divergences are calculated to be $\theta_{narrow} \approx 5°$ and $\theta_{broad} \approx 50°$.

In order to collimate the entire beam, without cutting the edges, a NA of ≈ 0.6 is estimated with the equation (4.12). In order to form a symmetrical beam an anamorphic prism pair could be used.

The broad beam profile also complicates the coupling into an optical fibre. Just a small amount of its initial intensity was guided through a MMF.

7.3.3. Electrical Characterisation

In figure 7.6 the optical power as a function of the laser current is shown, the threshold current of 25 mA corresponds to the datasheet [41].
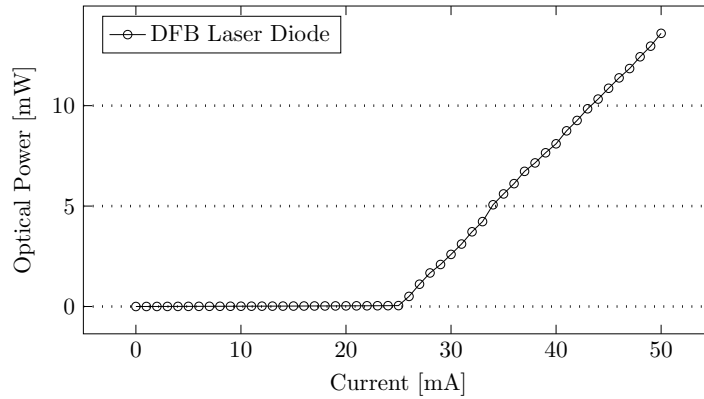
Figure 7.6.: Optical power as a function of the laser current of the DFB-laser *Toptica # LD-0795-0020-DFB-1* [41]. The threshold current is 25 mA.

7.3.4. Electrostatic Discharge (ESD) -Damage

All the different kinds of laser diodes are extremely sensitive[3] to electro static discharges ESDs. Therefore special precautions have to be taken in the laboratory in order to minimise the risk of a devices' ESD-damage.

ESD events occur when high voltages of several kVs affect the diodes in short time intervals, in the ns to µs regime. Besides the ESD, there is a so called electrical overstress (EOS) scenario. This occurs at much lower levels of voltage but at much longer time intervals [47].

During the characterisation of the DFB-laser, the laser-diode for the DFB-housing was destroyed due an electrostatic discharge (ESD) resulted by a parasitic grounding loop. This DFB-laser is mounted within a TO9 diode package, for which the DFB-laser housing was designed. DFB-lasers in the wavelength range of 795 nm are normally not produced in such packages, the used laser diode was a custom-made product by the company *Toptica*. In the moment of writing there were no DFB-lasers in the same package available.

7.3.5. Outlook for the DFB-Laser Characterisation

Further investigations of the DFB-laser should observe the laser light's frequency stability and the modulation capabilities. Especially the side band amplitudes of the - with 3.4 GHz frequency modulated - laser light is of special interest.

---

[3]The Human Body Model (HBM) simulates the electrostatic discharge (ESD) damage of electronic devices introduced by the human body, where damages caused by voltages as low as 50 V are common [47].

8. Characterisation of Cells with different Ne-pressure

In section 2.4.2 the influence of the buffer gas pressure on the CPT-resonance frequency and the CPT-linewidth is described. In order to investigate which pressure is necessary to find the most suitable parameters for the CDSM-sensor - CPT-linewidth, CPT-resonance amplitude and CPT-resonance frequency, see section 6.1.1 - different cells with different Ne-pressures are tested.

8.1. Ne-Buffer Gas Cells

The used cylindrical cells are:

Photonics Technologies isotopically pure ^{87}Rb
Ne buffer gas pressures:
15, 30, 60, 80, 100, 120 Torr
dimensions: ø 12.7 mm length: 28.8 mm

For each pressure, two cells are tested. The cell's buffer gas pressures are not exact due to its process of manufacturing. Availability of several cells allow to select the best suited for the sensor.
The individual cells nomenclature is:

X $NE - Sp$ N

Where X is the nominal pressure in Torr and N is the cell's number 1 or 2. This naming scheme is adopted from the manufacturer's cell markings.

8.2. Experimental Conditions

For the cell characterisation the experimental setup from section 6.1.2 was used. The VCSEL beam was collimated with the LCC. The lock-in amplifier's reference frequency was set to 30120 Hz and the reference amplitude of the internal oscillator to 0.722 V_{eff}. The reference phase was individually adopted. For each cell, the 0-0-CPT-resonances[1] were recorded for different laser light intensities. The experiment was performed and recorded with the LabView program for sweeping (section A.1) and analysed with the Analysis-LabView program (section A.2). The CPT-linewidth was measured with two

---

[1]See section 2.4.1

cursors, which were placed on the plot of the Analysis tool. With the same method the linewidth measurement uncertainty and the CPT-resonance amplitude are determined. For each CPT-resonance scan the parameters of table 8.1 are recorded.

Table 8.1.: Recorded parameters for each CPT-resonance scan.

Symbol	Unity	Explanation	Section
P_{in}	[μW]	cell's incident optical power	8.3
P_{out}	[μW]	cell's transmitted optical power	8.3
I_{laser}	[mA]	laser current	3.5
T_{laser}	[mA]	laser temperature	3.5
T_{before}	[Ω]	cell temperature before sweep	8.2.3
T_{after}	[Ω]	cell temperature after sweep	8.2.3
W_{CPT}	[Hz]	CPT-resonance linewidth	6.1.1
ΔW_{CPT}	[Hz]	uncertainty of W_{CPT}	8.2
A_{max}	[μV]	CPT-resonance amplitude maximum	6.1.1
A_{min}	[μV]	CPT-resonance amplitude minimum	6.1.1
ν_{CPT}	[Hz]	CPT-resonance frequency	6.1.1

8.2.1. Microwave Generator Frequency

For the CPT-resonance detection the microwave generator's frequency ν_{GHz} is set to half of the hyperfine splitting frequency $\frac{1}{2}\nu_{HFS} = 3.417$ GHz of the ground state in order to excite the transition from $5\ ^2S_{1/2}\ F = 1$ to the first excited state $5\ ^2P_{1/2}\ F = 1, 2$ with the upper side band $\nu_L + \nu_{GHz}$ and the transition from $5\ ^2S_{1/2}\ F = 2$ to the first excited state $5\ ^2P_{1/2}\ F = 1, 2$ with the lower side band $\nu_L - \nu_{GHz}$, as shown in section 6.1.1. Every frequency change $\Delta\nu_{GHz}$ of the microwave generator results in twice the frequency gap change $2 \cdot \Delta\nu_{GHz}$ between the upper and lower side band. Therefore every with the lock-in amplifier recorded frequency has to be doubled to obtain the actual frequency value of the spectral feature.
All frequencies, which are presented in this chapter always refer to the microwave generator's displayed frequency.

8.2.2. Applied Magnetic Field

In order to isolate the 0-0-CPT-resonance a magnetic field is applied, see section 6.1.1. To calculate the magnetic field flux density B, which is produced by the solenoid coil of the experimental setup in section 6.1.2, the equation

$$B = \mu_0 I \frac{n}{l} \tag{8.1}$$

is used [11]. The magnetic flux density within a solenoid coil is not uniform. At the coil's end, the flux density drops to half of the middles one. Although, by placing the

coil within the µ-metal shielding, the magnetic field lines are forced to enter the metal end caps of the cylindrical µ-metal shielding almost perpendicularly. This is due to the continuity condition for the B-field at an abrupt transition between the permeability of air and the high µ-metal's permeability [35].

For all cell characterisation the same magnetic flux density of

$$B = (7.9 \pm 0.2) \; \mu T$$

was applied to the cells. This value is calculated from equation (8.1) with the coil's current of $I = 6.0 \pm 0.1$ mA, the coil's length $l = 75$ mm and its number of turns $n = 79$. The magnetic flux density influences the 0-0-CPT-resonance frequency only in second order perturbation, so a only small shift is introduced. With the magnetic field of $B = (7.9 \pm 0.2) \; \mu T$ and $\Delta\nu(B) = 575.14 \cdot 10^8 \cdot B^2$ (see equation (2.38)), the 0-0-CPT-resonance frequency is shifted by $\Delta\nu = (3.6 \pm 0.1)$ Hz.

At the CPT-resonance frequencies, which are listed in this chapter, this frequency shift is not corrected .

8.2.3. Cell's Temperature

The cells were held at a constant temperature by a cell heating in order to minimize the Rb-vapour temperature influence on the CPT-resonance frequency. This influence is described in [17].

For the experiment, the cells were heated up to approximately 45°C. To avoid the unwanted influence of the cell heating coil the (heating) current was turned off and the CPT-resonance was scanned by the LabView program. With this LabView automation it is possible to probe a small frequency range (a few hundred Hz) around the CPT-resonance frequency in a time below 40 s with a resolution of 2 Hz. This scan-speed allows to scan the resonance while the cell's Pt1000 temperature[2] is in the range between 36.0°C and 35.4°C due to the cooling down. **All CPT-resonance scans were recorded at the cell's temperature of (35.7 ±0.3)°C.**

8.2.4. Rb-Coating and Cell Alignment

For the characterisation of the CPT-resonances, the intensity of the laser beam which interacts with the atoms of the Rb-vapour, is of interest. Therefore the incident optical power P_{in} is measured. This incident light intensity is reduced by Rb absorption and additional losses. These losses are due to the cell's misalignment and due to cell's surface reflections. There are regular approximately 4% reflection on the glass surfaces which can be reduced by a anti-reflex coating. Much higher reflections are introduced by condensed Rb-vapour on the cell's surfaces. This results in a highly reflecting, but inhomogeneous coating. In table 8.3 the amount of transmitted optical power P_{out} in relation to the incident optical power P_{in} is listed for each Rb-cell. The amount of transmitted power varies strongly between the cells. The reflecting Rb-coating is

---

[2]Platinum resistance temperature sensors: temperature/resistance relationships from the *DIN EN 60751* standard

Table 8.2.: Amount (P_{out}/P_{in}) of the optical power which as transmitted through the cell.

Cell	Amount	Cell	Amount	Cell	Amount
15NE-Sp1	0.60	60NE-Sp1	0.64	100NE-Sp1	0.47
15NE-Sp2	0.44	60NE-Sp2	0.61	100NE-Sp2	0.55
30NE-Sp1	0.60	80NE-Sp1	0.49	120NE-Sp1	0.53
30NE-Sp2	0.47	80NE-Sp2	0.66	120NE-Sp2	0.50

inhomogeneously spread on the cell's surfaces. Due to the experimental setup, where the cells are placed in a heating, put in the solenoid coil and encased by the μ-metal shielding, the exact orientation of the cells relative to the laser beam is not controllable. Therefore, for every new experiment, even for the same cell, the cell's alignment will be different and, in fact, the P_{out}/P_{in}-ratio will change. In section 8.3 the influence of the cell's alignment on the CPT-resonances is investigated.

Due to the random nature of these additional losses the choice of the incident optical power P_{in} for the CPT-resonance analysis is influenced by a random uncertainty. Therefore the transmitted optical power P_{out} - directly measured by the photo detector - is used for plotting and for the calculations in the analysis sections 8.3 and 8.4. With P_{out} the potential reflections on the cell's light source facing surface are excluded as a source of losses, but the potential reflections on the detector facing surface are still present as a source of losses.

8.2.5. Laser Beam Profile and Laser Beam Intensity

In experiments the investigation of the beam's intensity profile of the probing laser light is necessary to characterise the beam parameters' influence on the measurement. This is e.g. shown in section 6.3, where the beam's spot size influences the CPT-resonance linewidth. The section 4.1.4 about MMFs and SMFs features beam profiles. The beam's profile is also needed to calculate the light's intensity.

An experiment has to be performed to determine the laser beam's profile. A power meter[3] is covered with a slit and mounted on a moveable slider. The slit is positioned perpendicular to the slider's moving direction. The silt's area is

$$0.016 \ mm \cdot 11 \ mm = 0.176 \ mm^2.$$

The slider is moved with a screw. This screw allows to shift the power meter and so the slit with the precision of 1 μm. By shifting the slit through the entire beam, an optical power distribution as a function of the moved slit distance can be recorded. Each of the so recorded optical power data points is divided by the slit's area to calculate the (slit's area averaged) laser intensity as a function of the moved slit distance.

This is a one-dimensional scan of the beam profile. If the beam is TEM$_{00}$ the beam is

---

[3]Standard laboratory power meter: Newport Optical Power Meter 1830-C

symmetrical and a one-dimensional scan is sufficient to characterise the beam's profile. In the case of the DFB-laser the rotational symmetry is not given, so two scans are needed in order to characterise the DFB's profile, see figure 7.5.

Ultimately, the beam's diameter is needed to calculate the entire beam's intensity. The section 4.1 describes Gaussian beams. For an ideal TEM_{00} 86.5% of the beam power lies within a circle. At the radius of this circle the intensity drops to $1/e^2 = 13.5\%$ of the maximums intensity. This fact is used to calculate the laser beam's intensity. The beam intensity profile, which is recorded with the moveable slit, is fitted with an Gaussian function in order to determine this $1/e^2$-radius. Further it is assumed that the entire light intensity is distributed equally within this $1/e^2$-circle. So the entire optical beam power divided through the circle's area in order to calculate the beam's intensity. For the cell characterisation the fitted beam's diameter was determined to be (5.9 ± 0.3) mm.

8.3. Analysis of the Cell's Alignment

In order to investigate the influence of the cell alignment and the inhomogeneous Rb coating on a single cell characterisation the *60NE-Sp1* cell was characterised four times. For each characterisation the entire cell-setup (heating, coil and in μ-metal shielding) was reassembled. The four characterisations are compared to get an estimation of the variances introduced by the Rb-coating and the cell's alignment. The P_{out}/P_{in}-ratios are M1: 0.36, M2: 0.37, M3 0.53 and M4: 0.58.

In figure 8.2 the observed data of the four characterisations (M1 - M4) is displayed. In (a) the CPT-resonance linewidth W_0 is plotted as a function of the intensity. A linear behaviour - which is predicted by (2.18) - is observed. The plots are fitted linearly and the means of the fit parameters are used to calculate the power broadening and to estimate the ground state coherence decay rate[4] Γ. The values are listed in table 8.3. The errors of all the fit parameters (in this chapter) are determined with a 2σ confidence interval.

In [39] the CPT-resonance amplitude A as a function of intensity is described in two regimes. A quadratic rise for low intensities and a linear rise for higher intensities. The amplitude dependence in (b) is linear, no quadratic behaviour is observable from this data. Therefore linear fits are used to describe the CPT-resonance amplitude dependence. The mean increase of the amplitude is listed in table 8.3.

Figure (c) shows the CPT-resonance frequency as a function of intensity. Despite of the large errorbars, a slight increase of the resonance frequency is seen. For an ideal three-level system, there should not be any shift of the resonance frequency (light shift) with increasing intensity. But for real systems, the "dark state" becomes not completely dark and the light can excite some atoms [39] and so the resonance frequency is shifted due to the dynamic (ac) *Stark* effect [49]. The light shift is proportional to the intensity. Therefore linear fits are used to estimate the light shift. The mean extrapolated mean value of the CPT-resonance frequency at zero intensity and the mean light shift is listed

---

[4]See equation (2.18): $W_0(g^2 = 0) \approx \Gamma$

in table 8.3.

Close to the CPT-resonance frequency the dispersive signal, which is detected with the lock-in amplifier (see section 6.1.1) can be approximated linearly. For this linear function its slope's error is assumed to be the same as the slope's error of the amplitude/linewidth-ratio $\Delta A/W_0$ of figure 8.1. With the error $\Delta A/W_0$ the error of the CPT-resonance frequency is approximated.

In figure 8.1 the amplitude/linewidth ratio A/W_0 is plotted as a function of intensity. From the linear fits the mean slope is listed in table 8.3.

In table 8.3 the for all four measurements evaluated parameters are listed, combined with their estimated errors. These errors estimate the influence of the cell's alignment and the Rb-coating on the cell's surfaces.

Table 8.3.: Characterisation of the *60NE-Sp1* cell for four individual measurements. The listed values are the means of the linear fit parameters from the figures 8.2(a)-(c) and 8.5.

|	
power broadening	(10 ± 1) Hz cm^2 µW^{-1}
ground state coherence decay rate Γ	(45 ± 5) Hz
slope of the CPT-resonance amplitude A	(160 ± 9) µV cm^2 µW^{-1}
CPT-resonance frequency ν_0	(3417347491.4 ± 0.8) Hz
light shift	(1.7 ± 0.3) Hz cm^2 µW^{-1}
slope of A/W_0	(1.1 ± 0.1) µV cm^2 Hz^{-1} µW^{-1}
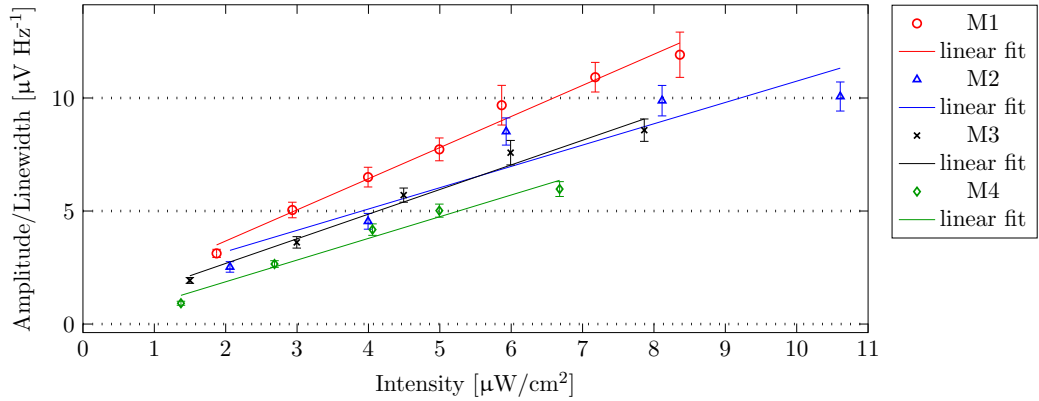
Figure 8.1.: Amplitude/Linewidth-ratio A/W_0 as a function of intensity. The mean slope is (1.1 ± 0.1) µV cm^2 Hz^{-1}.
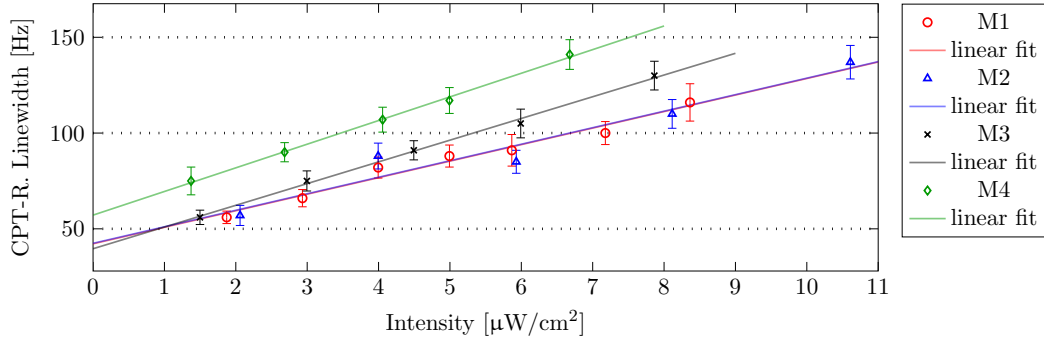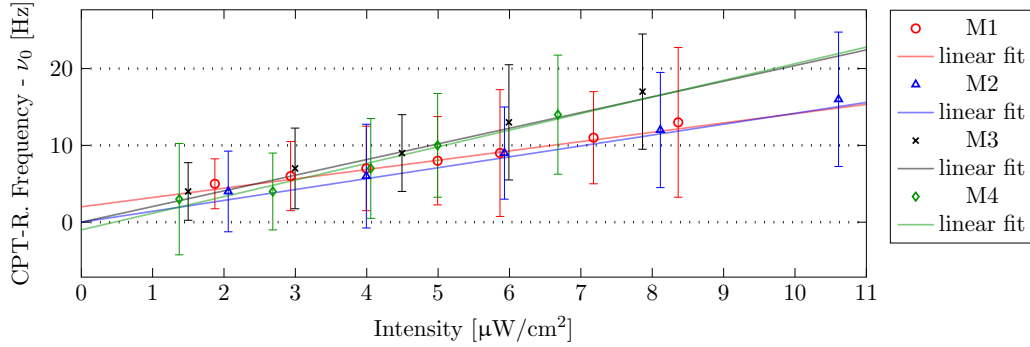
(a) CPT-resonance linewidth W_0 as a function of intensity. The power broadening is the slope of this function. The mean of the four fitted slopes is (10 ± 1) Hz cm^2 µW^{-1}. The ground state coherence decay rate Γ is the extrapolated linewidth at zero intensity. The mean of the four fits is (45 ± 5) Hz.
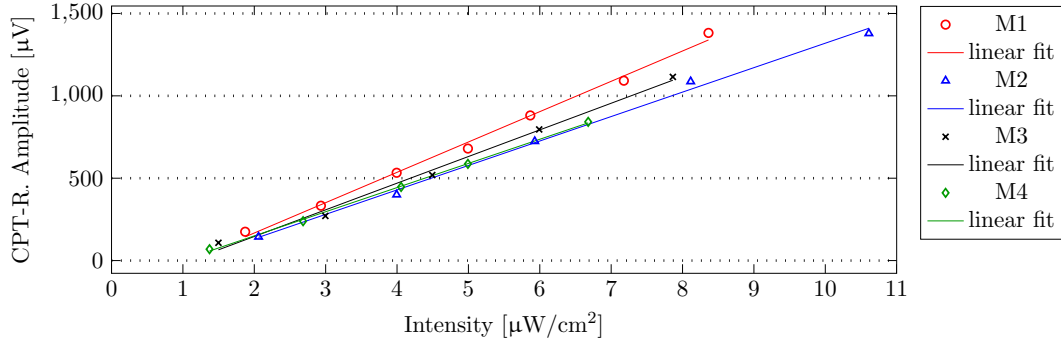
(b) CPT-resonance amplitude A as a function of intensity. The errorbars are too small to be seen. The mean of the fitted slope is (160 ± 9) µV cm^2 µW^{-1}.

(c) CPT-resonance frequency - ν_0 as a function of intensity. $\nu_0 = 3417347491$ Hz is the mean of the extrapolated linear fits at zero intensity. The mean fitted slope is the light shift with (1.7 ± 0.3) Hz cm^2 µW^{-1}

Figure 8.2.: Four separate 0-0-CPT-resonance characterisations of the Rb-cell *60NE-Sp1*.

8.4. CPT-Resonances as a Function of Ne-Pressure

Each cell from table 8.3 was characterised with the same approach as the *60NE-Sp1* cell, but only one measurement was performed for each other cell. In order to estimate the Ne-pressure influence on the CPT-resonance, the same fit parameters are determined. These fit parameters are used to draw the figures 8.3(a)(b), 8.4 and 8.5.

Due to the process of manufacturing, the Ne pressure does not match the nominal value. This fact is clearly visible in figure 8.4. For the nominal Ne-pressures of 30 Torr and 100 Torr the CPT-resonance frequencies of the two characterised cells are shifted. These large shifts can not be explained with the cell's misalignment (estimated error is < 1 Hz, see table 8.3) and the high reflective Rb-coating. These shifts are introduced by the "wrong" nominal pressure. Especially for the 100 Torr cells, the CPT-resonance frequency (of the upper dot) suggests that the Ne-pressure is closer to 120 Torr. Therefore this data-point was excluded from the linear fit.

The influence of the cell's alignment can be smaller than the data variation introduced by the different cell pressures which are caused by the manufacturing process.

The overall smallest linewidth was measured for the *100NE-Sp1* of

$$(40 \pm 4) \ Hz$$

at an intensity of $(1.5 \pm 0.1) \ \mu\text{W/cm}^2$.

8.4.1. Power Broadening and Ground State Coherence Decay Rate

In the previous section the power broadening and the ground state decay rate Γ were determined for the *60NE-Sp1* cell. The figure plot:Cell:all:Ground-Power(b) shows the ground state coherence decay rate Γ as a function of the Ne buffer gas pressure. The larger pressure leads to a decrease of the linewidth due to the longer interaction times of the Rb-atoms within the laser beam. For even larger pressures the linewidth increases due higher collision broadening [49]. Inbetween these two regions a region with constant linewidth (between 80 and 100 Torr) is established.

In figure plot:Cell:all:Ground-Power(a) the power broadening as a function of Ne-pressure is displayed. In this plot, there is no significant trend visible. The mean power broadening for all cells is (10.6 ± 0.6) Hz cm/μW.

8.4.2. Blue Shift

The influence of buffer gas on the CPT-resonance frequency is described in section 2.4.2. The equation 2.39 describes the resonance shift as a function of the buffer gas pressure and the temperature. For the cell characterisation the cell temperature was held constant, see section 8.2.3. Therefore the CPT-resonance frequency is shifted linearly with increasing Ne-pressure. This is observed in figure 8.4. This shift of the CPT-resonance frequency is called blue shift.

By the higher buffer gas pressure the Van-der-Waals and the exchange interaction of the Rb-atoms with the Ne-atoms during the atomic scattering is increased. The electrons
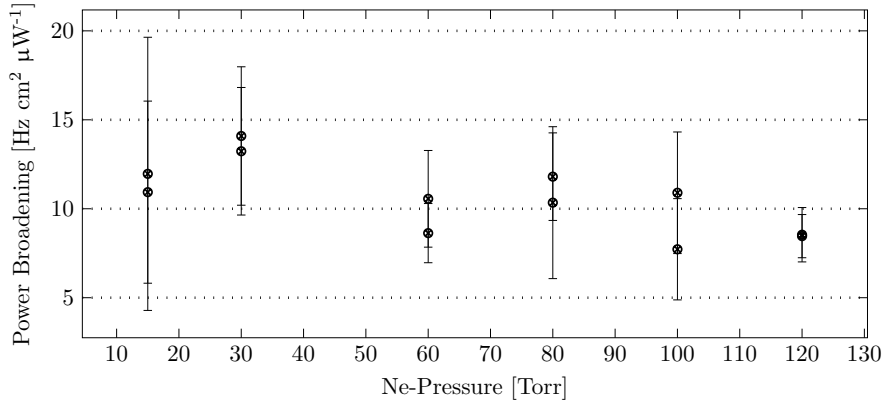
(a) Power broadening as a function of the cell's Ne-pressure. The mean power broadening for all cells is (10.6 ± 0.6) Hz cm/µW.
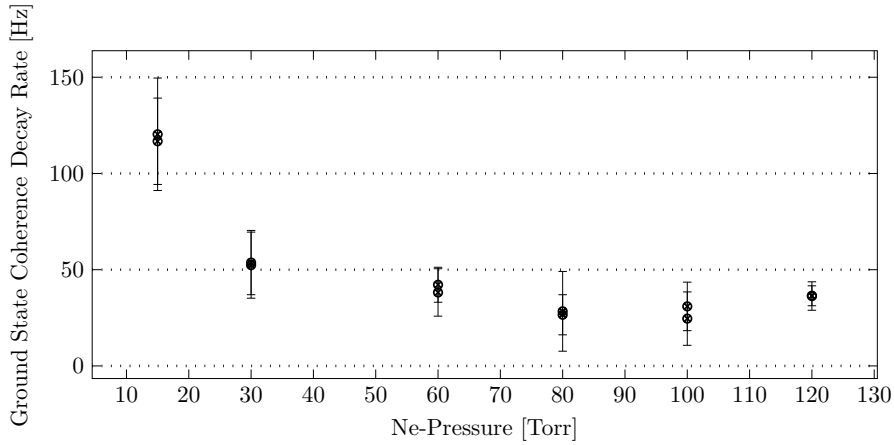
(b) Ground state coherence decay rate Γ is a function of Ne-pressure. In the region between 80 and 100 Torr, there is the lowest Γ.

Figure 8.3.: The power broadening and the ground state coherence decay rate Γ as a function of nominal Ne-pressure.

of the Rb-atom are pushed closer to their atomic nucleus due to the repulsing forces of the increased interactions. This leads to a larger Rb-ground state hyperfine splitting and therefore to a rise of the CPT-resonance frequency [28]. The linear fit's slope determines the blue shift $\beta = (87 \pm 7)$ Hz Torr^{-1}. The buffer gas free cell's CPT-resonance frequency is determined to be $\nu_0 = (3.4173417 \pm 5 \cdot 10^{-7})$ GHz. By dividing the blue shift β through the resonance frequency ν_0, $\beta/\nu_0 = (26 \pm 2) \cdot 10^{-9}$ Torr^{-1} is achieved. The literature value [48] is $\beta/\nu_0 \approx 50$ to $60 \cdot 10^{-9}$ Torr^{-1} depending on the cell temperature and the seal temperature[5].
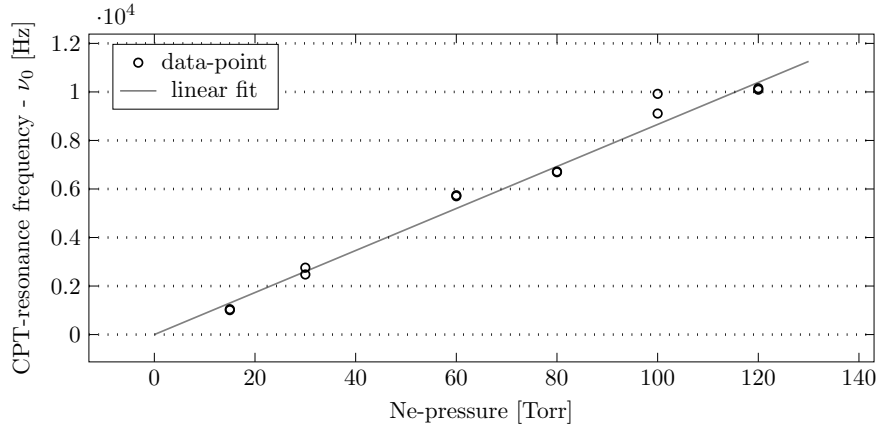
Figure 8.4.: CPT-resonance frequency - ν_0 as a function of the nominal Ne-pressure. The increase of resonance frequency is called blue shift $\beta = (87 \pm 7)$ Hz Torr^{-1}. The errorbars are too small be drawn. The buffer gas less CPT-resonance frequency is $\nu_0 = (3.4173417 \pm 5 \cdot 10^{-7})$ GHz.

8.4.3. Amplitude/Linewidth-Ratio

The ratio of the amplitude to the linewidth A/W_0 determines the sensitivity of the CDSM, see section 6.1.1. The higher this ratio, the small magnetic field changes are detectable. In figure 8.5 the interpolated ratio is plotted for the intensity of 5 μW/cm^2. The variance between two cells of the same nominal Ne-pressure can be as large as the variances of cells with different nominal Ne-pressure. This is visible in figure 8.4 for the 100 Torr cells, where a large pressure difference is known from the CPT-resonance frequency. Also for 30 Torr cell is a split
Although these variances and the large errorbar, the highest A/W_0-ratio is identifiable in the range between 80 to 100 Torr.

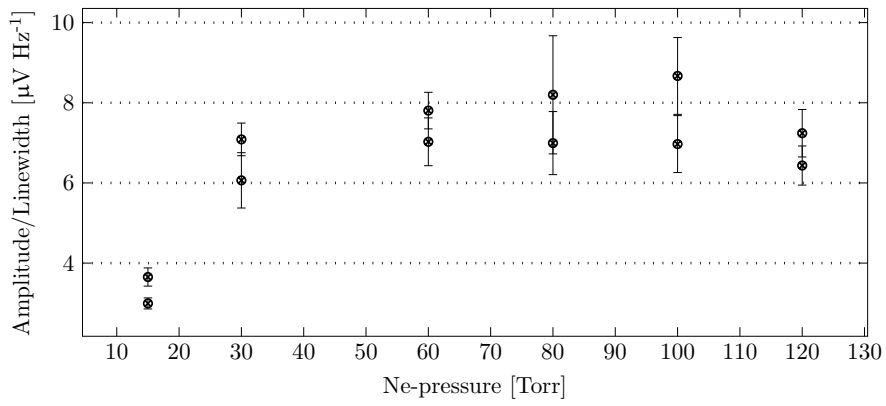[5]At which temperature the glass cell was sealed during the manufacturing process, this influences the Ne-pressure.

Figure 8.5.: CPT-Amplitude/Linewidth-ratio A/W_0 as a function of nominal Ne-pressure for the interpolated intensity of 5 μW/cm^2. The highest A/W_0-ratio can be found for the pressures 80 to 100 Torr.

9. Conclusion

The improvements of the CPT-resonance setup are the measurement automation, the LCC system and the design of a custom DFB-laser housing.

The measurement automation with LabView programs allows to remote control the microwave generator *Rohde & Schwarz SMR20* and the lock-in amplifier *Stanford Research Systems SR830*. A custom LabView analysis-tool simplifies the evaluation of the recorded data. The LabView programs proved their usability at the Ne-buffer gas cell's pressure characterisation. This characterisation showed that Ne-buffer gas pressures in the range of 80 to 100 Torr result in the highest amplitude/linewidth-ratio. This pressure range is the most suitable for the design of the CDSM sensor. The Ne-pressure deviations from its nominal values, due to the process of manufacturing, influence the data more than variations, introduced by cell's misalignments and a potential inhomogeneous Rb-coating on cell's surfaces.

A Laser Collimation Control (LCC) system was designed to evaluate the laser beam's collimation in order to minimise the CPT-resonance linewidth's power broadening introduced by an uncollimated laser beam. The Laser Collimation Control (LCC) system is used for the CDSM assembling and for the collimation of laser lenses and fibre couplers in the laboratory.

The designed DFB-laser housing proved its mechanical and thermal functionality and allowed to perform a basic electrical and optical characterisation of the DFB-laser diode. The optical characterisation showed a strongly elliptical laser beam profile. Therefore the currently used lens is not suitable for the collimation of the laser beam. A different optical system is necessary to produce a circular beam profile, e.g. an anamorphic prism pair. The DFB-laser modulation capability was not analysed and a further investigation is of interest.

A. Appendices

A.1. LabView Automation

Table A.1.: List of LabView SubVIs. The symbols are taken from LabView SubVIs The SubVIs functionality is described.

Nr	Symbol	Name and Functionality
1	FIND INIT ADDRES	**findingaddress(SubVI)** Scans the ports of the GPIB to find the *SR830* and *SMR20* and displays the address, which is necessary for communication.
2	INIT DEV	**init-devices(SubVi)** Initialises the GPIB-interface for later port scanning.
3	SR830 SNAP CONFIG	**SR830-config-snap(SubVI)** Configures the *SR830* with the measurement parameters: sensitivity, reference phase, reference amplitude, reference frequency, time constant, low pass filter slope, reserve mode and notch filter. This used parameters are explained in section 5.3.1.
4	SR830 SNAP MEAS	**SR830-measure-snap(SubVI)** Reads out a certain number of data from the lock-in with the "SNAP"-command. The waiting time between two readout processes is determined by the set time variable divided by the number of readouts. From all the so received data, the mean is calculated.
5	SR830 CONFIG DATA	**SR830-config-data-sweep(SubVI)** Converts the configuration information of the *SR830* into a string in order to save it to the measurement data file.
6	SMR20 CONFIG DATA	**SMR20-config-data-sweep(SubVI)** Converts the configuration information of the *SMR20* into a string in order to save it to the measurement data file.
7	SMR20 SINGLE CONFIG	**SMR20-config-singlefreq(SubVI)** Sets the **SMR20** to FM-mode and to a constant frequency. This is used for the monitoring mode (section 6.2.3). The external reference is activated for the stabilisation with an atomic clock.

8	SMR20 SWEEP CONFIG	**SMR20-config-sweep(SubVI)** Configures the sweep mode of the *SMR20*, which is triggered via the "TRIG"-command. The set parameters are: start frequency, step frequency and stop frequency. The FM-mode is activated as well as the external reference the stabilisation with an atomic clock.
9	SR830 SMR20 SCAN	**single-scan-SR830-SMR20-snap(SubVI)** This is the central sweep mode, which is explained in section 6.2.3. It performs a frequency sweep with a simultaneous data recording. The data is saved to the measurement data file. It uses the SubVIs number 3,4,5,6 and 8. A schematic drawing of its functionality is shown in figure 6.8 on page 51.
10	SR830 SMR20 LIVE	**live-mode-SR830-SMR20-snap(SubVI)** This is the monitoring mode, which is explained in section 6.2.3. It monitors the data from the SR830 and allows to change the configuration parameters of the SMR20 and the SR830. It used the SubVIs number 3,4 and 7. The acquired data is not saved.
11	SMR20 SR830 FILE	**data-file-SR830-SMR20(SubVI)** Collects the data strings from SubVI numbers 5 and 6, combines it with the annotation window (see figure A.1) and writes it at the beginning of each measurement data file.
12	GET FILE PATH	**get-file-from-project-folder(SubVI)** Constructs a data file path and file name for the specific project folder. The measurement data file name includes the date and time stamp of the sweep's start for unique file names.
13	LOG-F OPEN CREATE	**LOG-file-create-or-open(SubVI)** Creates a log-file for each day of experiments. In this log-file all device parameters and annotations of all, this day, performed experiments are saved, but not the data of the X and Y of the lock-in amplifier itself.
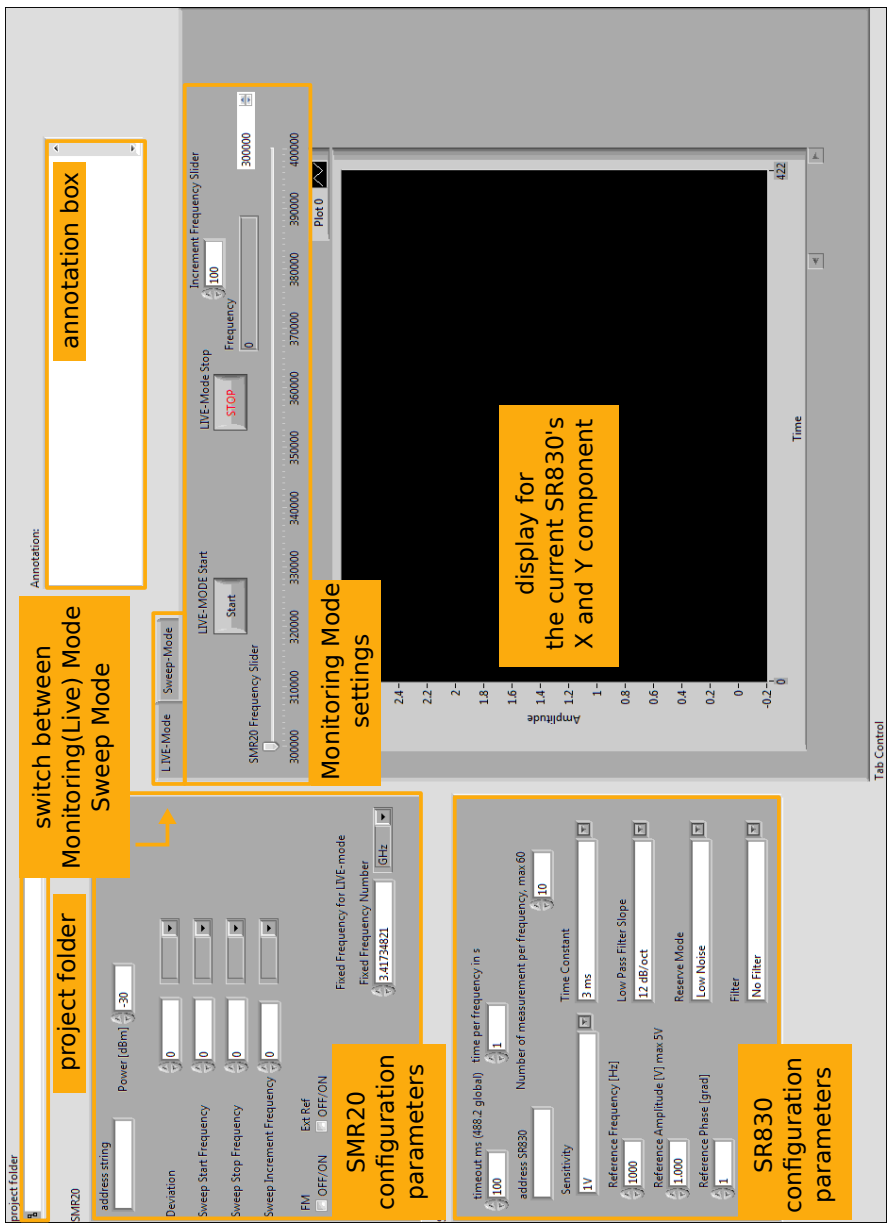
Figure A.1.: Integration of the Central Sweep Mode and the Monitoring Mode in one GUI.
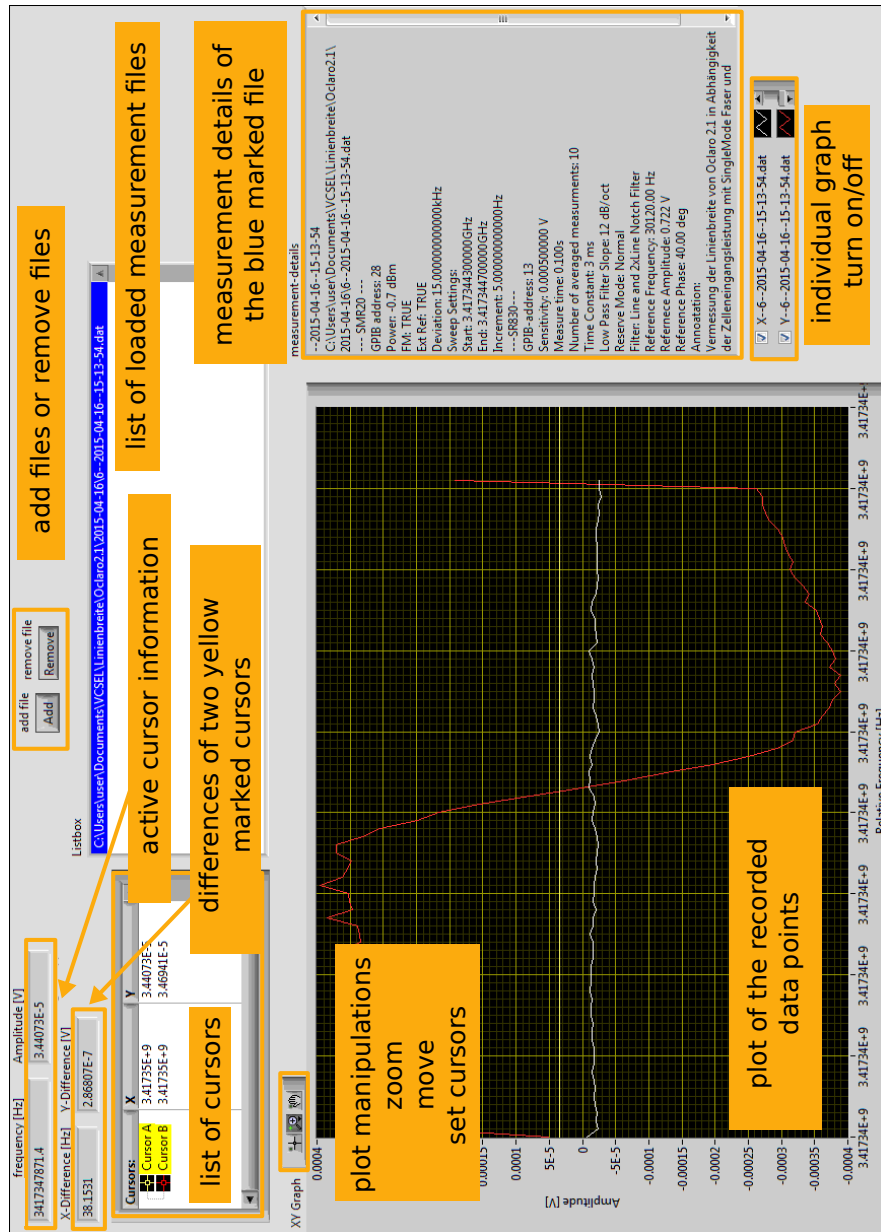
Figure A.2.: LabView Analysis Tool

A.2. Mechanical Drawings

A.2.1. DFB-Laser Diode Housing
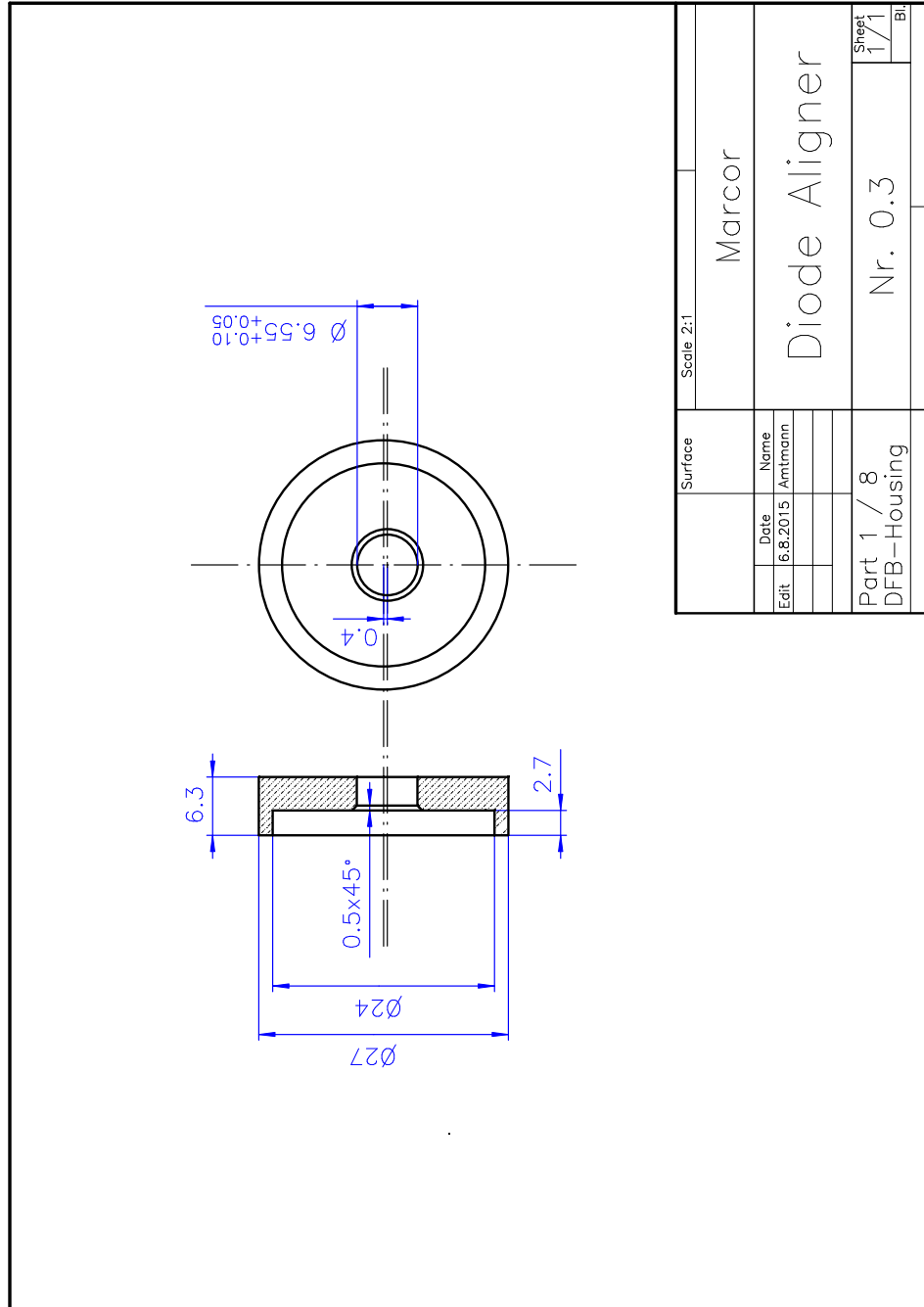
Figure A.3.: The diode aligner is part 1 of the DFB-laser housing.
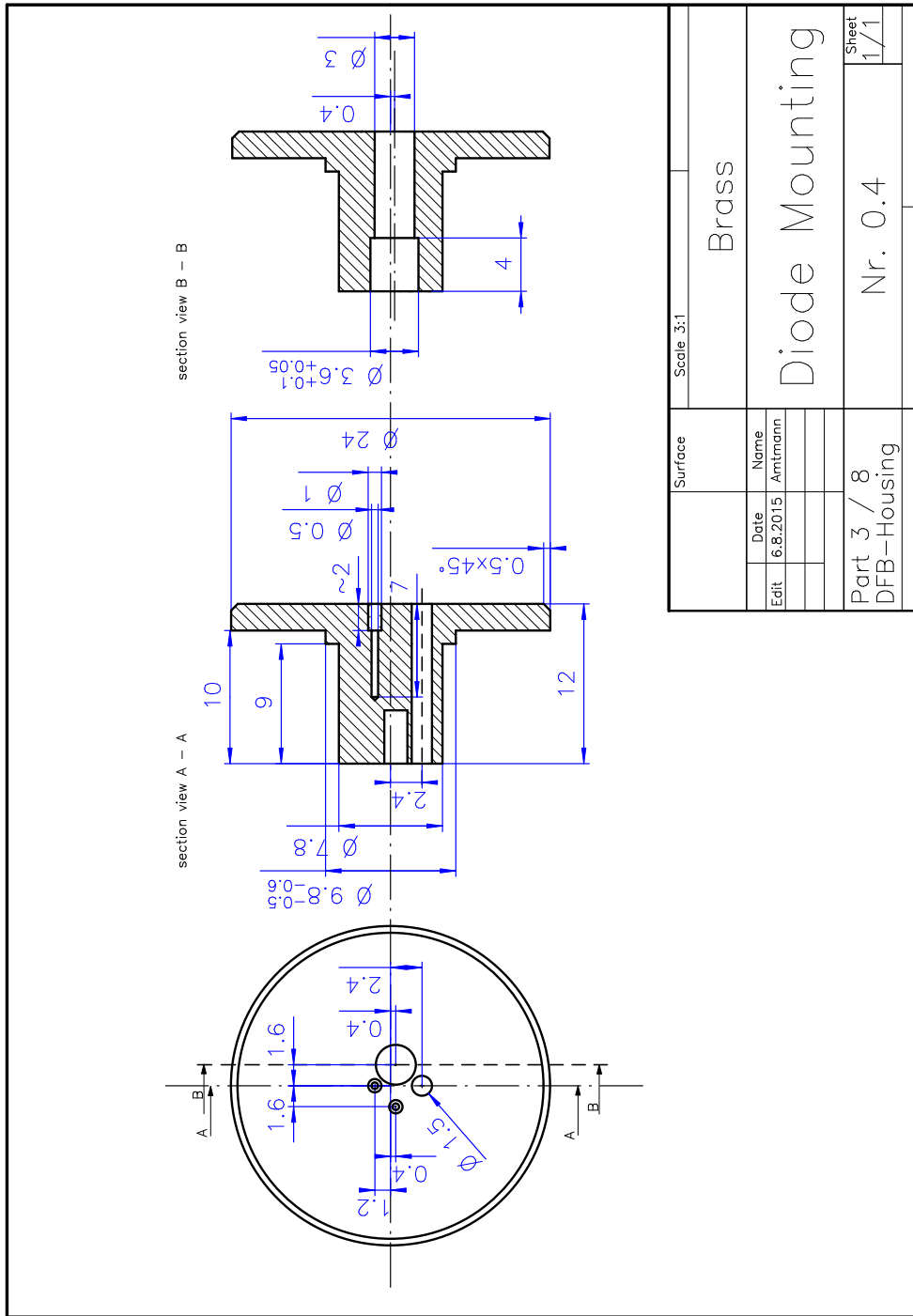
Figure A.4.: The diode mounting is part 3 of the DFB-laser housing.
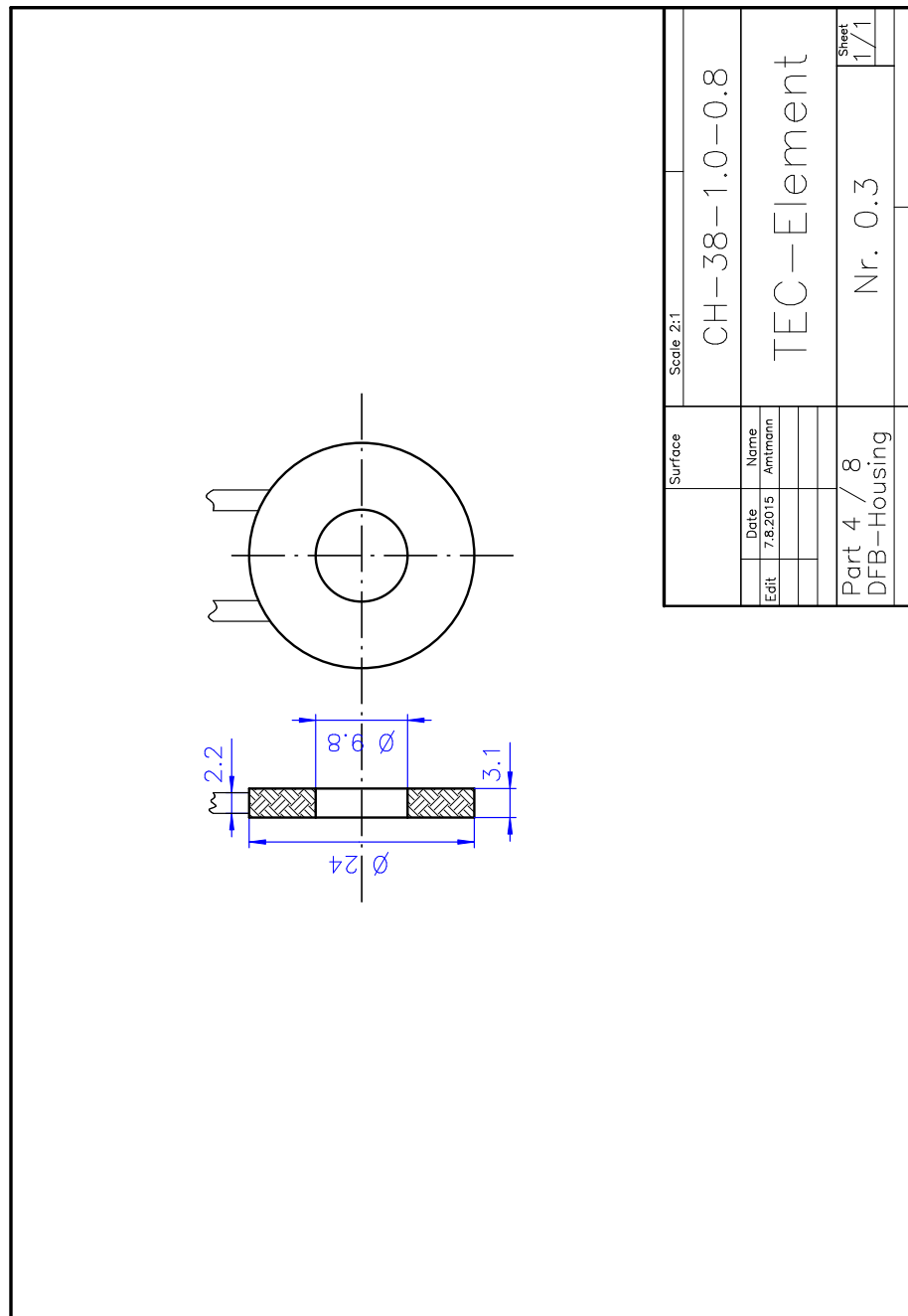
Figure A.5.: The TEC-element is part 4 of the DFB-laser housing. The dimensions are taken from the actual object, not from the data sheet.
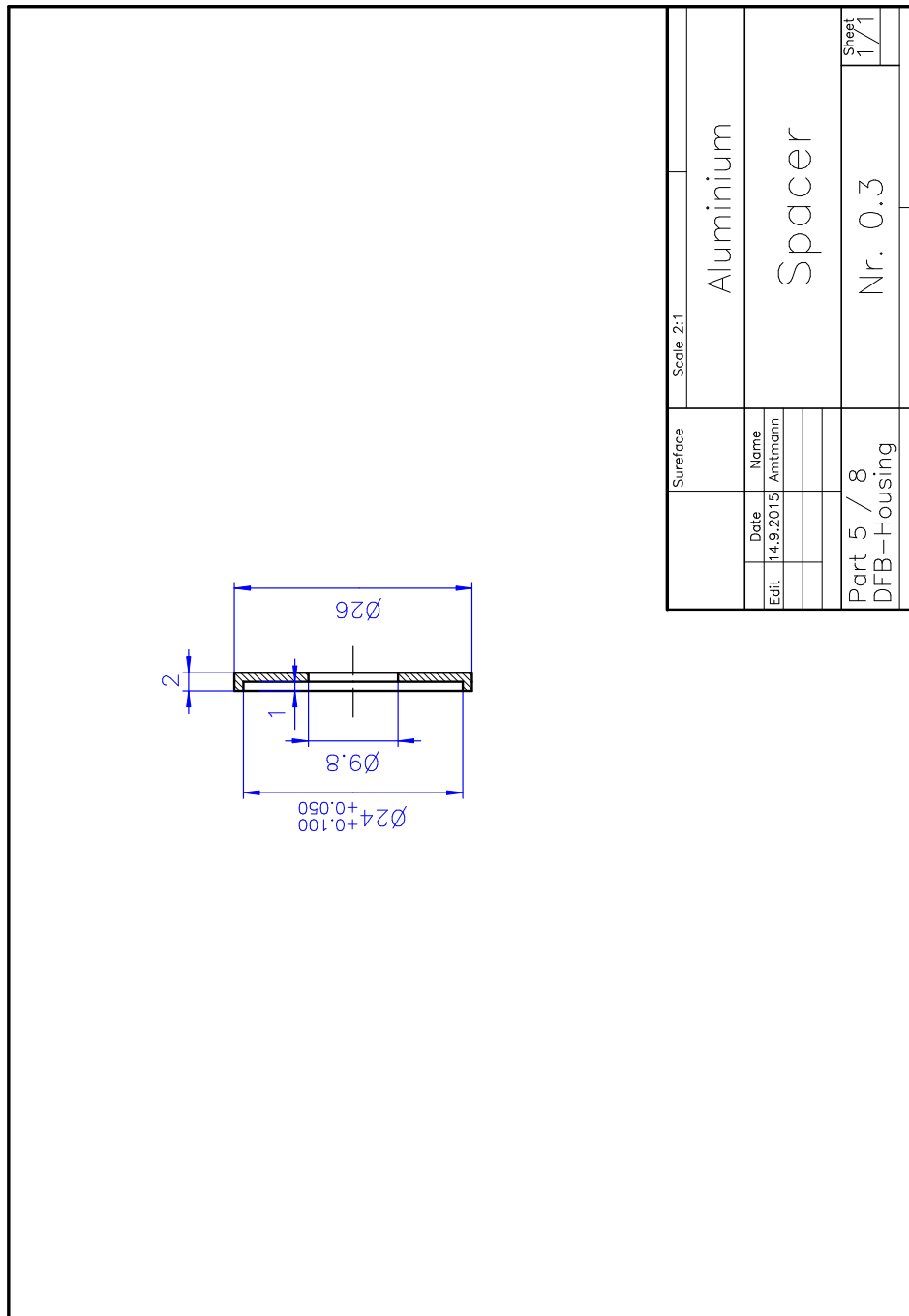
Figure A.6.: The aluminium spacer is part 5 of the DFB-laser housing.
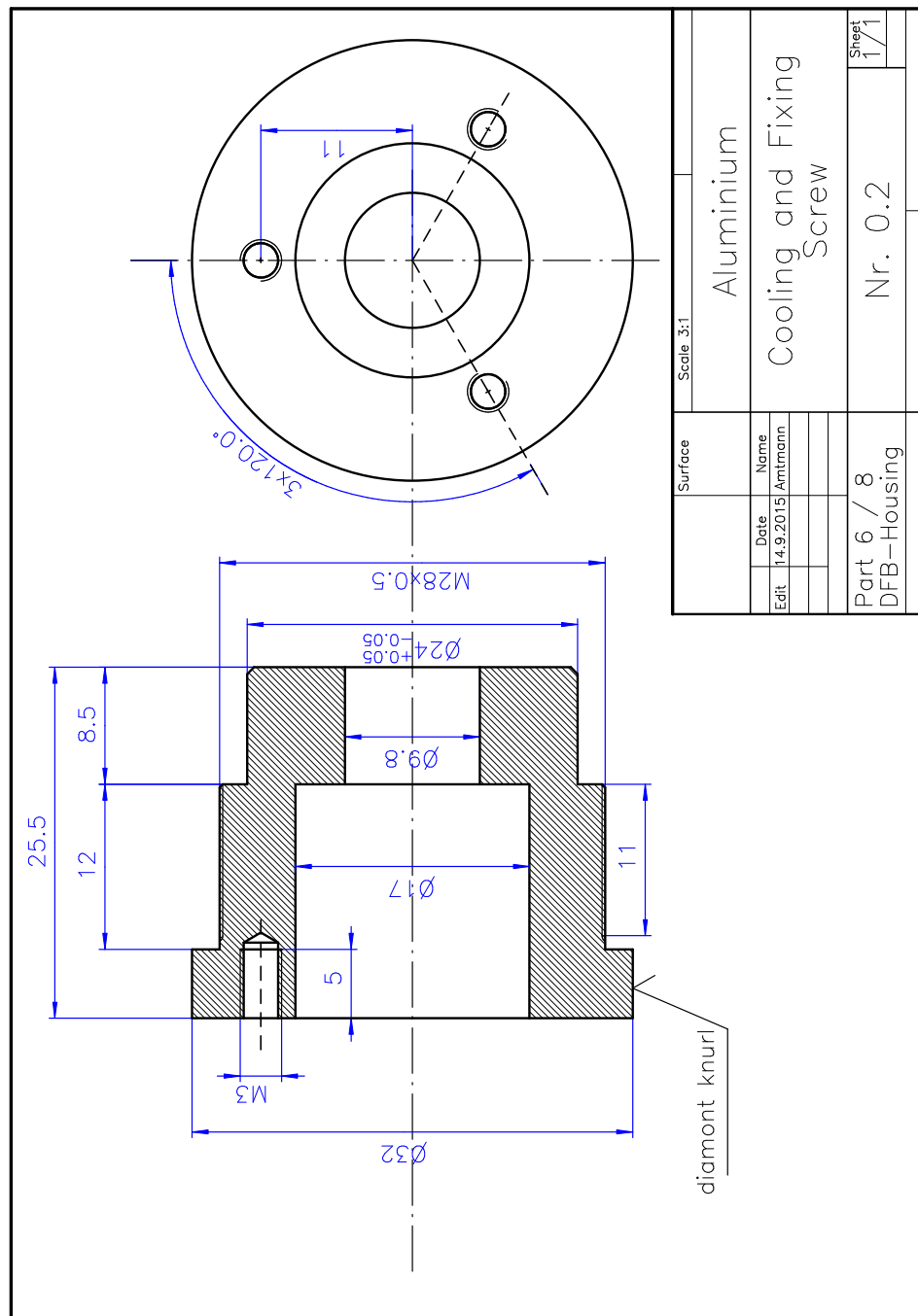
Figure A.7.: The cooling and fixing screw is part 6 of the DFB-laser housing.
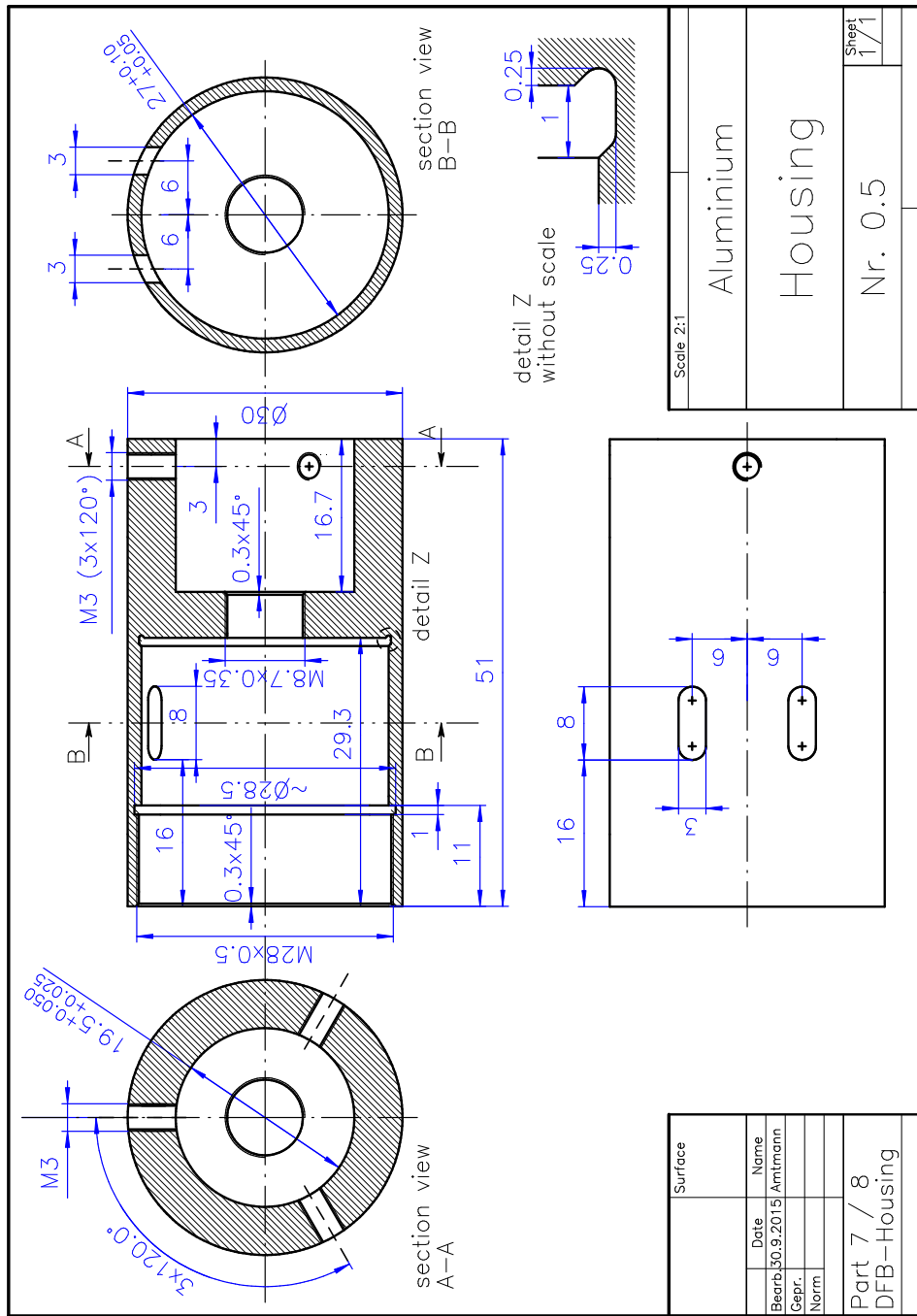
Figure A.8.: The housing for the single components is part 7 of the DFB-laser housing.

Figure A.9.: The supporting construction is part 8 of the DFB-laser housing.

A.2.2. Laser Collimation Control (LCC)

Figure A.10.: LCC Lens Mounting Part 1 and Part 2

A.3. List of Acronyms

CPT Coherent Population Trapping i

EIT electromagnetically induced transparency 8

VCSEL Vertical Cavity Surface Emitting Laser i

DFB Distributed Feedback i

TEC thermoelectric cooler 63

S+K Schäfter+Kirchhoff GmbH 32

LCC Laser Collimation Control i
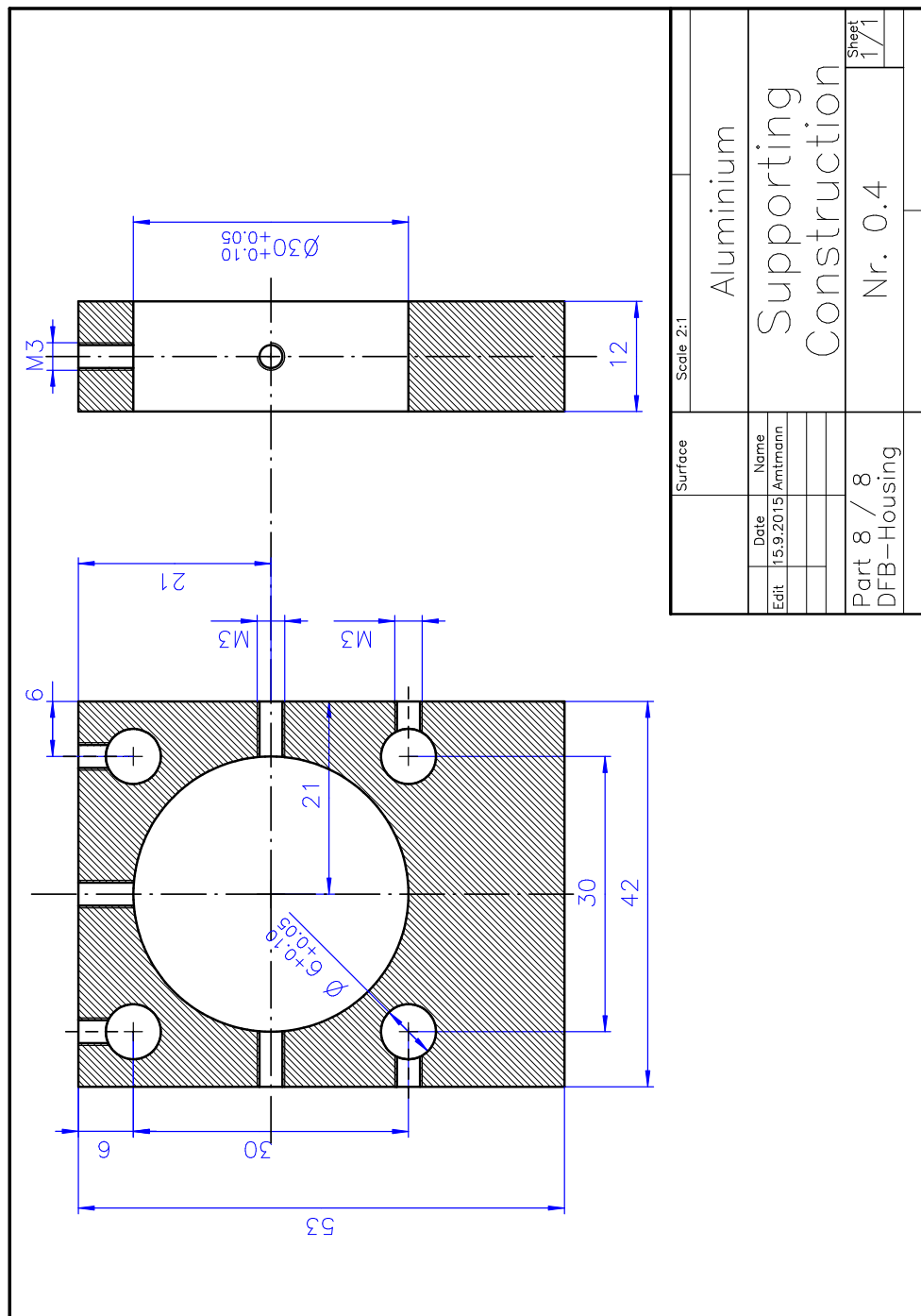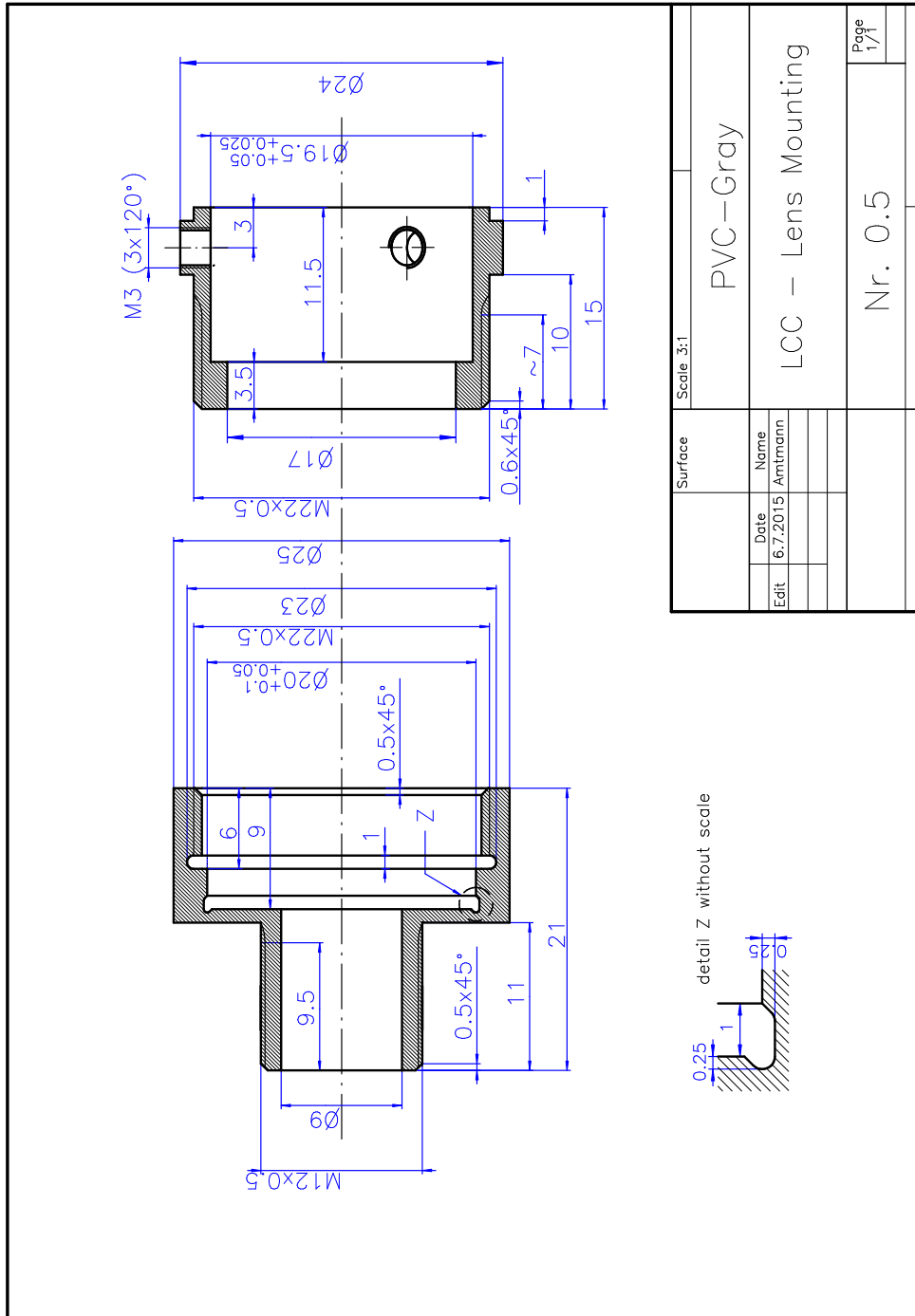
IR infra red 12

FM frequency modulation 15

AM amplitude modulation 22

PM phase modulation 34

ECDL external cavity laser diode 21

EM electromagnetic 3

TEM transverse electromagnetic mode 25

GUI graphical user interface 49

PSD phase sensitive detector 35

NA numerical aperture 28

MMF multi-mode fibre 29

SMF single-mode fibre 29

CDSM Coupled Dark State Magnetometer i

FWHM full width at half maximum 7

HF high frequency 33

NTC negative temperature coefficient 63

GPIB General Purpose Interface Bus 49

ESD electrostatic discharge 70

EOS electrical overstress 71

PLL Phase Lock Loop 61

Danksagung

Bibliography

[1] *795nm Single mode VCSEL in tilted cap TO46*. Oclaro, Inc. 2012. URL: www. oclaro.com.

[2] C. Affolderbach et al. "Nonlinear spectroscopy with vertical-cavity surface-emitting laser (VCSEL)". In: *Appl. Phys. B 70, 407-413* (2000).

[3] B. D. Agep'ev, M. B. Gornyi, and B. G. Matisov. "Coherent popuation trapping in quantum systems". In: *Physics - Uspekhi 36 (9)* (1993).

[4] E. Arimondo. "Coherent popuation trapping in laser spectroscopy". In: *Progress in Optics XXXV* (1996).

[5] E. Arimondo. "Relaxation processes in cohherent-population trapping". In: *Physical Review A* (1996).

[6] E. Arimondo and G. Orriols. "Nonabsorbing Atomic Coherences by Coherent Two-Photon Transitions in a Three-Level Optical Pumping". In: (1976).

[7] *Bernhard Halle Nachfl. Bestformlinsen*. Katalog S015: Standard-Programm. Bernhard Halle Nachfl. GmbH. Hubertusstraße 10 D-12163 Berlin, 2015.

[8] G.C. Bjorklund et al. "Frequency Modulation (FM) Spectroscopy". In: *Appl. Phys. B 32, 145-152* (1983).

[9] *CH-38-1.0-0.8 Thermoelectric Module (Peltier Module) Specifications*. TE Technology, Inc. 1590 Keane Drive, Traverse City, MI, 49696-8257 USA, 2010. URL: http://tetech.com/wp-content/uploads/2013/09/CH-38-1.0-0.8.pdf.

[10] *Coaxial Bias-Tee ZX85-12G+*. Mini-Circuits. P.O. Box 350166, Brooklyn, NY 11235-0003 USA.

[11] W. Demtröder. *Experimentalphysik 2*. Springer-Verlag Berlin Heidelberg, 2009.

[12] W. Demtröder. *Experimentalphysik 3*. Springer-Verlag Berlin Heidelberg, 2010.

[13] W. Demtröder. *Laserspektroskopie*. Springer-Verlag Berlin Heidelberg, 2007.

[14] *DEVICE SPECIFICATIONS GPIB-USB-HS+*.

[15] *DL 100 Diode Laser System Manual*. TOPTICA Photonics AG. Fraunhofgasse 14 82152 Martinsried/Germany, 2002.

[16] Jürgen Eichler and Hans Joachim Eichler. *Laser Bauformen, Strahlführung, Anwednungen*. 7. Springer-Verlag Berlin Heidelberg, 2010. URL: 10.1007/978-3-642-10462-6.

[17] M. Ellmeier. "Influence of Characteristic Parameters on the Performance of a Coupled Dark State Magnetometer". MA thesis. Karl-Franzens-Universität Graz.

[18] M. Erhard and H. Helm. "Buffer-gas effects on dark esonances: Theory and experiment". In: *Physical Review A* 63.043813 (2001), 63ff.

[19] M. Erhard, S. Nußmann, and H. Helm. "Power broadening and Doppler effects of the coherent dark resonances in Rb". In: *Physical Review A, Volume 62, 061802(R)* (2000).

[20] Zbigniew Ficek and Stuard Swain. *Quantum Interference and Coherence*. Springer Science+Business Media, Inc., 2005.

[21] *FS725 Rubidium Frequency Standard Operation and Service Manual*. Version 1.2 (3/2013). Stanford Research Systems. 1290-D Reamwood Avenue Sunnyvale, California 94089, 2002, 2013.

[22] Eugene Hecht. *Optik*. Oldenbourg Verlag München Wien, 2005.

[23] David Jiles. *Introduction to Magnetism and Magnetic Material*. Taylor and Francis Group, 1998.

[24] S. Kappe et al. "Simple parameterization of dark-resonance line shapes". In: *Appl. Phys. B 76, 57–63* (2003). DOI: 10.1007/s00340-002-1072-8.

[25] S. Kappe et al. "Temperature dependence of the coherent population trapping resonances". In: *Appl. Phys. B 74* (2002), pp. 217–222. DOI: 10.1007/s003400200800.

[26] S. Kraft et al. "Rubidium spectroscopy at 778-780 nm with a distributed feedback laser diode". In: *laser Phys. Lett. 1-6* (2004).

[27] Peter Lambropoulos and David Petrosyan. *Fundamentals of Quantum Optics and Quantum Information*. Springer-Verlag Berlin Heidelberg, 2007.

[28] Roland Lammegger. "Coherent Population Trapping - Ein Quanteninterferenzeffekt als Basis optischer Magnetometer". PhD thesis. Technischen Universität Graz, 2006.

[29] *LED800-series*. Roithner LaserTechnik GmbH. Wiedner Hauptstraße 76, 1040 Vienna, Austria, 2011. URL: http://www.roithner-laser.com/datasheets/led_div/infrared/led800-series.pdf.

[30] *Mikrowellen Signalgenerator: R&S SMR20*. Rohde&Schwarz.

[31] *Model SR830 DSP Lock-In Amplifier Stanford Research Systems*. 1993.

[32] *NTC thermistors for temperature measurement Glass-encapsulated sensors, standard type Series/Type: B57550G1*. 2014.

[33] G. Orriols. "Nonabsorbing Resonances by Nonlinear Coherent Effects in a Three-Level System". In: (1979).

[34] T. L. Paoli and J. E. Ripper. "Direct Modulation of Semiconductor Lasers". In: *IEEE, Vol. 58, No. 10* (1970).

[35] Dietmar Petrascheck and Franz Schwabl. *Elektrodynamik*. Springer-Verlag Berlin Heidelberg, 2015. DOI: 10.1007/978-3-662-43457-4.

[36] *Polarizing Beamsplitter Cubes*. Bernhard Halle, GmbH.

[37]   A. Pollinger et al. "Control Loops for a Coupled Dark State Magnetometer". In: *IEEE Sensors* (2010).

[38]   A. Pollinger et al. "Enable the inherent omni-directionality of an absolute coupled dark state magnetometer for e.g. scientific space applications". In: *IEEE* (2012). DOI: `978-1-4577-1772-7/12`.

[39]   Characterization of coherent population-trapping resonances as atomic frequency references. "S. Knappe and R. Wynands and J. Kitching and H. Robinson and L. Hollberg". In: *J. Opt. Soc. Am. B / Vol. 18, No. 11* (2001).

[40]   J. Ringot et al. "Generation of phase-coherent laser beams for Raman spectroscopy and cooling by direct current modulation of a diode laser". In: *Eur. Phys. J. D 7,285-288* (1999).

[41]   *Semiconductor Laser Diode Nr.LD-0795-0020-DFB-1*. TOPTICA Photonics AG. Lochhamer Schlag 19 - D-82166 Gräfelfing, 2009. URL: `www.toptica.com`.

[42]   J. Seufert et al. "DFB laser diode in the wavelength range from 760 nm to 2.5 μm". In: *Spectrochimica Acta Part A 60 3243.3247* (2004).

[43]   *Silicon PIN Photodiode BPX 61*. 1.1. OSRAM Opto Semiconductors GmbH. Leibnizstraße 4, D-93055 Regensburg, Jan. 2014.

[44]   Daniel A. Steck. "Rubidium 87 D Line Data". In: (2003). URL: `http://steck.us/alkalidata`.

[45]   Ulrich Tietze and Christoph Schenk. *Halbleiter-Schaltungstechnik*. 13th. Springer-Verlag Berlin Heidelberg, 2010.

[46]   *Type: EZ 141-AL-TP/M17 SEMI RIGID, the form stable microwave cable*. 2002.

[47]   Osamu Ueda and Stephen J. Pearton, eds. *Materials and Reliability Handbook for Semiconductor Optical and Electron Devices*. Springer Science+Business Media, Inc., 2013.

[48]   Jacques Vanier and Claude Audoin. *The Quantum Physics of Atomic Frequency Standards*. Adam Hilger, Bristol and Philadelphia, 1989.

[49]   R. Wynands and A. Nagel. "Precision spectroscopy with coherent dark states". In: *Appl. Phys. B 68, 1-25* (1999).

[50]   R. Wynands et al. "Selection rules and line strengths of Zeeman-split dark resonances". In: *Physical Review A 58, 196* (1998).

[51]   Matt Young. *Optik, Laser, Wellenleiter*. Springer-Verlag Berlin Heidelberg, 1997.